Lehrstuhl für Solartechnik

RWTH AACHEN UNIVERSITY

The present work was submitted to the Institute of Solar Research,
German Aerospace Center (DLR)

Force Analysis on Flexible Pipe Connectors of Parabolic Trough Solar Collectors

Kraftanalyse an flexiblen Rohrverbindungen von Parabolrinnen-Solarkollektoren

Master-Thesis

presented by
Joan Henri Weiß
380057

1^{st} Examiner: Univ.-Prof. Dr.-Ing. Robert Pitz-Paal
2^{nd} Examiner: Dr.-Ing. Eckhard Lüpfert

Tutor: Dr.-Ing. Sonja Kallio

Almería, May 30, 2025

Abstract

Concentrating Solar Power (CSP) enables renewable energy with thermal storage and high grid stability. Parabolic Trough Collectors (PTCs) are an established technology in commercial solar power plants. A critical component of these systems are the flexible pipe connectors, which connect the solar field with the absorber tubes of the collectors and are exposed to high mechanical loads due to daily tracking movements and thermal expansion. Due to their function, these components are referred to as Rotation and Expansion Performing Assemblies (REPAs). REPAs are dynamic seal systems subject to wear, making their long-term durability a key reliability concern. A failure of these components can lead to leaks, potentially causing fires and unplanned power plant shutdowns.

This study investigates the long-term behavior of REPAs through accelerated lifespan testing and force analyses to understand how stresses evolve and enable predictive maintenance. The two main types of REPAs, Rotary Flex Hose Assemblies (RFHA) and Ball Joint Assemblies (BJA), are tested on a specially developed test rig. A full daily tracking cycle is simulated in 2.5 minutes, resulting in 10,000 cycles over one month, equivalent to a 30-year operational lifetime. The tests are conducted under realistic conditions, with a heat transfer fluid (HTF) at 393 °C and 34 bar pressure.

In the RFHA test campaign, 24,240 cycles were carried out until the test was terminated due to a leak. The analysis reveals that the forces on RFHAs remain stable throughout the lifecycle, but 1,000 cycles before a critical leak show early increases in forces and torques, with 150 cycles before the failure, significant force spikes can be observed. These findings enable the development of a condition monitoring system where force measurements and vibration analyses for both REPA types and optical angle monitoring, especially for BJAs, could serve as cost-effective monitoring methods. Only the first test series has been completed in the BJA test campaign, with 2,700 cycles performed. As no leaks or failures have occurred, no definitive conclusions regarding predictive maintenance can be drawn; however, load behavior similarities suggest that early failure indicators may emerge. In ongoing testing, these sensor approaches will be further investigated to develop a reliable and practical early fault detection strategy.

Kurzdarstellung

Konzentrierende Solarenergie ermöglicht die Nutzung erneuerbarer Energie mit thermischer Speicherung und hoher Netzstabilität. Besonders Parabolrinnen Kollektoren sind eine etablierte Technologie, die in kommerziellen Solarkraftwerken eingesetzt wird. Ein kritisches Bauteil dieser Anlagen sind flexible Rohrverbindungen, die das Verbindungsstück zwischen Solarfeld und den Absorberrohren darstellen und aufgrund der täglichen Nachführbewegungen sowie thermischer Ausdehnung hohen mech-

anischen Belastungen ausgesetzt sind. Aufgrund ihrer Funktion werden diese Komponenten als Rotation and Expansion Performing Assemblies (REPAs) bezeichnet. REPAs sind Gleitdichtungssysteme, die einem Verschleiß unterliegen, wodurch ihre langfristige Haltbarkeit von großer Bedeutung ist. Ein Versagen dieser Komponenten kann zu Leckagen führen, die Brände verursachen und ungeplante Kraftwerksstillstände zur Folge haben können.

Diese Arbeit untersucht das Langzeitverhalten von REPAs durch beschleunigte Lebensdauertests und Kraftanalysen, um Belastungsveränderungen zu erfassen und eine Predictive Maintenance zu ermöglichen. Auf einem eigens entwickelten Teststand werden die beiden Hauptbauarten der REPAs, Rotary Flex Hose Assemblies (RFHA) und Ball Joint Assemblies (BJA) untersucht. Ein vollständiger Tageszyklus der Nachführung wird in 2,5 Minuten simuliert, sodass innerhalb eines Monats 10.000 Zyklen, entsprechend einer Betriebsdauer von 30 Jahren, durchgeführt werden. Die Tests erfolgen unter realistischen Bedingungen mit einem Wärmeträgerfluid bei 393 °C und 34 bar.

In der RFHA-Testkampagne wurden 24.240 Zyklen durchgeführt, bis der Test aufgrund einer Leckage abgebrochen wurde. Die Analyse zeigt, dass die Kräfte auf die RFHAs über den Lebenszyklus hinweg stabil bleiben. Bereits 1.000 Zyklen vor einer kritischen Leckage steigen Kräfte und Momente leicht an. In den letzten 150 Zyklen vor dem Versagen treten deutliche Kraftspitzen auf. Diese Erkenntnisse ermöglichen die Entwicklung eines Condition-Monitoring-Systems, bei dem Kraftmessungen und Schwingungsanalysen für beide REPA-Typen sowie eine optische Winkelüberwachung, insbesondere bei BJAs, als kostengünstige Überwachungsmethoden dienen könnten. In der BJA-Testkampagne wurde bisher nur die erste Testreihe mit 2.700 Zyklen abgeschlossen. Es sind noch keine Leckagen oder Ausfälle aufgetreten. Daher sind derzeit keine klaren Aussagen zum Predictive Maintenance möglich. Ähnliche Muster im Lastverhalten deuten darauf hin, dass frühe Ausfallindikatoren erkannt werden könnten. In laufenden Tests werden diese Sensoransätze weiter untersucht, um eine zuverlässige und praxisnahe Strategie zur frühzeitigen Fehlererkennung zu entwickeln.

Nomenclature

Acronyms and Abbreviations

BJA	Ball Joint Assembly	Flexible pipe connection allowing rotation and thermal expansion
CIEMAT	Centro de Investigaciones Energéticas, Medioambientales y Tecnológicas	Spanish research institution for energy and environment
CSP	Concentrating Solar Power	Technology using mirrors or lenses to concentrate solar energy for thermal power generation
DLR	Deutsches Zentrum für Luft- und Raumfahrt e. V.	German Aerospace Center
DNI	Direct Normal Irradiation	Solar radiation received per unit area by a surface perpendicular to the sun's rays
DP-DPO	Diphenyl-Diphenyl Oxides	Heat transfer fluid used in CSP plants
GUI	Graphical User Interface	
HCE	Heat Collecting Element	Absorber tube in the focal line of a parabolic trough
HTF	Heat Transfer Fluid	Fluid used to transport thermal energy within a solar thermal system
LCOE	Levelized Cost of Energy	Average total cost of building and operating a power plant per unit of electricity generated
LEF	Lower East Force	Force measured at the east side lower support
LEM	Lower East Torque	Torque measured at the east side lower support

LR	Linear Regression	
LWF	Lower West Force	Force measured at the west side lower support
LWM	Lower West Torque	Torque measured at the west side lower support
OPC	Open Platform Communications	
PLC	Programmable Logic Controller	
PSA	Plataforma Solar de Almería	Solar research center in southern Spain
PTC	Parabolic Trough Collector	Solar concentrator using parabolic mirrors
REPA	Rotation and Expansion Performing Assembly	Flexible connection between absorber tube and solar field piping
RFHA	Rotary Flex Hose Assembly	Flexible pipe connection allowing rotation and thermal expansion
SCA	Solar Collector Assembly	Trough collector of typically 150 m length
SCADA	Supervisory Control and Data Acquisition	
SCE	Solar Collector Element	Collector module, smallest repeating unit of a parabolic trough collector

Greek Symbols

α_r	Sunrise angle rotational position	°
α_s	Sunset angle rotational position	°
α_{cold}	Cold angle translational position	°
α_{end}	End angle rotational position	°
α_{hot}	Hot angle translational position	°
α_{stow}	Stow angle rotational position	°
η	Viscosity	mPa · s

μ	Hysteresis	
ρ	Density	$^{\mathrm{kg}}/_{m^3}$
σ	Stefan–Boltzmann constant	$5.67 \cdot 10^{-8}\,^{\mathrm{W}}/_{m^2K^4}$

Roman Symbols

$\dot{q}''_S$	Radiated power per area	$^{\mathrm{W}}/_{m^2}$
A_C	Collector area	m^2
A_R	Receiver area	m^2
b_{rg}	Relative repeatability error	% FS
c_p	Specific heat capacity	$^{\mathrm{J}}/_{kg \cdot K}$
d_{cr}	Relative creep	% FS
d_{lin}	Relative linearity error	% FS
F	Force	N
F_{dyn}	Dynamometer/load cell force	N
F_{Nom}	Nominal laod cell force	N
I_0	Solar constant	$1361\,^{\mathrm{W}}/_{\mathrm{m}^2}$
S	Characteristic load cell value	$^{\mathrm{mV}}/_{\mathrm{V}}$
S_N	Characteristic nominal load cell value	$^{\mathrm{mV}}/_{\mathrm{V}}$
S_0	Zero signal (unmounted)	$^{\mathrm{mV}}/_{\mathrm{V}}$
S_{F0}	Zero signal when mounted	$^{\mathrm{mV}}/_{\mathrm{V}}$
TK_0	Temperature effect on zero signal	$^{\%\ \mathrm{FS}}/_{\mathrm{K}}$
TK_C	Temperature effect on calibration constant	$^{\%\ \mathrm{RD}}/_{\mathrm{K}}$
U	Voltage	V
U_A	Measuring range end value	V
U_D	Wheaton bridge voltage	V
u_e	Load cell input sensitivity	$^{\mathrm{mV}}/_{\mathrm{V}}$
U_S	Load cell amplifier supply voltage	V

u_s	Load cell output signal	$^{mV}/_{V}$
C	Concentration factor	
g	Local acceleration of free fall	$9.81\,^{m}/_{s^2}$
K	Decoupling matrix	
k	Load cell scaling factor	$^{V}/_{N}$
LCOE	Levelized Cost of Energy	$^{\$}/_{kWh}$
M	Torque	Nm
m	Mass	kg
T	Temperature	°C or K

Contents

List of Figures

List of Tables

1. Introduction

Climate change is one of the greatest challenges of our time. A key approach to limiting the rise in global temperatures is to switch to renewable energies. The Paris Agreement of the COP21 climate conference sets the goal of significantly reducing global greenhouse gas emissions to keep global warming below 2 °C above pre-industrial levels and, if possible, to limit it to 1.5 °C [1]. Concentrated solar power (CSP) is a promising technology in this area. CSP power plants use concentrated solar radiation to generate heat, which can be stored in thermal storage facilities and used to generate electricity when required. Parabolic trough collectors (PTCs), in particular, are widely used, as they are a proven technology and offer dispatchability through thermal storage and, thus, high grid stability. [2]

The German Aerospace Center (DLR) is conducting research in various aspects of CSP technology in collaboration with the Spanish research center Centro de Investigaciones Energéticas, Medioambientales y Tecnológicas (CIEMAT) at the Plataforma Solar de Almería (PSA) in Spain. The PSA is one of the world's leading research facilities for concentrated solar power and offers extensive testing facilities for components and systems in the field of solar thermal energy. Key research areas at the PSA include optimizing heat storage systems, developing new collector technologies, and investigating material resistance under extreme operating conditions. [3]

This thesis investigates the durability and failure mechanisms of flexible pipe connections in parabolic trough power plants. These components, known as Rotation and Expansion Performing Assemblies (REPAs), connect the fixed piping system of the solar field with the absorber tubes of the parabolic trough collectors. REPAs are exposed to high temperatures, high pressures, repeated movements, mechanical loads, and concentrated solar radiation. Failures and ruptures in these flexible pipe connectors can have severe consequences, such as leakage and fire of hot heat transfer fluid, making their reliability a critical factor in CSP power plant operation. To address these challenges, continuous condition monitoring of REPAs is essential for transi-

tioning from reactive maintenance strategies to predictive maintenance approaches, which can significantly reduce operation and maintenance costs.

To study the loads and long-term behavior of the REPAs, accelerated lifespan tests are conducted using the REPA test rig at the PSA. These tests simulate real operating conditions, including nominal field parameters of 393 °C, 34 bar, thermal oil flow, thermal expansion, and tracking movements, to evaluate the durability and performance of the components over time. Load cells are installed under the REPAs to measure forces and torques in three directions during normal operation and failure events. As part of this work, different types of REPA are examined by carrying out a detailed force analysis of the tests performed. The knowledge gained can serve as a basis for future condition monitoring systems and support the development of predictive maintenance strategies. This would extend the service life of REPAs, increase their reliability, and reduce the operating costs of CSP power plants.

This work is part of the REPA project, co-funded by the German Federal Ministry for Economic Affairs and Energy (funding reference 03EE5141A). The author gratefully acknowledges this support. Additional support was provided through an Erasmus+ scholarship, which enabled international collaboration during the project.

The work is structured as follows: First, an overview of the basics of CSP technology and the current state of the art regarding REPAs is given. The experimental setup, including the sensors used, is then described in detail. The methodology of the force analysis, the test results, and their evaluation are then presented. Finally, the most important results are summarized, and an outlook on possible future research work is given.

2. Fundamentals and State of the Art

This chapter elucidates the fundamental principles and state of the art in concentrating solar power (CSP), a technology that uses sun energy to generate heat or electricity. It provides a comprehensive overview of the various CSP technologies, with a particular focus on parabolic trough collectors (PTCs). Additionally, it delves into the intricate functioning of the Rotation and Expansion Performing Assemblies (REPAs), which are integral components of PTCs. Furthermore, the chapter outlines the essentials of force measurement with load cells, a crucial aspect of the instrumentation utilized in this study.

2.1. Fundamentals of Concentrating Solar Power

The following subchapter presents an overview of the fundamental properties of solar radiation and the underlying physical principles. A central focus is on how solar radiation can be converted into usable forms of energy to support a sustainable energy supply. The subchapter gives an overview of the most important concepts of concentrating solar radiation and the various technologies for generating energy. Parabolic trough power plants, one of the most established technologies in CSP, are particularly examined.

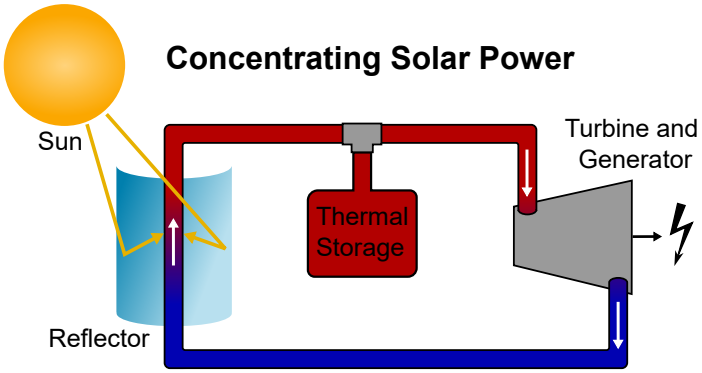

Figure 2.1.: Conventional concentrating solar power plants

As a primary energy source, the sun provides the basis for the utilization of solar energy in CSP power plants. These plants collect and concentrate the incident solar radiation in order to facilitate the effective conversion of solar energy into heat. Figure 2.1 shows the basic principle of a CSP Power Plant. The thermal energy generated by concentrated solar radiation can be stored in thermal storage units for later use or used immediately to generate electricity. The latter is achieved by converting heat into mechanical and electrical energy using turbines. In order to achieve elevated temperatures, the solar radiation is concentrated in a targeted manner. This is achieved using mirrors or lenses that focus the sunlight on a smaller area. [4]

$$C = \frac{A_C}{A_R} \tag{2.1}$$

The concentration factor shown in equation 2.1 describes the ratio between the collection area A_C and the irradiated target surface A_R. Higher concentration factors enable higher temperatures required for efficient electricity generation in thermal power plants. [5]

2.1.1. Solar Radiation

The Stefan Boltzmann law regards the sun as a black body that radiates energy. Equation 2.2 describes the radiated power of such a body. In this context, $\dot{q}''_S$ is the radiated power per area, which is calculated from the Stefan Boltzmann constant σ and the temperature of the body under consideration T in K. [6]

$$\dot{q}''_S = \sigma \cdot T^4 \tag{2.2}$$

With the solar surface temperature of $5777\,\mathrm{K}$, the solar constant I_0 shown in the equation 2.3 follows. The solar constant describes the energy emitted by the sun that reaches the Earth as solar radiation. [7]

$$I_0 \approx 1361\,\mathrm{W/m^2} \approx 12\,\mathrm{MWh/m^2a} \tag{2.3}$$

When solar radiation enters the Earth's atmosphere, some of this radiation is reduced by reflection, absorption, and scattering. In particular, Rayleigh and Mie scattering on microparticles contribute to this attenuation. These effects result in less radiation reaching the Earth's surface than the solar constant. [8]

For CSP, not the total global radiation is relevant, but only the direct normal irradiance (DNI). The DNI is the proportion of solar radiation that reaches a surface perpendicular to the sun's direction without being scattered. Figure 2.2 shows the average worldwide DNI. CSP systems can only work efficiently if the DNI is sufficiently high. An annual DNI value from 1900 $^{\mathrm{kWh}}/_{m^2}$ to 2100 $^{\mathrm{kWh}}/_{m^2}$ is necessary to make the operation of such systems economically viable.[4]

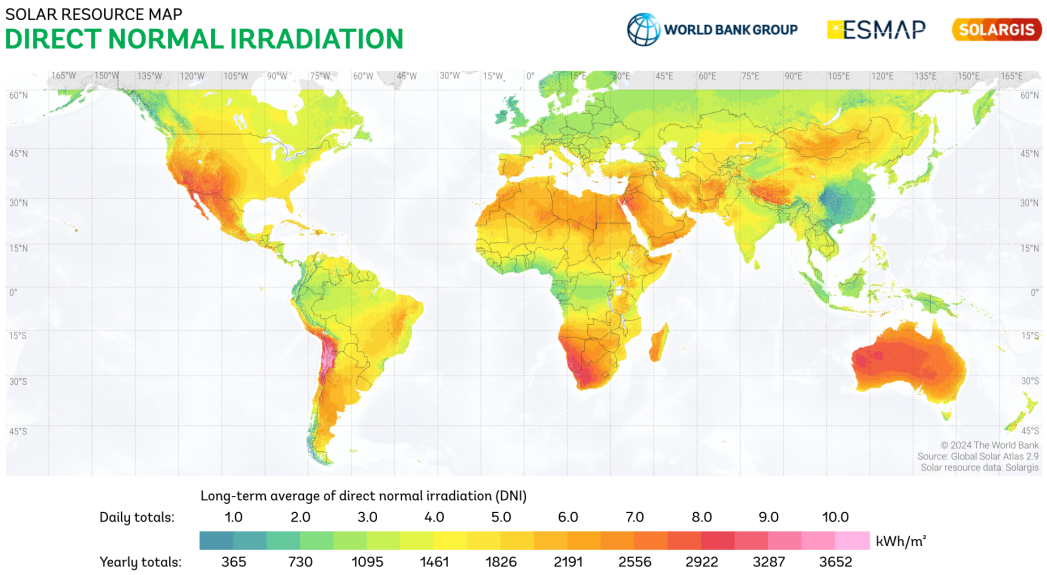

Figure 2.2.: Average worldwide annual and daily direct normal irradiation [9]

2.1.2. CSP Technologies

To get an overview of the most common CSP technologies, it is important to distinguish between point-focusing and line-focusing systems. The light is concentrated on a single point in point-focusing systems, such as solar towers or parabolic dishes. The light is concentrated along a line in line-focusing systems, such as parabolic troughs or linear Fresnel collectors. [4]

Figure 2.3 shows the two common point-focusing technologies. The left-hand side shows the schematic structure of a solar tower power plant. The most important components of a solar tower power plant are the heliostats, the tower, and the receiver integrated into the tower. The incident sunlight is reflected by the heliostats, large, slightly curved mirrors, and concentrated on the receiver. Due to the high

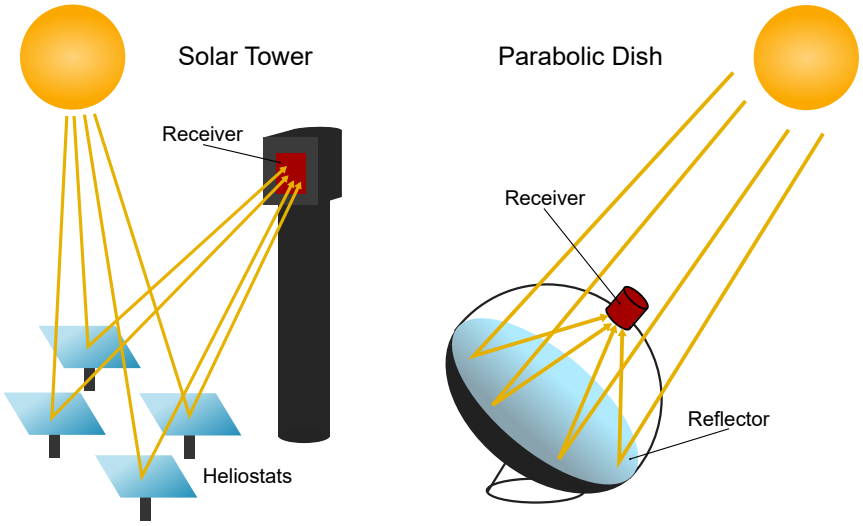

Figure 2.3.: Point-focussing CSP technologies

concentration factor, temperatures of up to 1200 °C are reached. The connected conventional power plant process can achieve high efficiencies with this high temperature. Depending on the latitude at which the power plant is built, a north or a surrounding field is selected. In a north field configuration, heliostats are arranged on only one side of the tower to reduce shading and reflections. They are placed around the tower in a surrounding field to enable more uniform solar energy collection throughout the day. [5]

Figure 2.4 shows the north field of the CESA-1 Solar Tower owned by CIEMAT at the PSA in Spain. The maximum field size of a heliostat field is limited due to various loss mechanisms that increase with the distance of the heliostats to the tower and receiver. For this reason, multi-tower arrays are also conceivable, that use several small towers with receivers. [5]

In addition to the solar tower, parabolic dishes are the second common CSP point-focusing technology. Figure 2.3 shows the general structure of a parabolic dish on the right-hand side. Parabolic point-focus concentrators are a type of CSP technology that utilizes a rotationally symmetric shape to harness solar energy. These dishes are designed to reflect incoming sunlight onto a receiver at the focal point [11]. The typical diameter of a solar dish ranges from 5 to 10 m, covering an area between 40 and 120 m^2. A Stirling or Brayton engine coupled with an electric generator is po-

Figure 2.4.: Solar tower CESA-1 at the PSA owned by CIEMAT [10]

sitioned at the focal point to convert the concentrated solar energy into electricity. Parabolic dishes have concentration ratios of up to 2000. As a result, temperatures around 750 °C and pressures of up to 200 bar are achieved during operation [11]. Each dish can produce between 5 and 50 kW of electricity. This scalability makes parabolic dishes versatile for various energy needs and particularly suitable for small, stand-alone power-generating applications.[12]

Point-focusing systems, such as solar towers and parabolic dishes, require two-axis tracking to focus direct solar radiation effectively. This precise tracking ensures that the concentrated sunlight remains focused on the receiver throughout the day as the sun moves across the sky. [11]

Figure 2.5 shows the line-focusing technologies. The left-hand side shows the schematic structure of a linear Fresnel system. The name of this type of system is derived from the Fresnel lens. An array of long linear mirrors is employed in a linear Fresnel reflector, representing a continuous curve analogous to the Fresnel lens. Mirrors of a near-flat, slightly curved configuration are employed. The mirrors are mounted on a tracking system that enables them to follow the sun from east to west. The sunlight is reflected onto a fixed receiver in the center above the mirrors. [13]

Figure 2.6 shows the configuration of the receiver. The absorber tube is located at the center of the receiver. Most commercial applications use water as the heat transfer fluid (HTF). The water passes through the absorber tube, undergoes vaporization and

superheating, and can finally be utilized to generate energy in a turbine coupled with a generator [11]. A secondary concentrator is installed in the receiver to concentrate the reflected sunlight further. The insulation attached to it reduces the heat loss of the receiver. [14]

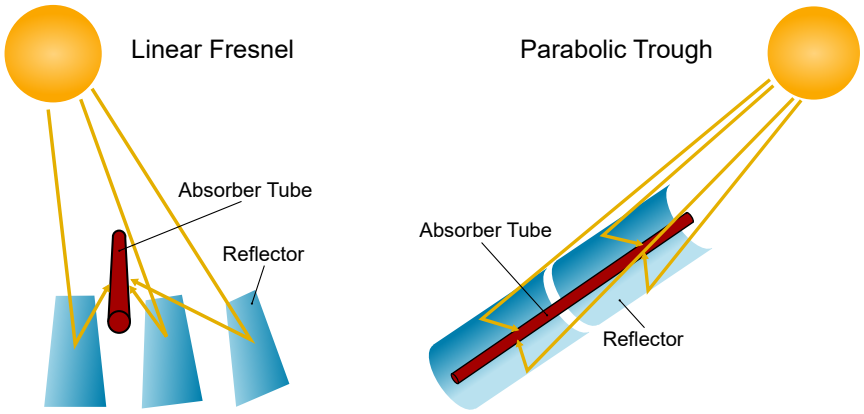

Figure 2.5.: Line-focussing CSP technologies

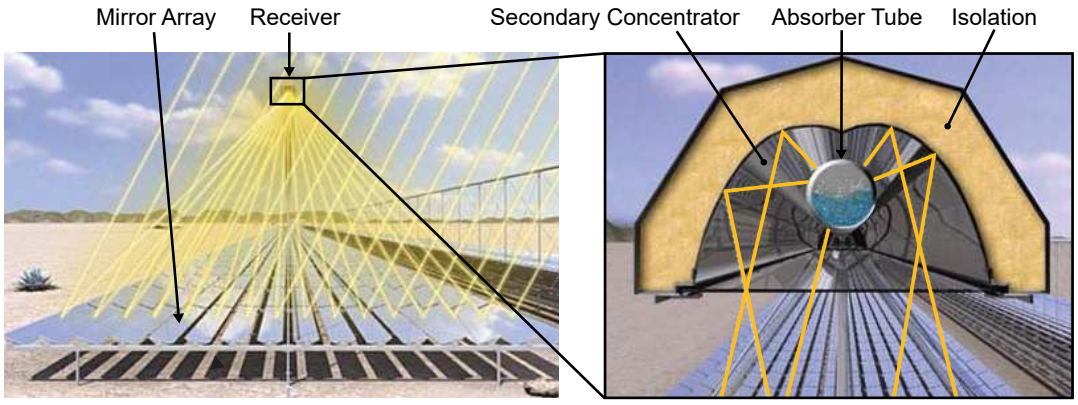

Figure 2.6.: Linear fresnel system and receiver with secondary concentrator [14]

On the right-hand side, figure 2.5 shows the schematic structure of a PTC. In solar PTCs, parabolic-shaped mirrors reflect and focus the sunlight onto an absorber tube [15]. The trough is designed so that the sun rays enter parallel to the axis of symmetry and are thus concentrated on a focal line. In this focal line, the absorber tube gets mounted. The supporting structure connects the parabolic trough and the absorber tube and follows the sun throughout the day using the tracking device [2]. In general, line-focusing systems, such as parabolic troughs and linear Fresnel collectors, only require single-axis tracking. [11]

As this work mainly deals with PTC power plants and the critical structural components, this type of CSP technology is explained in more detail in subsection 2.1.3

2.1.3. Parabolic Trough Collector in Detail

As described in subsection 2.1.2 on the basics of the CSP, a PTC consists of 4 main components, which this subsection describes in more detail. This includes the supporting structure, the mirrors, the absorber tube with an HTF, and the tracking system. First, the general structure of a PTC power plant is explained, and then the individual main components of the PTC are described.

Figure 2.7 shows the schematic structure of a typical PTC power plant, in this case, the Andasol I power plant. This power plant near Granada, Spain, was constructed in 2009 as Europe's first PTC power plant. Today, there are three units at this site (Andasol I-III), each with an installed capacity of 50 MW [16]. The PTC is the most advanced and widely adopted technology for large-scale CSP generation. [4]

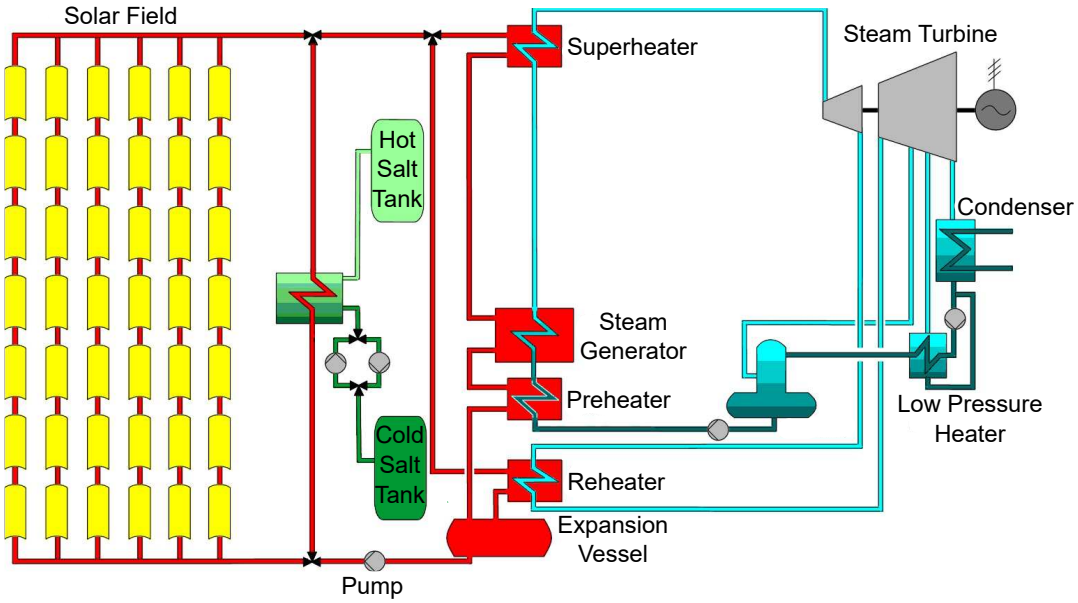

Figure 2.7.: Circuit diagram of a PTC power plant - Example based on Andasol I [5]

The operational concept of a PTC power plant closely resembles that of traditional power plants using steam in a Rankine cycle, even though it relies on solar energy as the heat source. A network of PTCs in the solar field absorbs sunlight, which is

then used to heat the HTF. This energy stored in the HTF powers the Rankine cycle to generate electricity. To achieve maximum efficiency, the system incorporates four stages of heat exchange. Water is preheated in a solar heat exchanger and converted into steam in a vaporizer. The steam is superheated before entering the high-pressure turbine. After this stage, the steam is reheated and directed through a low-pressure turbine. Both turbines are connected to a generator via an axle, which drives the generator. In addition to its ability to harness solar energy, the power plant is equipped with a thermal storage system that enables continuous electricity production, even when sunlight is unavailable. This system uses molten salt stored in two separate tanks to manage excess heat. During periods of strong solar radiation, surplus energy is stored, which can be utilized later when solar input decreases, such as at night. This ensures a consistent energy supply and makes the plant highly flexible in meeting fluctuations in grid demand. [5] This flexibility, referred to as dispatchability, is a significant advantage of PTC power plants with integrated storage, enhancing their competitiveness in the energy market. [17]

The solar field in commercial PTC power plants is constructed according to the principle shown in Figure 2.8. Several solar collector elements (SCEs) are assembled to form a solar collector assembly (SCA). Then, several SCAs are connected in series to form a collector loop. A cold header pipe extends from the power block, transporting the cold HTF to the individual collector loops. After passing through the loop, the heated HTF flows into the hot header pipe and back to the power block, where the thermal energy is used. [17]

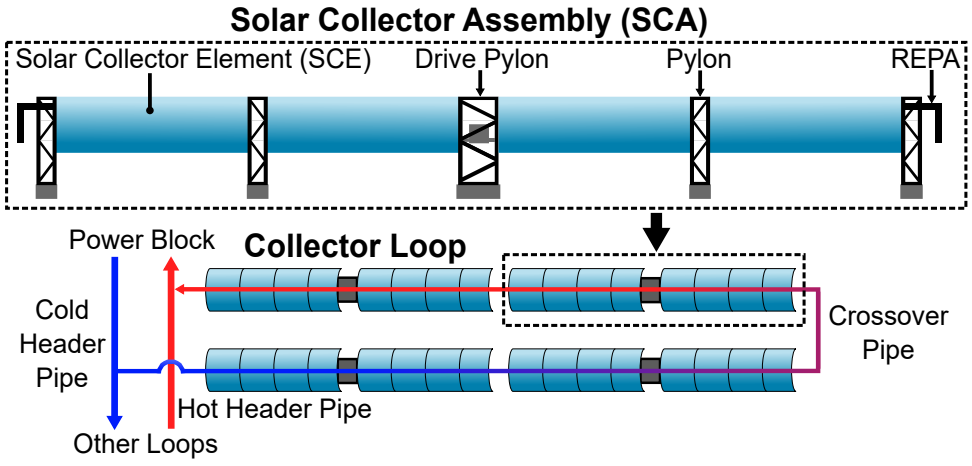

Figure 2.8.: Parabolic trough solar collector assembly and collector loop

The individual SCEs and SCAs are assembled on-site during the power plant construction. Each SCA consists of a drive pylon for sun tracking, several normal pylons, the SCEs, and two REPAs connecting the heat collecting elements (HCEs) to the next SCA or the header pipes. For an SCE, several mirrors are mounted on a support structure with a jig. This jig ensures the alignment between the mirrors and the frame of the support structure. The pylons and the support structure are usually made of steel or aluminum, whereby aluminum has the advantage of lower weight with good mechanical properties [2]. Figure 2.9 shows multiple SCEs in an SCA. Depending on the manufacturer, SCEs have a length of 8 to 25 m. As between 6 and 12, SCEs are combined to form an SCA, the total length of an SCA is between 50 and 250 m. [18, 19, 20]

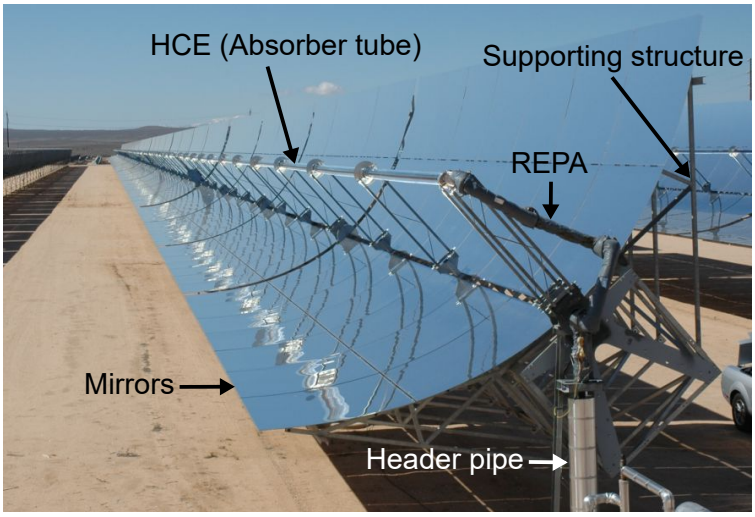

Figure 2.9.: *Heliotrough* Skal-ET collector elements in an SCA [21]

The mirrors are attached to the support structure. The production of the mirrors is a complex multi-step process. First, green glass is converted into solar glass, which reduces the absorption coefficient of the glass. The glass is then bent into the required parabolic shape and tempered. The most common bending processes are quench bending and sag bending. The glass treated this way is then coated in a final step to create a reflective layer. The state-of-the-art combines a sprayed-on silver layer, a copper layer, and lacquer. The silver layer ensures high reflectivity, and the copper and lacquer layers are applied as protective layers. Other possible materials for the mirrors or reflectors are aluminum, which achieves a reflectivity of up to 88 %, and polymers. However, the use of polymers is not yet economically viable. [2]

The mirrors reflect and concentrate the sunlight onto the HCE. The HCE, shown in Figure 2.10, consists of a metal absorber tube enclosed in a vacuum-sealed cover glass. This minimizes heat loss through convection and reduces the degradation of the metal absorber [2]. The absorber tube has a selective surface usually made of Ni-NiO, which achieves an absorption coefficient of 0.96 [22]. A high absorption coefficient combined with a low emission coefficient is a prerequisite for a high energy yield. This means that as much solar radiation as possible can be absorbed, and the energy can be transferred to the HTF. The bellows allow different expansions between the cover glass and the absorber tube while the seals maintain the vacuum. To protect the bellows and seals from solar radiation, the glass-to-metal areas are surrounded by radiation shields. As hydrogen accumulates in the vacuum due to thermal degradation of the HTF, hydrogen getters are installed in the tube. These absorb residual hydrogen and maintain the vacuum. [23]

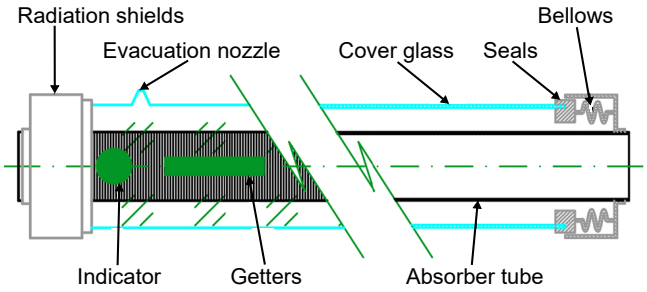

Figure 2.10.: Heat collecting element of a PTC [23]

The absorber tubes are filled with an HTF to ensure efficient operation of the PTC power plant. The selection of a suitable HTF influences the efficiency and profitability of the power plant. The required thermophysical properties of such an HTF are stability at temperatures above 400 °C, a low melting point, high thermal conductivity and high specific heat capacity for efficient heat storage, low corrosion rate, and low dynamic viscosity. As leaks and accidents can occur during operation, low flammability, low explosivity, and low toxicity are advantageous to protect the environment. Low costs and industrial availability also play a role. [24]

Table 2.1 shows common HTFs and their properties. A distinction can be made between 4 different types of HTFs. Diphenyl-diphenyl oxides (DP-DPO), silicone oils, molten salts, and water or steam are used in PTCs. The most widely used

are DP-DPOs such as *Therminol® VP-1*, an organic eutectic mixture consisting of 73.5 % diphenyl oxide ($C_{12}H_{10}O$) and 26.5 % diphenyl ($C_{12}H_{10}$). DP-DPOs have a maximum operating temperature of 400 °C and a melting point of 12 °C, requiring a freeze protection system. In contrast, silicone oils such as *Syltherm® 800* have a melting point below 0 °C, eliminating the need for a freeze protection system. These silicone oils are not organic like DP-DPO but contain siloxane-based chain molecules. [25]

Table 2.1.: Characteristics of HTFs in PTC applications [17]

Property	Unit	*Therminol® VP-1*	*Syltherm® 800*	*HELISOL® 5A*	*Solar Salt*	*HITEC®*	*HITEC® XL*
Freezing Point	[°C]	12	-40	-65	220	142	120
Max. Temp.	[°C]	400	400	430	600	535	500
ρ (300 °C)	[kg/m^3]	815	671	656	1899	1640	1992
η (300 °C)	[$mPa \cdot s$]	0,2	0,47	0,2	3,26	3,16	6,37
c_p (300 °C)	[J/kg K]	2319	2086	2235	1495	1560	1447
Costs	[-]	high	very high	high	low	medium	medium

Molten salts such as the HITEC are an interesting alternative to other HTFs, primarily due to their high-temperature stability and possible use in heat storage. The high possible temperatures increase the efficiency of the Rankine Cycle. In addition, molten salts serve as heat transfer and storage medium, meaning no heat exchangers are required for heat storage. The major disadvantages are the high corrosiveness and the high melting point of over 200 °C, which makes trace heating necessary. This is why molten salts are not yet widely used commercially [26]. As with molten salts, high temperatures of over 400 °C can also be achieved with water as the HTF. The primary advantages of the so-called direct steam generation are high efficiency due to the high temperatures and the fact that no heat exchanger is required. Both the water and maintenance costs are lower than those of a synthetic oil-based CSP power plant. The biggest challenge for direct steam generation is the control of the plant, which is more complex due to the layered two-phase flow inside the absorber tubes and the different flow patterns. [27]

According to the current state of research, supercritical carbon dioxide could also replace conventional HTFs. Solar-to-electric efficiency can be increased due to higher process temperatures and supercritical cycles. [28]

A tracking system is necessary as the sun's position changes throughout the day. Figure 2.11 shows the two standard tracking methods for PTCs. A distinction is made

between north-south and east-west tracking. The names of the methods are based on the direction in which the aperture surface of the PTC is rotated. In north-south tracking, the tracking axis is therefore aligned in the east-west direction, and the aperture surface rotates between north and south. In contrast, with east-west tracking, the tracking axis is aligned in the north-south direction, and the aperture surface rotates from east to west. [29]

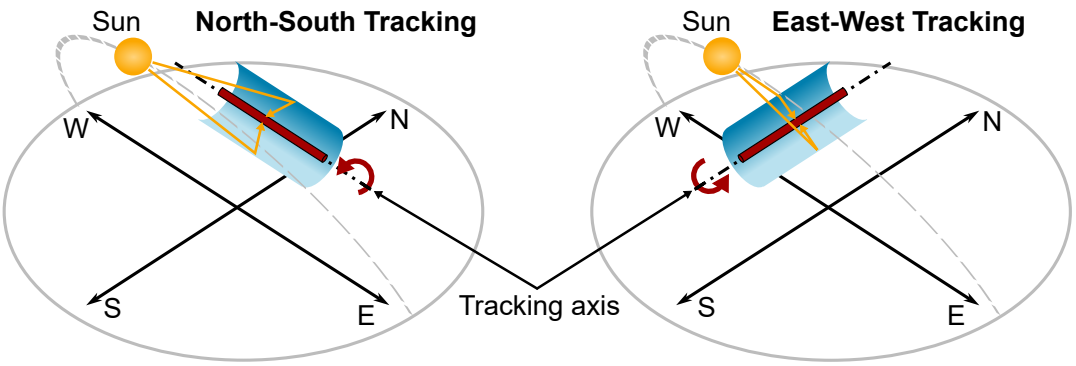

Figure 2.11.: Different tracking methods for PTCs

As shown in Figure 2.8, each SCA contains a drive pylon, which allows several SCEs to be rotated simultaneously. For this purpose, an electric motor with a gearbox is integrated into the drive pylon, which enables either hydraulic or pneumatic tracking. To keep the forces and energy required for tacking to a minimum, the axis of rotation and the center of gravity should be at the swivel points. [2]

Figure 2.12 shows the collector angle during the day for east-west sun tracking. In the morning at sunrise, the collector is moved from the stow position α_{stow} to the start position α_r in a fast, continuous motion. The sun is then tracked until sunset α_s. This happens in a slow, incremental motion. This means that the angular position is not changed continuously but is adjusted to the sun's current position every 20 to 40 s. To determine the sun's position, algorithms that approximate the sun's current position or direct measurement technologies with inclinometers or magnetic strip monitoring are used. After sunset, the collector is brought back into the stow position quickly and continuously until the next power plant starts up. [17]

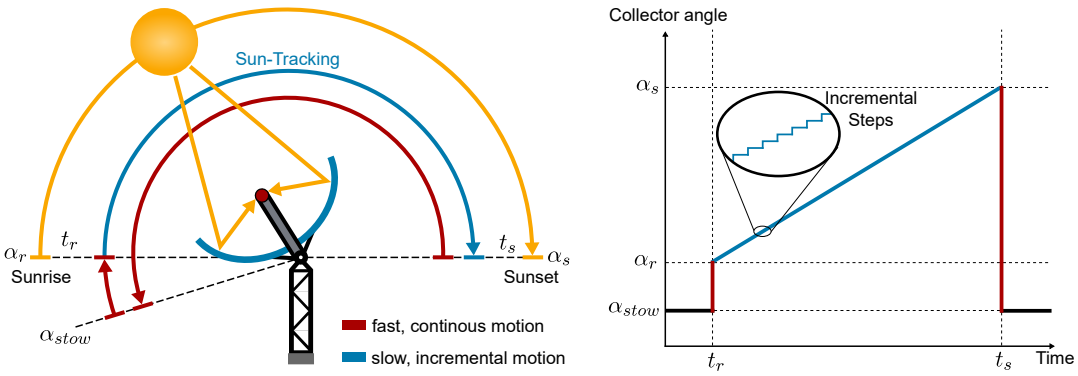

Figure 2.12.: Collector angle of a PTC tracking the sun

2.1.4. Current Status and Perspective of CSP

There are more than 143 CSP projects worldwide, of which 114 are in operation, 20 are decommissioned, and nine are still under construction as of 2023. Spain, the USA, and China are the leading countries regarding installed capacity (see figure 2.13). In Spain, 51 active CSP projects have a total capacity of 2300 MW, accounting for almost a third of global installed capacity. In the USA, there are 26 projects with a total capacity of 1500 MW, and in China, the total capacity is 906 MW, while several projects are currently still under construction. A total of 7889 MW of CSP capacity has been installed worldwide. 72 % of the installed capacity are PTC power plants, 23 % are solar tower power plants, and 5 % are linear Fresnel power plants. [4]

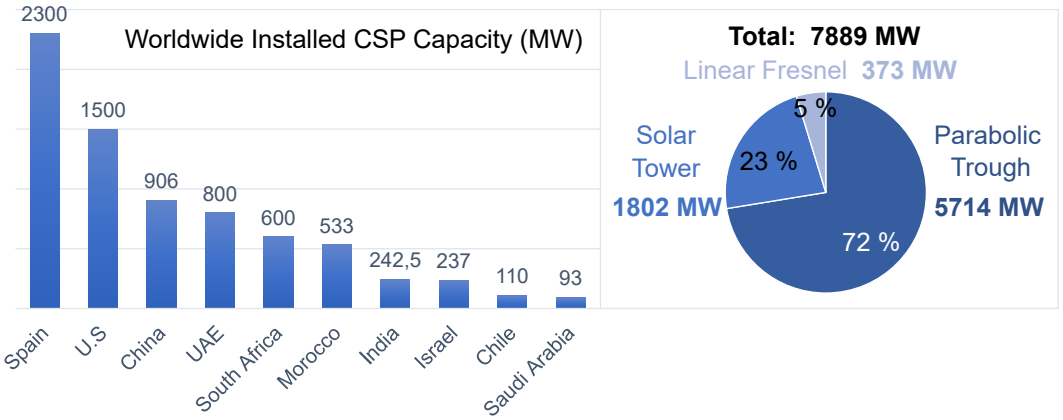

Figure 2.13.: Global installed CSP capacity distribution

Forecasts indicate strong growth in the installed capacity of CSP. According to the European Solar Thermal Energy Association, the International Energy Agency, and

Greenpeace, the forecast indicates that Concentrated Solar Power (CSP) could cover 8 to 11,8 % of global energy demand by 2050. However, this assumes an extreme growth in capacity [30]. The Levelized Cost of Energy (LCOE) could fall to 0,05 $/kWh [31]. In particular, the combination of CSP, thermal energy storage, and other renewable energies such as photovoltaics and wind in hybrid systems already has a low LCOE of around 0,1 $/kWh. [4]

2.2. Rotation and Expansion Performing Assemblies

This section explains the basics and common variants of the REPAs in PTCs. In addition, it presents various test rigs and the results obtained in these on aging processes and the service life of REPAs.

As described in subsection 2.1.3, the parabolic trough tracks the sun on one axis on a sunny day. The absorber pipe must, therefore, be connected to the header pipes with a flexible pipe connector that can compensate for this rotation. At the same time, the translational movement due to the thermal expansion of the absorber pipe must be compensated. When the power plant starts up in the morning, the absorber pipe expands as the HTF temperature rises and contracts again when the temperature falls. Flexible pipe connectors, known as Rotation and Expansion Performing Assemblies, compensate for these two movements. REPAs are dynamic seal systems that are subject to wear over time, making their mechanical durability a key factor in the system's long-term reliability. Despite their critical role, reliable maintenance strategies for REPAs are often lacking, which highlights the need for systematic condition monitoring and predictive maintenance approaches.

Two of these REPAs are required per SCA. With a service lifetime of 25-30 years, this results in a lifetime of 10,000 daily cycles, as shown in Figure 2.12. REPAs must be able to endure temperatures of up to 400 °C and pressures of up to 35 bar, as well as the forces and torques of the rotation and expansion. Due to these high requirements, REPAs are among the most mechanically stressed components in a PTC power plant and are prone to failure. Effective maintenance strategies are important to minimize possible leaks, fires, and associated downtime. [17]

The two types of commercially used REPAs are presented below. These include the Rotary Flex Hose Assemblies and the Ball Joint Assemblies.

2.2.1. Rotary Flex Hose Assemblies

Rotary Flex Hose Assemblies (RFHAs) consist of three main components, as shown schematically on the left side in Figure 2.14. The three components are a flexible metal hose, a swivel joint, and a torque-transmitting interface, commonly known as a torque sword.

The metal hose has a corrugated structure along its length, allowing flexibility. To minimize heat losses, it is thermally insulated. The swivel joint connects the fixed pipe and the rotating corrugated hose, which is driven by the torque sword. This joint has a single rotational degree of freedom and is anchored to a rigid support, ensuring stability. The torque sword, typically a flat steel beam, maintains the connection between the SCA and the swivel joint, transmitting rotational movement. As shown in Figure 2.14, the swivel joint compensates for rotational movement, while the corrugated hose absorbs translational displacement. [17]

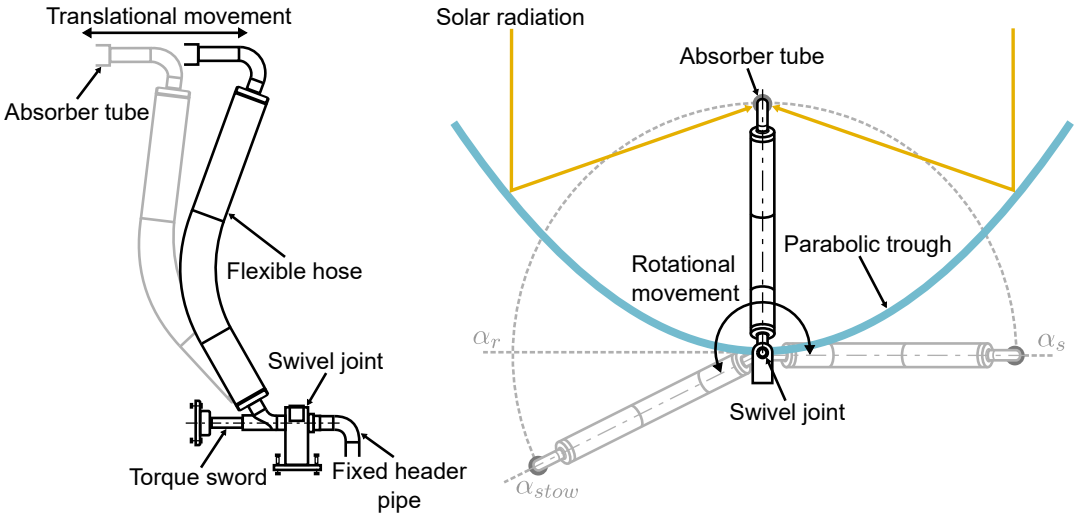

Figure 2.14.: Schematic structure and movement of an RFHA

2.2.2. Ball Joint Assemblies

Ball joint assemblies (BJAs) usually consist of three individual ball joints connected. Figure 2.15 shows this typical structure. One ball joint is attached to the HCE, another to the fixed header pipe, and a third ball joint is placed centrally between the other two using two pipe sections. Each ball joint has three rotational degrees of free-

dom so that this arrangement can compensate for both rotational and translational movement.

The right side of Figure 2.15 shows a cutaway of a typical ball joint. The ball joint consists of two main components. A pipe with a spherical end and a housing into which this pipe is inserted. The pipe is held in place by two compression seals. An injectable sealant, for example, graphite, can be injected through a fill coupling in the housing. A fill connection plug closes this injection point. This allows the injectable sealant to be refilled, making the ball joint serviceable. This maintainability is one of the reasons why BJAs are used more often commercially than RFHAs. [17]

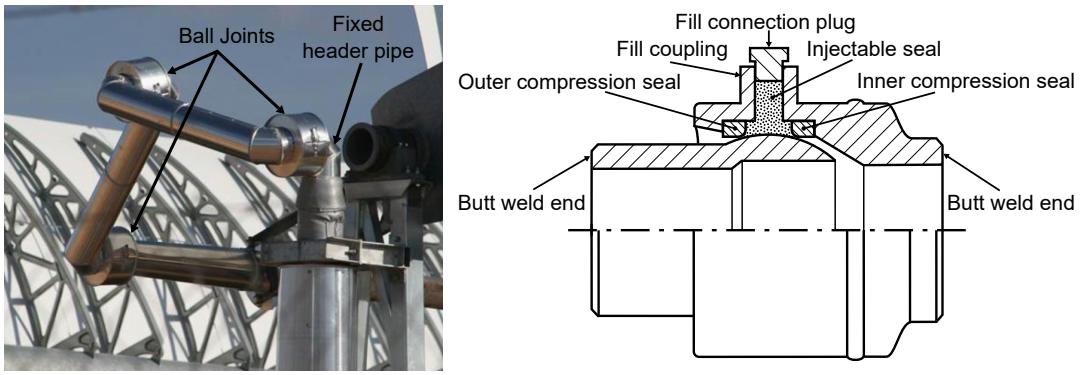

Figure 2.15.: BJA [32] and cutaway of a ball joint

According to the manufacturer *Advanced Thermal Systems*, routine maintenance for ball joints is minimal. Regular maintenance mainly includes inspections for leaks, lubrication of the fill connection plugs, and cleaning during system shutdowns to prevent the buildup of packing material or debris. If leaks occur, additional sealing packing material can be added. The graphite packings are inserted via the filling openings. These graphite packings expand when heated and seal any leaks that occur. Excessive addition of packing should be avoided so as not to affect the torque of the joint adversely. [33]

2.2.3. REPA Test Rigs and Measurement Methods

As already described, REPAs are among the most mechanically stressed components in a PTC Power Plant. Therefore, tests under operating conditions are required before field usage. Many different test rigs have already been constructed for this purpose, some of which are presented in this subsection.

Senior Felxonics GmbH, a manufacturer of flexible connectors for PTCs, tests RFHAs on a kinematic test rig. Figure 2.16 shows the setup of this test rig. The swivel joints are wetted with stagnant HTF that can be heated up to 550 °C. The maximum pressure is 40 bar. The flexible hose is filled with water at ambient temperature and can also be pressurized up to 40 bar. The kinematic unit allows the RFHA to be rotated between -120 ° in the stow position and up to 120 ° in the end position. At the same time, a thermal expansion movement is simulated. To do this, the kinematic arm is moved translationally from -14.5 ° in the cold position to the maximum warm position at 5.5 °. Two load cells are installed to collect data on forces and moments. One is under the swivel joint, and the other is between the flexible hose's upper end and the HCE. [17]

As no mass flow circulates through the RFHA, the reliability of the test method for predicting the aging effects of the tested components is reduced. For this reason, the flex hoses are tested separately in another test rig. The flex hoses are subjected to a circulating HTF with a temperature of up to 450 °C and a pressure of up to 40 bar. At the same time, the translational movement by thermal expansion can be simulated. However, the flex hoses are not rotated in this test rig. [17]

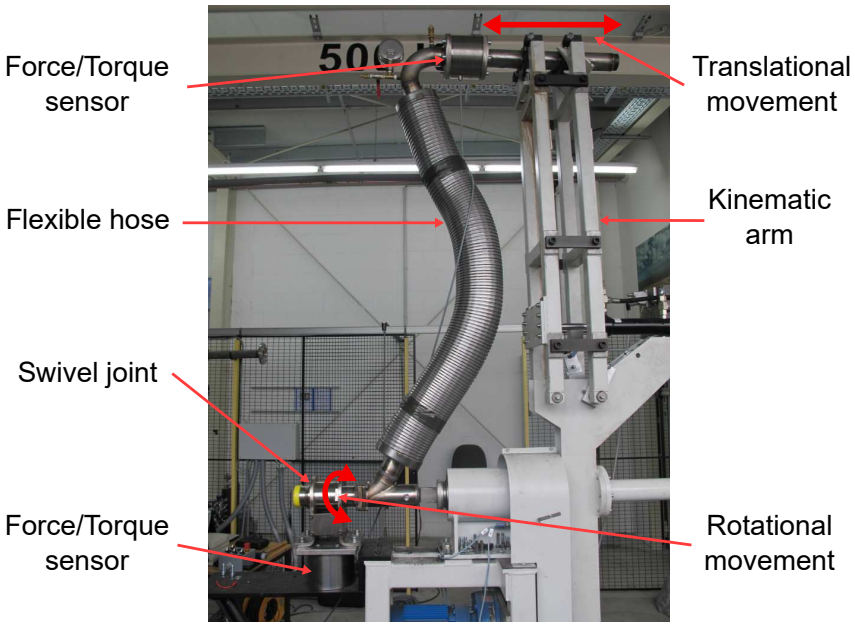

Figure 2.16.: *Senior Felxonics GmbH* test rig for RFHAs [17]

To test a new flexible interconnect system developed by *Senior Felxonics GmbH* for PTCs, another test rig was set up at the University of Wisconsin, Madison. The RotationFlex Triple System (RF-Triple®) installed in the test rig can be seen in Figure 2.17. It consists of three separate flexible hoses. One hose compensates for the translational movement caused by thermal expansion, while the other two hoses compensate for the necessary rotation of 180 ° in two 90 ° steps each. Molten salt (60 % $NaNO_3$, 40 % KNO_3) is used as the HTF. During the lifetime tests, the system is moved between 0 ° and 180 °. Temperatures of up to 550 °C and pressures of up to 31.5 bar are reached. The test rig has torque, force, temperature, pressure, and salt level measurement sensors to record data. The RotationFlex Triple system achieved more than 10,000 cycles without failure in the tests. The results show that the flexible interconnect system is a promising alternative to conventional BJAs, which are technically unsuitable for molten salt applications. [34]

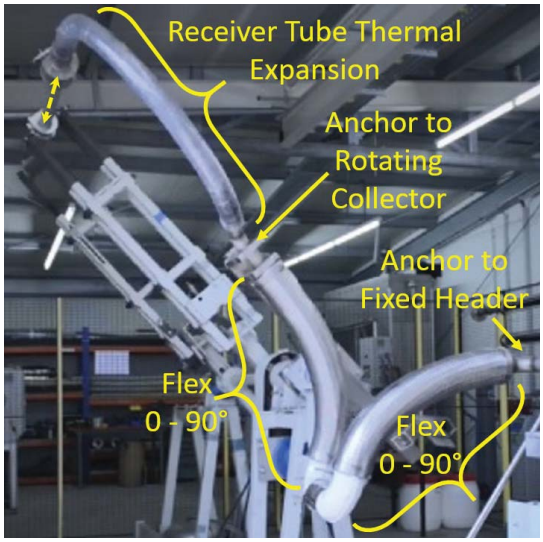

Figure 2.17.: *Senior Felxonics GmbH* Test Rig for RotationFlex triple system [34]

Abengoa Solar has also developed a test rig, shown in Figure 2.18, for testing various REPAs for PTCs with molten salt as the HTF. The test rig is equipped with sensors for torque, force, temperature, pressure, and salt level and also exposes the test objects to stagnant molten solar salt (60 % $NaNO_3$, 40 % KNO_3). Pressures of up to 40 bar and temperatures of up to 500 °C are achieved. The test device allows a rotation of 215 ° and a thermal length change of 600 mm, whereby the actual test range was set between 200 mm to 600 mm. The movements take place simultaneously,

with a cycle time of two minutes. [35]

Both RFHAs and BJAs can be tested in the test rig. More than 13 different variants have already been tested. The success was limited as most assemblies showed leaks after about 2000 to 3000 cycles. No pliable seal material could be found that was compatible with 500 °C molten salt. Therefore, in addition to the conventional REPAs, an alternative technology without ball or swivel joints, consisting of two flexible hoses and a torque transfer arm, was investigated. [35]

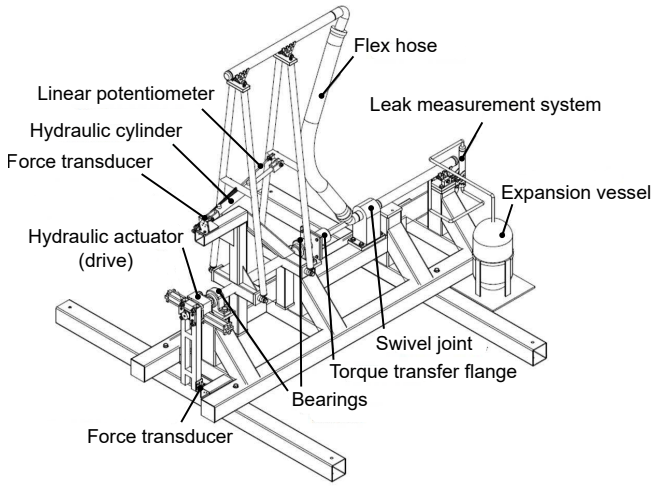

Figure 2.18.: *Abengoa Solar* test rig for RFHAs and BJAs [35]

Another test rig was developed by Dong et al. as part of the National Key Research and Development Program of China [36]. In the test rig shown in Figure 2.19, BJAs are tested with a common heat transfer oil as HTF. The ball joints are installed on the mechanical platform, which is equipped with the necessary motors and control devices for rotational and translational movement. The ball joints can rotate from 0 ° to 215 ° as well as swivel from -7 ° to 7 °. In addition, various measurement devices are installed to continuously measure torque, leakage rate, temperature, and pressure. Accelerated life tests are carried out under realistic conditions with oil temperatures up to 393 °C and pressures up to 41 bar generated by the thermal oil control device. [36]

The tests simulated around 5,000 operating cycles, corresponding to a service life of 12 years. In pure rotation mode, the torque was higher than in pure swivel mode. The

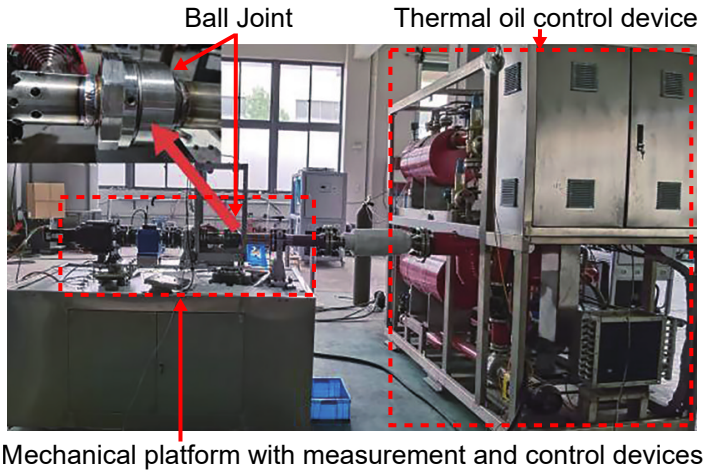

Figure 2.19.: *CGN Solar Energy Development* test rig for ball joints [36]

greatest load occurred in combined motion, whereby only eight cycles were performed this way. The maximum measured leakage rate was 50.2 μmol/mol, which is significantly below the permissible limit values. It was, therefore, possible to confirm the reliability of the ball joint under the tested conditions. [36]

2.3. Fundamentals of Load Cells

Sensors determine an unknown measured variable, such as force or torque. This section describes the fundamentals of load cells used to measure these variables. First, the general mode of operation and the different decoupling methods are explained. Furthermore, the different measurement inaccuracies are explained using the characteristic load cell curve.

2.3.1. Mode of Operation

Load cells are used to measure forces and torques. The classic measurement chain consists of a sensor that converts the physical forces and torques into a measurement signal, a signal amplifier, and an indication device with which this amplified signal can be read out. [37]

Figure 2.20 shows this measuring chain. The input signal of the force or torque is converted into a voltage using a strain gauge. The strain gauge is deformed by ex-

ternal forces and torques, causing the ohmic resistance to change. This change is measured using a Wheatstone bridge circuit [38]. A measuring amplifier is used as the differential voltage measured in this way is usually very small. This provides auxiliary energy as a supply voltage U_S, whereby the sensor outputs the signal u_s.

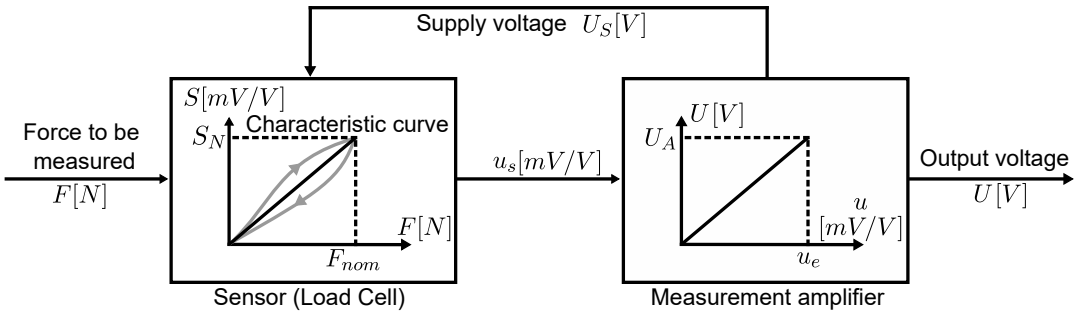

Figure 2.20.: Measuring chain for force measurement with a load cell

The output signal u_s is calculated using the equation 2.4. The force is multiplied by the slope of the characteristic load cell curve. This slope is given by the nominal characteristic value S_N divided by the nominal force F_{nom}. The output signal is, therefore, equal to the differential voltage of the Wheaton bridge U_D divided by the supply voltage of the amplifier U_S and is specified in mV/V. [37]

$$u_s = \frac{S_N}{F_{nom}} \cdot F = \frac{U_D}{U_S} \tag{2.4}$$

The output signal u_s of the load cell is the input signal for the measuring amplifier. This amplifies the signal and outputs a voltage depending on the input force. The measuring range end value U_A specifies the maximum measurable force. Analogous to the load cell, a characteristic curve also describes the measuring amplifier. The gradient of this characteristic curve is calculated from the measuring range end value U_A and the input sensitivity u_e, resulting in equation 2.5 for the characteristic curve of the entire measuring chain. The characteristic values of the load cell and the amplifier are combined to form the scaling factor k, resulting in a direct linear correlation between the measured force and output voltage. [37]

$$U = \frac{S_N}{F_{nom}} \cdot \frac{U_A}{u_e} \cdot F = k \cdot F \tag{2.5}$$

2.3.2. Decoupling Methods

In multi-axis load cells, several strain gauges are connected to measure forces and torques in several dimensions. External mechanical loads do not only act on individual strain gauges. The loads are distributed across the sensor system, meaning several channels react to a single load. For a measurement to remain precise, it is necessary to negate these so-called coupling effects through mathematical or structural measures. For this purpose, decoupling methods such as matrix or structural decoupling can be used.

In matrix decoupling, the raw signals of all channels are processed with an individual decoupling matrix for each sensor. The coupling effects are mathematically filtered out. The measured values F_{dyn} of the load cell follow from equation 2.6. K is the fully equipped decoupling matrix, and U is the signals of the individual channels of the load cell. [39]

$$F_{dyn} = K \cdot U \tag{2.6}$$

With structural decoupling, the sensor channels are mechanically designed to be independent. Each force or torque component is assigned directly to a specific channel. For example, a force in the x-direction only leads to a signal in the corresponding channel without influencing other channels. However, even with a structurally decoupled load cell, a small amount of crosstalk often remains between the individual channels. Analogous to matrix decoupling, this can be eliminated using a crosstalk matrix to ensure high sensor accuracy. [40]

2.3.3. Measurement Uncertainties

The linear relationships between the input force and output voltage presented in the previous subsections, such as in equation 2.5 and 2.6, are never fully valid in reality. Various physical effects and external influences on the sensor lead to measurement uncertainties. Figure 2.21 shows the characteristic curve of a load cell with various uncertainties.

A central variable is the zero signal, which represents the output signal of an unloaded sensor. A distinction is made between the zero signal without mounting materials S_0 and the mounted zero signal S_{F0}. Changes in the zero signal can be caused by mount-

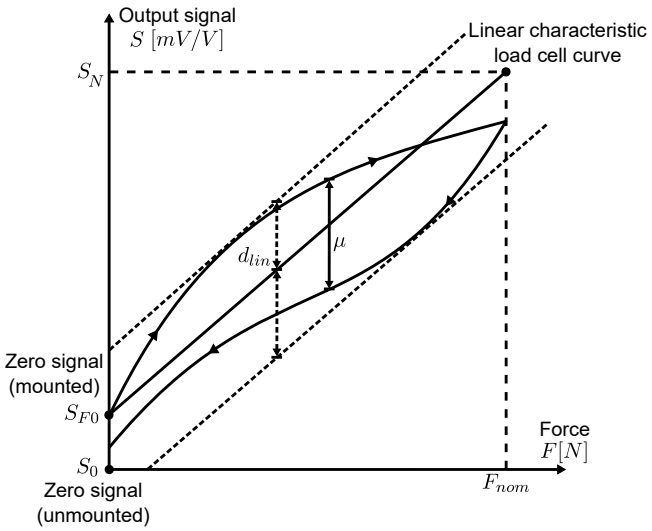

Figure 2.21.: Schematic representation of load cell uncertainties

ing on uneven surfaces or deformations caused by tightening the mounting screws. To compensate for this effect, either the zero signal specified in the calibration is subtracted from the measurement signal or an offset is set at the start of a measurement. Regular offset adjustments allow changes to the zero signal during operation to be considered. [39]

Non-linearity refers to the sensor signal's maximum deviation d_{lin} from an ideal linear characteristic curve. It occurs when the actual characteristic of the sensor is not exactly linear. A similar effect is described by hysteresis μ. It describes the maximum difference in the sensor signal between an increasing and a decreasing load up to the nominal force F_{nom}. This is caused by small, irreversible deformations of the material inside the sensor. After a load cycle, the zero signal can shift, which must be considered in measurement applications with cyclical loads. [39]

Creep describes the time-dependent change in the sensor signal under constant load. This effect typically occurs after a long period of loading. Time-dependent material properties, in particular, cause the viscoelastic behavior of the strain gauges and the surrounding material [38]. Creep is usually not detected during calibration, as the loads are often only applied briefly. However, this effect must be considered for applications with permanent loads.

Temperature influences also affect measurement accuracy. Deviations from the calibration temperature lead to uncertainties that can be divided into two main aspects, as shown in Figure 2.22. The temperature effect on the zero signal TK_0 leads to a parallel shift of the characteristic curve. In contrast, the temperature effect on the calibration constant TK_C causes a change in the slope of the curve. Depending on the temperature change, both effects can positively and negatively influence the output signal. TK_0 can be compensated for using an offset correction, whereas TK_C requires temperature measurement and mathematical adjustment. [39]

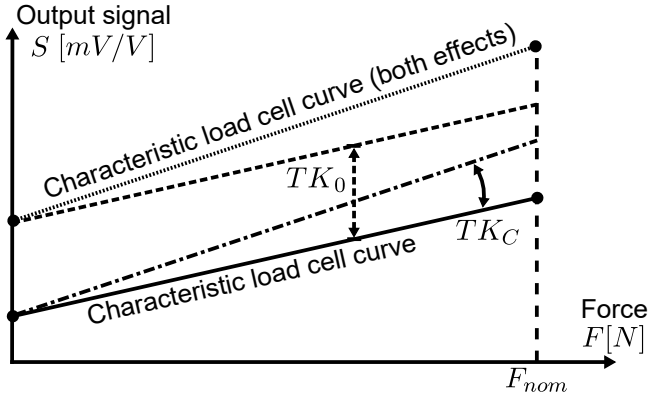

Figure 2.22.: Temperature effects on the characteristic curve of a load cell

3. Experimental Setup

This chapter introduces the REPA test rig located on the PSA in Spain. First, the general structure and possible process parameters are explained. The SCADA system for controlling the test rig and the possibilities for data acquisition are discussed. Furthermore, the sensors used, particularly the load cells and the REPA types tested, are presented.

3.1. REPA Test Rig

The REPA test rig is used to perform accelerated yet realistic lifespan tests on different types of REPAs. Two REPAs are simultaneously rotated and translationally moved while hot pressurized HTF flows through them. Both RFHA and BJA can be tested. Around 400 to 570-day cycles can be simulated per day. This means that the effects of a lifespan of 25 years resulting in 10,000 cycles can be investigated in less than a month.

An overview of the test rig is shown in 3.1. The test rig can be divided into three main parts. The Main Assembly with the Kinematic Unit provides the rotational and translational movement. The HTF Cycle ensures the correct HTF temperature, pressure, and mass flow, and the Supervisory Control and Data Acquisition System (SCADA) for data collection, monitoring, and control of the test rig.

3.1.1. Main Assembly

The main assembly consists of the kinematic unit, the traverse, and two REPAs mounted on the two tables of the main frame. Figure 3.2 shows the main assembly with two RFHAs installed.

The kinematic unit consists of the drive pylon, the hydraulic unit, and four hydraulic cylinders. Two hydraulic cylinders are installed in the center of the drive pylon and are used to generate the rotational movement. The other two hydraulic cylinders are

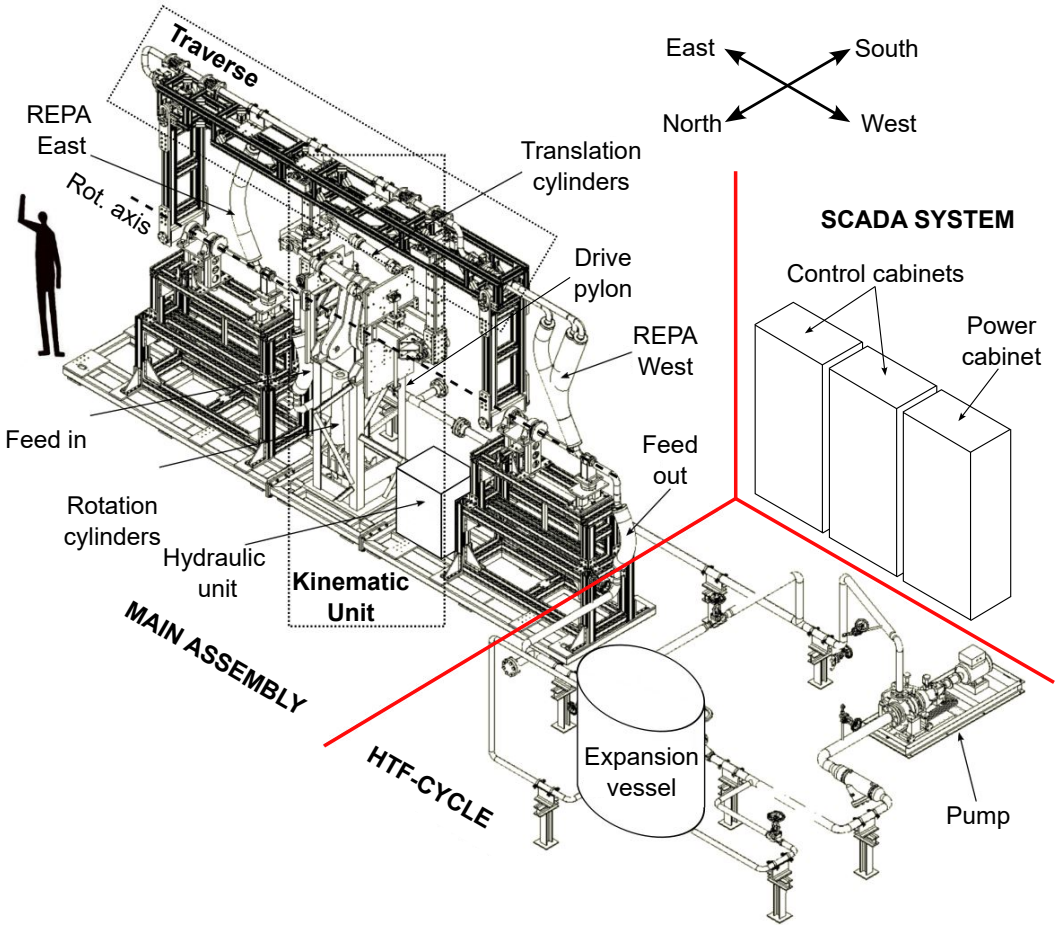

Figure 3.1.: REPA test rig overview [39]

positioned at the top of the drive pylon and enable translational movement. The two drive pylon arms connect the kinematic unit to the traverse.

The traverse connects the two upper ends of the REPAs. The distance between the axis of rotation and the traverse is the same as that between the axis of rotation and the receiver of a PTC. In order to simulate different collector types, the height of the traverse can be set between 1.5 m and 2.3 m. It is attached to the frame of the main assembly with the two outer swivel arms. With the help of the attached drive pylon arms, the entire traverse and, thus, the connected REPAs can be set in motion. The traverse can be rotated around the rotational axis in the north and south directions and moved translationally in the east and west directions. Maximum angles for rotation are from -23 ° in the stow position to 186 ° in the end position. The design allows

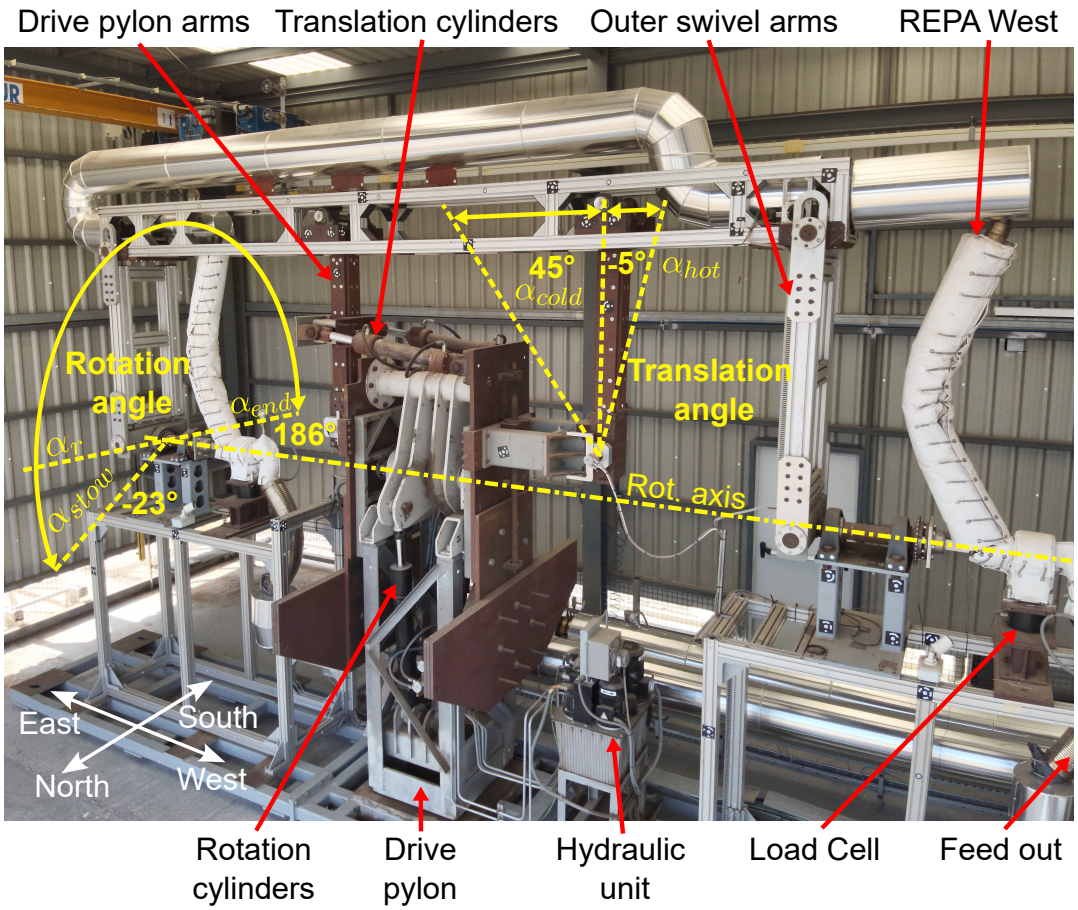

Figure 3.2.: REPA test rig main assembly with kinematic unit and traverse

a translational movement of 50 ° whereby only a fraction of this is used in operation. The maximum possible translation angle in the west direction is -5 °. With a traverse height of 1.72 m and a translation angle of 12 ° in the east direction, a translational movement of 500 mm is achieved. [39]

The hydraulic system is responsible for all these movements and has been designed to simulate regular cycles and swift rotation steps to approximate dumping and break-away torques. To minimize hydraulic damping, the hydraulic unit is placed as close as possible to the cylinders, and where possible, rigid tubes are used for connection.[39]

During installation, the REPAs to be tested are welded to the traverse pipe and the feed-in or feed-out pipes. In the case of the RFHA, the Swivel joint is firmly attached to the table of the main assembly. A load cell is placed between the swivel joint and

the table to measure the force. For a BJA, the straight pipe section of the lowest ball joint is attached to the load cell. The exact structure of this assembly is explained in the sensor mounting plate subsection 3.2.3. Flex hoses are used for the two feed connections to minimize possible influences on the force measurement. Movements of the pipe connections due to high pressures and thermal expansion at elevated temperatures would otherwise result in forces that could falsify the force measurement results. [41]

3.1.2. HTF Cycle

The HTF cycle consists of three main components. The pipe system has a pump, an expansion vessel, and electric heaters. The pump ensures the flow of the HTF in the circuit. It is designed for a mass flow of 6 m^3/h to 60 m^3/h at pressures of up to 40 bar. For safety reasons, a bypass that shortcuts the main assembly is installed in the pipe system. This allows a quick separation between the pump and the main assembly in case of a failure.

An expansion vessel is connected to the pipe system to regulate the pressure. The expansion vessel is used to compensate for the thermal expansion of the HTF. For this purpose, nitrogen is used as an inert gas. It is admitted from a pressurized gas cylinder or vented as needed. The nitrogen system can also be used to adjust the process pressure. The adjustable pressure range is between 1 and 40 bar.

To heat the HTF, 10 high-performance electric band heaters with an output of 3500 W each are installed in the test rig. These heaters are attached to the pipe leading to the main assembly before the feed-in. In order to achieve the lowest possible heat loss, all pipes are covered in 120 mm insulation. This way, a maximum temperature of 450 °C can be achieved. *Therminol® VP-1* oil with a maximum permissible temperature of 400 °C was used for the test campaigns carried out in this work. However, using silicone oils with higher maximum temperatures is also conceivable in this test rig. [39]

3.1.3. Scada System & Data Aquisition

The SCADA system monitors and controls the entire test rig, including the kinematic unit and the HTF cycle. Figure 3.3 shows an overview of the components

of this system. The central element is the Programmable Logic Controller (PLC) SIMATIC S7-300 from *Siemens*. All sensors and actuators are connected to this PLC via various interfaces, either analog or digital. This PLC controls the speed of the HTF pump, records measurement data, and sends control commands to the servo controller. The servo controller manages the speed of the motors in the hydraulic system and controls the movement of the cycles. [42]

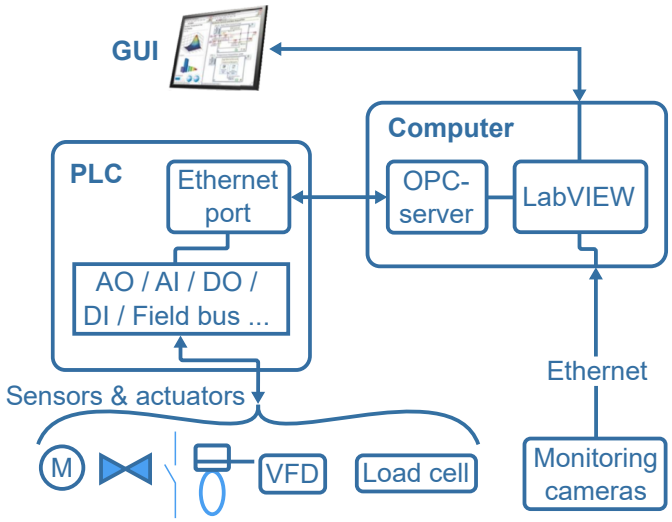

Figure 3.3.: SCADA system components overview [42]

An Open Platform Communications (OPC) server allows the reading and writing of PLC variables and is connected to a Graphical User Interface (GUI) programmed in *LabVIEW*. This GUI enables remote control of the test rig. Visual monitoring can also be carried out with cameras connected via an ethernet connection. A servo drive actuates the system's rotation, while an inverter drive system controls the translational movement. The direction of movement of the traverse system is determined by 4/3 directional control valves, which control whether the cylinder pistons are retracted or extended. During the changeover points at around 35 ° and 133 °, the movement of the traverse slows down when a piston changes from pushing to pulling or vice versa.[42]

Figure 3.4 shows the PLC extension installed in December 2024. The existing PLC system had to be extended to integrate the new load cells. This extension also provides enough space to install further sensors, such as additional load cells or cameras, to monitor the REPA test campaigns. The second cabinet is connected to the PLC

system via a PLC module connector in the middle of the cabinet. A SITOP PSU100S is used as the power supply unit and installed in the cabinet's upper part. The two newly integrated load cells are connected in the lower area. The individual analog inputs can thus be integrated into the existing PLC system.

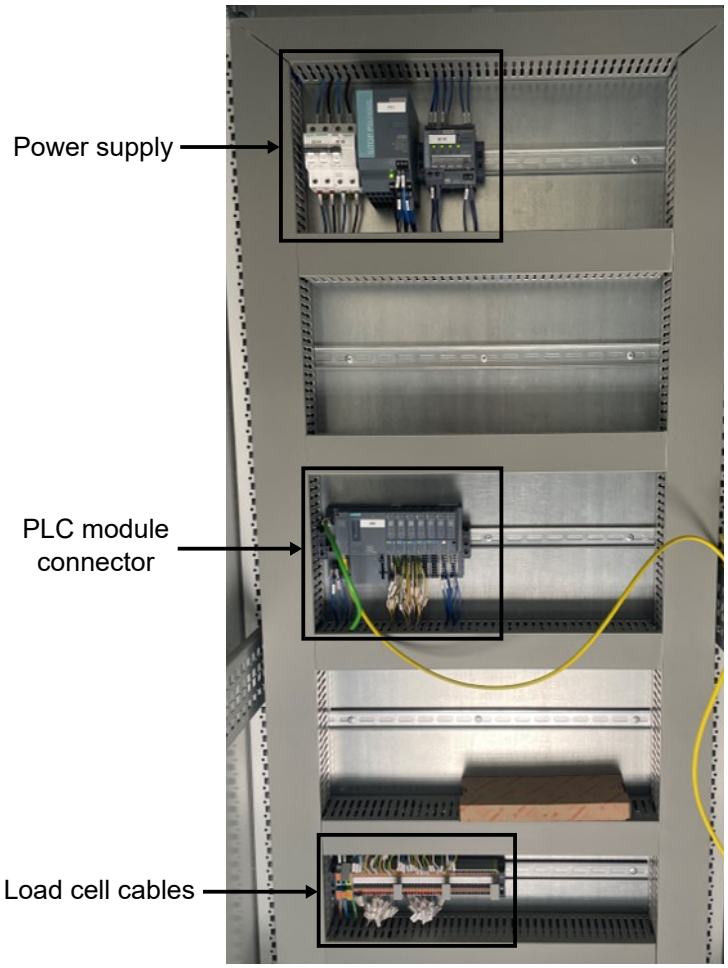

Figure 3.4.: PLC extension cabinet and load cell connections

3.2. Sensors for Force Analysis

The REPA test rig contains a wide range of sensors for measuring temperatures, pressures, positions, forces, and torques. The load cells that collect data for forces and torques are particularly important for this work. In this section, the sensors used and their properties are presented

To analyze the causes and mechanisms behind REPA wear and eventual failure, two load cells are used to measure the forces and moments exerted by each REPA on its bearings. The REPAs, labeled west and east, are each mounted on a load cell. These load cells are called lower east and lower west load cells.

As part of this work, the load cells previously used in the test rig were replaced with new ones. These new load cells provide more accurate measured values due to higher temperature stability and the measuring ranges adapted to the forces expected in the test campaigns. Since the force analysis also includes test campaigns carried out with the old load cells, both models are presented here.

3.2.1. Six Axis Circular Load Cell - K6D175

The six-axis circular load cell K6D175 from *ME-Messysteme* measures forces and torques. Figure 3.5 shows the load cell on the left and the amplifier used for data acquisition on the right. As no integrated amplifier is installed, the GSV-1A16USB K6D amplifier is used.

Figure 3.5.: Six axis load cell K6D175 [43] and signal amplifier GSV-1A16USB K6D [44]

Table 3.1 shows the load cell specifications. As the largest forces are expected in the z-direction, the largest capacity of 20 kN was selected here. The nominal temperature range of the load cell is between -10 °C and 70 °C, and the maximum service temperature range is between -10 °C and 85 °C. The maximum supply voltage is 5 V, and the overload capacity is 300 % of the full capacity.

Table 3.1.: Force specifications for six axis circular load cell K6D175 [43]

	F_x	F_y	F_z	M_x	M_y	M_z
Capacity	10 kN	10 kN	20 kN	1000 Nm	1000 Nm	2000 Nm
Nominal value @ FS	0.5 mV/V	0.5 mV/V	0.5 mV/V	0.5 mV/V	0.5 mV/V	0.5 mV/V

3.2.2. Six Axis Circular Load Cell - M4347K5

To carry out precise force measurements, the six-axis circular load cell M4347K5 from *Sunrise Instruments* is integrated in place of the old load cells. The sensor was selected based on the results of previous force measurements on the REPA test rig. This means that the load cell is optimally matched to the requirements of future test campaigns. Figure 3.6 shows the load cell. It has a fixed and a loading side. The forces are measured in relation to the coordinate system positioned in the center of the loading side. The force in the direction of the axis and the moment around this axis are measured for each of the three axes. The analog output is provided via a *LEMO* connector.

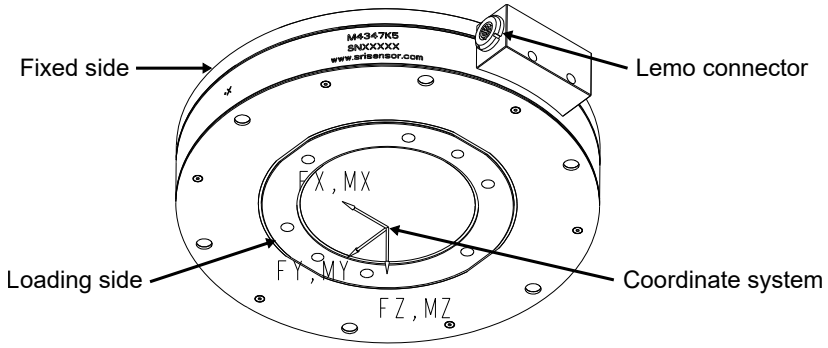

Figure 3.6.: Six axis circular load cell M4347K5 [45]

Table 3.2 shows the force specifications of the load cell. Adjusting the force capacity ensures that measurement accuracy and reliability are maintained even under specific load conditions. The most significant forces occur in the z-direction, which is why the force capacity for F_z is 6 kN. A capacity of 3 kN is sufficient for the other two directions. The highest torques are expected around the x- and y-axis, so the capacity is 1500 Nm. At Full Scale (FS), the output is 5 V. The output is differential and centered at 0 V. This means that positive forces at the full capacity result in an output of +5 V, and negative forces at the full capacity result in an output of -5 V. The overload capacity is 1000 % of the full capacity. The overload capacity is the maximum possible load a sensor can take before breaking. If, for example, forces

above the standard capacity are applied during installation, the sensor is not directly destroyed.

Table 3.2.: FForce specifications for six axis circular load cell M4347K5 [45]

	F_x	F_y	F_z	M_x	M_y	M_z
Capacity	3 kN	3 kN	6 kN	1500 Nm	1500 Nm	1000 Nm
Resolution	1 N	1 N	1.5 N	0.16 Nm	0.16 Nm	0.22 Nm
Output @ FS	5 V	5 V	5 V	5 V	5 V	5 V

The load cell has an integrated amplifier, meaning no external signal amplifier is required. This allows the load cell to be connected directly to the PLC and the SCADA system. A *LEMO* connector with 16 pins is plugged into the load cell to connect the individual cables to the PLC. As the sensor is structurally decoupled, two cables are used for each force or torque's positive and negative channels. The sensor, therefore, has a total of 16 cables. The *LEMO* connector cable is shielded to prevent possible interference. Figure 3.4 in the subsection on the Data Acquisition and Scada system shows the integration of the two load cells to the PLC extension.

As the HTF is heated up to 393 °C during the test campaign, the pipes and connectors between the load cell and pipe also heat up. In previous tests, load cell temperatures between 60 °C and 80 °C were reached. With a maximum operating temperature range of -40 °C to 100 °C, these temperatures are no problem for the load cell. The compensated temperature range is between 20 °C and 70 °C. The temperature drift in this temperature range is less than 3 %. Larger measurement uncertainties are therefore expected at temperatures above 70 °C. A measurement uncertainty estimation, including these temperature drift uncertainties, is shown in subsection 4.1.1.

Other important sensor specifications for subsequent calibration are crosstalk, non-linearity, and hysteresis. The load cell M4347K5 has a crosstalk between the various measured variables of up to 5 %. The non-linearity and hysteresis are each 1 %. [45]

3.2.3. Load Cell Mounting

In order to obtain measurement results that are as replicable as possible, the load cells must be installed on a robust, flat surface. Figure 3.7 shows one of the M4347K5 six-axis load cells installed in the test rig.

The load cell is attached to the base frame of the main assembly using a specially manufactured bottom plate. The bottom plate is firmly screwed to the loading side of the load cell. The fixed side is then screwed to the load cell top plate. In the case of a BJA, a specially manufactured load cell connector is attached to this top plate. This connects the top plate with the bottom feed-in or bottom feed-out, leading to the lower ball joint. In the case of an RFHA, the swivel joint housing is attached directly to the load cell top plate. This positioning allows the forces and torques to be measured as close as possible to the swivel or ball joint.

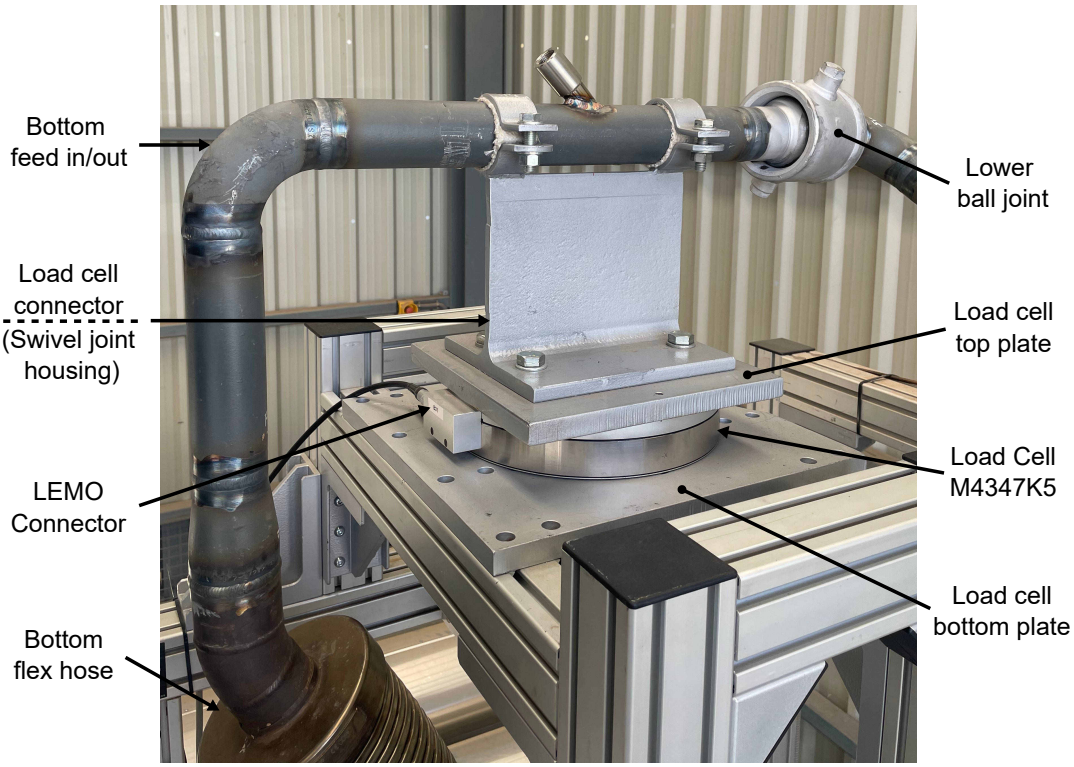

Figure 3.7.: Integration of M4347K5 load cell into BJA without insulation

The integration of the new load cells results in a change to the coordinate system. Figure 3.8 shows the coordinate systems for both load cells, with the arrows representing the direction of positive values. The test campaign with RFHAs analyzed in this work was carried out with the K6D175 load cells shown on the left. The BJA test campaign was carried out with the M4347K5 load cells shown on the right. When analyzing and comparing the results, note the change in the coordinate systems. The x-axis is aligned to the north, and the z-axis is to the top on both sides. For the

K6D175 load cell, the y-axis is oriented to the west, and for the M4347K5 load cell to the east.

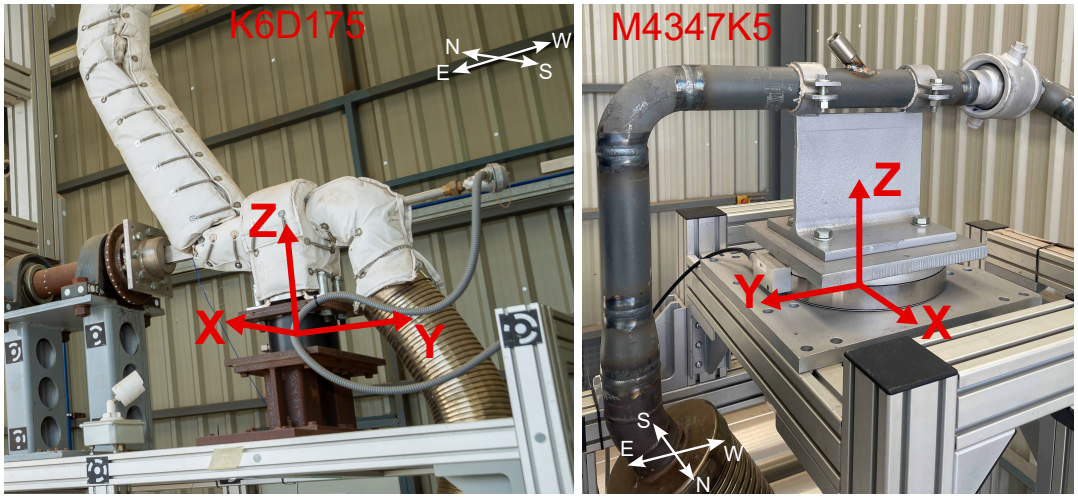

Figure 3.8.: Coordinate systems of the K6D175 and the M4347K5 Load Cell

3.3. REPA Installation

This section presents the two REPA assemblies used. First, the RFHA that was already installed at the beginning of this work is described. This is followed by a more detailed description of the integration of the BJA, for which the pipe installation was designed as part of this work.

3.3.1. Rotary Flex Hose Assembly

In the first test campaign, an RFHA is examined as a REPA. Identical RFHAs are installed on both the east and west sides, as seen in the main assembly figure 3.2. The swivel joint is firmly connected to the top plate of the load cell. The torque sword is welded directly to the piece of pipe that leaves the swivel joint. Both components are aligned coaxially to the test rig's rotation axis. The corrugated flex hose and the swivel joint are insulated to minimize heat loss. As the RFHAs were already installed in 2022, the installation process is not described in detail here.

3.3.2. Ball Joint Assembly

In the second test campaign, a BJA is examined as the REPA. The ball joint 2"-S2-SWW-400H-70-20 from *Advanced Thermal Systems* is installed for this purpose. First, the RFHAs are dismantled so that two BJAs can replace them. After removal, the dimensions of the feed-in and feed-out connections and the load cell's new attachment are determined to design a pipeline for the ball joints. Based on these dimensions, an isometric piping drawing is created manually. Figure 3.9 shows the piping drawing, with the east BJA on the left and the west BJA on the right. The corresponding bill of material can be found in the appendix A.1

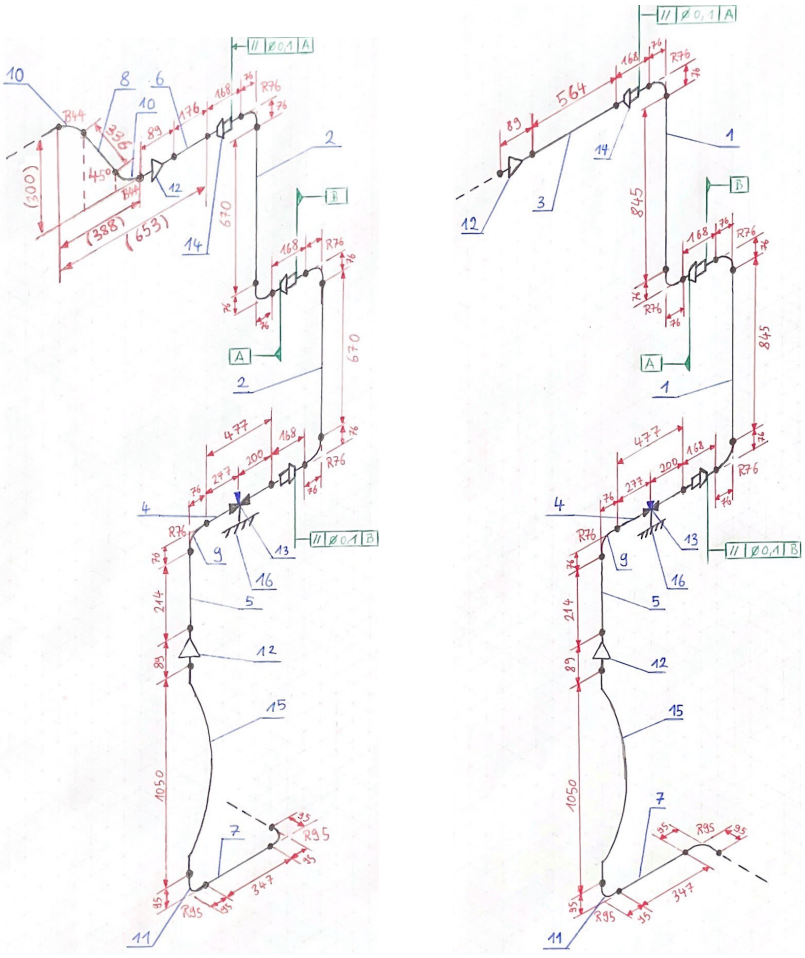

Figure 3.9.: BJA piping dimensions for east side (left) and west side (right)

The length of the pipe sections between the individual ball joints determines the angle between these pipe sections. The connection length between the upper ball joint

and the traverse influences the translational angle. These lengths are determined based on technical drawings of BJAs used in power plants to achieve comparable angles. The two pipe sections between the ball joints should have an inclination of 30 ° in the X-Z plane. The maximum translational angle should be -12 °. As the traverse can only be inclined by -5 °, the BJA is installed with an inclination angle of -7 °.

On the east side, the connection point to the pipe system is in the middle of the traverse frame. Due to the required insulation, the upper ball joint does not fit into the frame. Therefore, the upper ball joint must be positioned lower so that the east assembly is 300 mm lower overall than the west assembly. This must also be considered in the force analysis, as the forces can vary due to different dimensions. The methodology of the test campaigns, the force measurement, and the force analysis carried out are explained in more detail in the following chapter.

4. Methodology

This chapter describes the methodical procedure for the force analysis. First, the calibration of the sensors is explained, which was carried out to ensure reproducible and reliable measured values. This is followed by a description of the commissioning of the test rig and the test campaigns carried out. Finally, the procedure for evaluating the force and torque data obtained using Python is explained.

4.1. Load Cell Calibration

In order to obtain the most accurate and reproducible measurement results possible, it is essential to calibrate the sensors used. This chapter explains the procedure for calibrating the six-axis load cells. It explains how to integrate the calibration protocol provided by the manufacturer. Due to how load cells work, measurement inaccuracies still exist even with a perfect calibration. Therefore, a measurement uncertainty estimation is presented.

The sensors have already been calibrated by the manufacturer and are supplied with a calibration protocol. The calibration protocols are shown in Appendix A.1 and A.2. The load cells are integrated into the SCADA system with the help of this protocol and the equations presented in section 2.3. The equations are programmed into *LabVIEW* with the individual values for zero offset, capacity, output at capacity, and crosstalk for each load cell. Equation 4.1 results from equation 2.5. This equation can be used to determine the measured force of each of the six channels of the load cell. The scaling factor k results from the load cell capacity divided by the voltage output at capacity. This allows the force or moment $F_{dyn,i}$ to be determined for each of the six channels based on the load cell channel voltage output U_i.

$$U_i = k \cdot F_{dyn,i} \;\Leftrightarrow\; F_{dyn,i} = \frac{Capacity}{Output\ at\ Capacity} \cdot U_i \tag{4.1}$$

Equation 4.2 shows an example of the calculation for the force in the x-direction from the eastern load cell.

$$F_{dyn,x} = \frac{3000\,\mathrm{N}}{5.1268\,\mathrm{V}} \cdot U_{Fx} = 585.16\,\mathrm{N/V} \cdot U_{Fx} \tag{4.2}$$

Despite the mechanical decoupling, the crosstalk is removed in the next step because there is still a small influence between the individual channels. Equation 4.3 is used for this, which can be derived from equation 2.6. The crosstalk matrix K is multiplied by the force vector F_{dyn} to obtain the actual applied forces. This matrix multiplication is used to compensate for the mutual influence of the individual channels. The values of the crosstalk matrix are given in %. The result F_{real} reflects the real measured forces.

$$F_{real} = K \cdot F_{dyn} = \begin{bmatrix} 100 & 0.47 & -0.42 & 0.04 & 0.22 & -0.04 \\ 0.53 & 100 & -0.06 & -0.03 & -0.05 & -0.3 \\ -1.81 & -1.54 & 100 & 0.11 & 0.49 & -0.44 \\ -1.49 & -1.05 & 0.7 & 100 & 0.3 & -1.49 \\ -0.46 & 2.29 & 0.98 & -0.21 & 100 & -1.13 \\ 0.84 & -0.33 & -0.39 & -0.38 & 0.54 & 100 \end{bmatrix} \cdot F_{dyn} \tag{4.3}$$

After programming the PLC, initial tests can be carried out to validate the calibration. To do this, the load cells are loaded in the direction of the various axes. A tension belt is fastened around the load cell connector to test the x- and y-axes. This tension belt is tensioned in the direction of an axis using a ratchet, and the force is measured using a cable tension sensor. The z-axis is tested by placing different weights on it. The expected forces are determined by the formula 4.4 where m is the applied mass, and g is the local acceleration of free fall. The calculated values or the values of the rope tension sensor and the values of the load cell are compared. In the case of error-free integration of the load cells, these values match.

$$F_g = m \cdot g \tag{4.4}$$

Both methods are inaccurate and are therefore not used for actual calibration but only to validate successful programming after installation of the calibrated sensors. The manufacturer of the load cells used a calibrated reference load cell for the actual calibration. The torques are no longer explicitly checked at this point. As the correct integration of the two load cells could be confirmed with the described methodology, it can be assumed that the torques are also measured correctly.

A further step implements a button for taring the load cells in the *LabVIEW* program. Taring sets the current measurement to zero so that subsequent values are recorded relative to this reference point. This eliminates preloads or self-weight effects before the actual forces are measured. Taring is carried out after the REPAs to be tested have been installed and before the start of a test campaign.

4.1.1. Measurement Uncertainty Estimation

Various sources of error were analyzed to assess the measurement accuracy of the six-axis load cells used in this study. The relevant measurement uncertainties include zero signal after mounting, hysteresis, creep, non-linearity, and temperature effects, which have already been explained in the fundamentals section. These factors affect the precision of the measured forces and moments and must, therefore, be considered during planning, calibration, and evaluation of measurements to ensure the reliability of the results.

Two different approaches were applied to quantify these measurement uncertainties for the load cells. The values for hysteresis, non-linearity, and temperature effect were taken from the calibration protocols of each load cell. These protocols provide detailed information on the characterization of measurement deviations. In contrast, the values for zero signal after mounting, creep, and zero signal after a temperature cycle were determined directly on the test rig through measurements taken after installation and during the initial test runs. The zero signal after mounting was assessed by observing the initial output signal of the load cells under no load conditions to identify any deviations from the ideal zero value. Creep was determined by monitoring signal drift over time under constant load. The zero signal was evaluated after a full temperature cycle to assess the stability of the sensor signal after exposure to temperature variations.

Table 4.1 summarizes the identified uncertainties, with separate values presented for the East and West load cells. This overview shows that the measurement uncertainties of the two load cells vary slightly, which must be taken into account when interpreting the results. In particular, temperature effects play a crucial role, as they can influence the measurements repeatability and stability. Therefore, regular monitoring of zero signals is essential to ensure the highest possible measurement accuracy.

Table 4.1.: M4347K5 load cell measurement uncertainty

Uncertainty	Approach		Value east	Value west	Estimated impact
Zero signal when mounted S_{F0}	measured		1 N	0.5 N	neglected
Relative hysteresis error μ	<0.1 % FS	<0.2 % FS	<6 N	<12 N	moderate
Relative creep 30 min d_{cr}	measured		<58.3 N	<25.8 N	moderate
Non-linearity error d_{lin}	<0.1 % FS	<0.15 % FS	<6 N	<9 N	moderate
Temperature Effect TK_0, TK_C	<3 %		(±)0 to 180 N		major

FS: of full scale, being in Z axis 6 kN

An uncertainty analysis has already been carried out for the load cell K6D175 using a similar procedure [41]. The exact values of this analysis can be found in the table A.2 in the appendix. The uncertainty values in this table were determined for a temperature of 50 °C. The temperature effect has the most significant impact on the uncertainties of the K6D175 load cell. Accordingly, a deviation due to temperature changes of TK_0 from 580 N and of TK_C from 41 N is possible. This corresponds to an uncertainty approximately 3.5 times as large as the M4347K5 load cell. This is mainly due to the large capacity and the inaccuracies dependent on this full scale, which is why it makes sense to replace these load cells.

4.2. Setup and Execution of Test Campaigns

This subsection describes the test series carried out on the REPA test rig. First, an overview of the typical motion sequence of the test rig's traverse is provided. Furthermore, the two test campaigns performed with the RFHA and BJA are explained. This includes details on the number of executed cycles, the motion sequences, and the operating conditions applied for temperature and pressure.

Figure 4.1 illustrates the typical motion sequence of the REPA test rig. The rotation angle is represented in green, while the translation angle is shown in purple. The figure depicts three cycles, each lasting approximately 150 s. At the beginning of a cycle, the traverse is positioned in the stow position α_{stow}. During each cycle, the traverse moves to the end position α_s and then returns to the stow position. Except for brief stops at the stow and end positions, the traverse moves at an approximately constant speed.

The motion from the stow position to the end position simulates the solar tracking process and, consequently, the movement of the REPA during daytime operation. In

the first half of the cycle, the translational angle remains constant at α_{hot} representing the hot state, where the REPAs experience their maximum translational deflection. In the second half of the cycle, the traverse returns from the end position to the stow position, simulating nighttime conditions in an actual PTC. During the night, the HTF cools down, leading to a reduction in the translational angle. To replicate this effect, the traverse moves continuously to the cold position α_{cold} at a controlled speed. At the beginning of a new cycle, the traverse rapidly returns to the hot position, mimicking the morning reheating process in a solar PTC power plant.

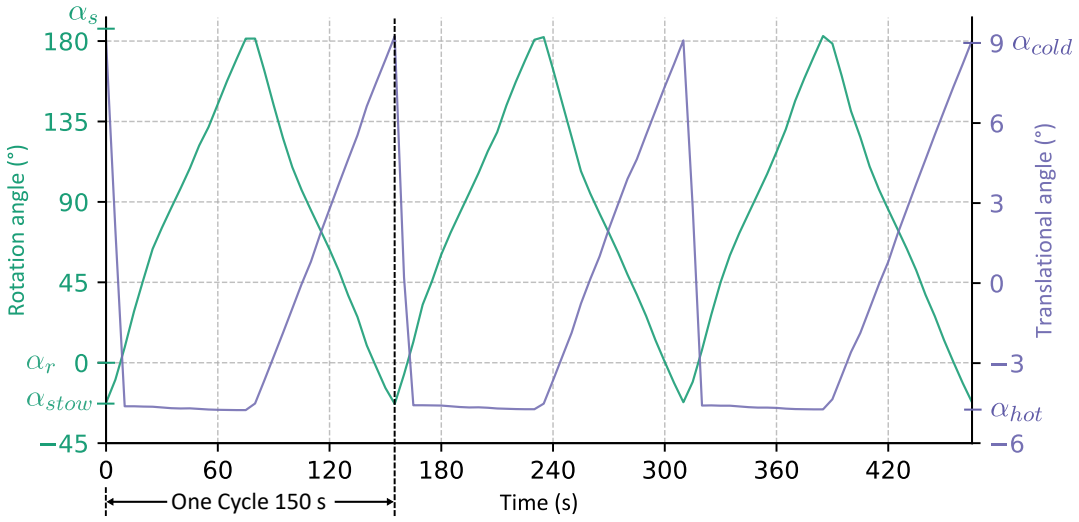

Figure 4.1.: Rotational and translational angle during the cycles

4.2.1. Rotary Flex Hose Assembly Test Campaign

A series of tests with 10,000 cycles had already been carried out in the previous year without any significant abnormalities being detected. Based on these results, further tests were initiated to stress the RFHA components until they reached the end of their service life. For this purpose, around 10,000 cycles were completed in June and a further 4,000 cycles in October 2024. Table 4.2 shows an overview of these test campaigns.

Initially, a rotational movement of -23 ° to 186 ° was set. After the first unplanned standstill after 5545 cycles, the upper limit value was reduced to 183 °. The translational movement remained constant over the entire test campaign. A translation of -5 ° was set for the hot operating state, while 9 ° was selected for the cold state, re-

sulting in a total translational movement of 430 mm. An HTF temperature of 393 °C and an HTF pressure of 34 bar was set for the entire test campaign.

During the test campaign in June, there were several interruptions due to technical problems on the test bench. On June 11, the south inductive sensor was triggered because of a rotational movement problem, and on June 29, magnetic head sensor issues led to rotational movement errors. As maintenance work on the test bench can only be carried out when switched off, these defects led to delays. In particular, the necessary cooling and subsequent reheating of the HTF took about a day in each case.

On July 3, a total cycle count of 20,000 was reached, leading to a temporary interruption of the test campaign. The second testing phase commenced on October 3 to further stress the RFHA components until critical failure. From the beginning of the October test campaign, brief occurrences of smoke formation were repeatedly observed at the swivel joints, ultimately resulting in a shutdown after cycle 24154. Following a total of 24240 cycles, a critical leak occurred, leading to the termination of the test campaign.

Table 4.2.: Procedure for the 2024 RFHA test campaign

Date	Cycle	Rotational movement	Translational movement	HTF-T	HTF-p	Description
2024-06-02	10000	-23 ° to 186 °	-5 ° to 9 ° 430 mm	393 °C	34 bar	Start-up June test campaign
2024-06-11	15545					Shutdown: Inductive Sensor triggered because of rot. movement problem
2024-06-23	15769	-23 ° to 183 °				Restart
2024-06-29	19244					Shutdown: Magnetic head sensor issue leads to rot. movement error
2024-06-30	19279					Restart
2024-07-03	20773					Shutdown: 20.000 cycles at operating conditions reached
2024-10-03	20773					Start-up October test campaign
2024-10-08	24154					Shutdown because of smoke development and first minor leaks
2024-10-10	24240					Leakage during start-up

4.2.2. Ball Joint Assembly Test Campaign

The BJA test campaign also aims to subject the BJAs to operational loads over a complete service life to analyze aging processes and associated mechanical stresses. This study examines the test series that commenced in April 2025. By the time of the first interruption, 2,700 cycles had been completed, corresponding to an equivalent

operating duration of approximately seven years.

Similar to the RFHA test campaign, a temperature of 393 °C and a pressure of 34 bar were defined as test parameters. However, due to the modified dimensions of the REPAs, the motion angles were adjusted. The rotational movement ranges from 0 ° to 180 °, while the translational movement spans from -5 ° to 8 °, corresponding to a linear displacement of approximately 400 mm. As the angular velocity remains the same as in the previous campaign, the cycle time is reduced from 150 s to 130 s.

After approximately 2,700 cycles, the test rig was shut down due to a nationwide power outage. Further restarts and tests to cover the full-service life of the BJAs are planned or ongoing but are not analyzed within the scope of this work.

4.3. Data Analysis with Python

This section provides an overview of the procedure for data analysis with Python. First, it explains why Python was chosen as the tool for data analysis in this work and what advantages this programming language offers. In addition, it explains the libraries used and the procedure for the force analysis.

The constantly growing volumes of data in science and technology require powerful tools for efficient processing and analysis. Python has established itself as a programming language for data analysis. The platform-independent open-source software offers a simple syntax and a wide selection of specialized libraries. This software is further developed by the users themselves, resulting in extensive documentation and support resources being available. This has contributed to Python being established as the standard for data-driven applications in many companies and research institutions. [46]

A major advantage of Python is its comprehensive collection of specialized libraries. These enable efficient numerical calculations, data processing, and visualization. For this reason, Python was chosen as the tool for analyzing the force data in this thesis. The following subsection provides a detailed overview of the libraries used in this thesis and their applications.

4.3.1. Utilized Python Libraries

Four Python libraries are mainly used to process, visualize, and analyze the data collected in the REPA test rig. These are pandas, SciPy, matplotlib, and scikit-learn. This subsection introduces each library and describes how they are used for force analysis.

Figure 4.2 shows an overview of the data collection and force analysis steps. In the REPA test rig, the SCADA system and various sensors are used to collect data for forces, torques, temperature, pressure, and rotational and translational angular position. A data point is measured for all values every 5 s and saved in a CSV file. By recording every 5 s, 30 data points are available per cycle. In this way, one CSV file is generated per day. These files are imported into Python for processing at the end of a test campaign.

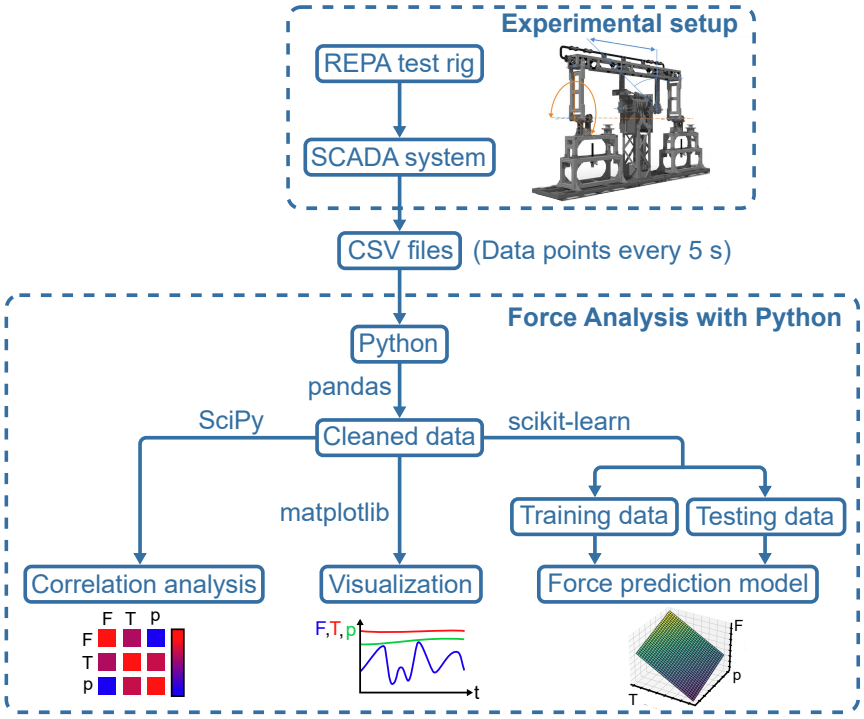

Figure 4.2.: Overview of the steps for the force analysis with Python

The first step is to clean the imported data and prepare it for all subsequent steps. To do this, the data is loaded into a `DataFrame` of the pandas program library. Pandas is a Python library for analyzing and processing tabular data. It combines the efficient data processing of NumPy with the flexible functions of spreadsheets and databases.

The central object is the `DataFrame`, a table with labeled rows and columns for structured data storage and processing. Among other things, pandas enables the filtering, transformation, and aggregation of data as well as the processing of time series and missing values [47]. This allows the REPA test data to be cleaned, missing measured values to be replaced by interpolation, and some features to be added. A column for the cycle mode and a cycle counter are added as features. The cycle mode variable can distinguish between three different operating modes of the test rig. Firstly, the standstill mode, when both the rotation angle and the translation angle remain unchanged, and therefore, no cycles are performed. This is the case, for example, during the heat-up or cool-down of the test rig. Secondly, the cycle mode in which cycles are run with pressures and temperatures below the real operating conditions, and thirdly, the cycle mode for cycles with real operating conditions of around 393 °C and 34 bar. The completed cycles are counted with the cycle counter feature. This means that only certain cycles can be considered in the further force analysis. The `DataFrame` generated in this way for each test series is then used for the actual force analysis. A correlation analysis is carried out, various cycles are visualized, and a force prediction model is created.

SciPy is a scientific Python library that enables numerical computations in various fields such as optimization, integration, linear algebra, and statistics [47]. In this work, the module `scipy.stats` is used, which provides tools for statistical analysis, including probability distributions, statistical tests, and descriptive statistics. The Person method is used to perform the correlation analysis of the different variables measured in the test campaigns.

Matplotlib is the most commonly used Python library for creating two-dimensional diagrams and data visualizations [47]. The library enables the creation of customizable diagrams. In this work, Matplotlib was used to visualize the experimental measurement data.

Scikit-learn is a Python library for machine learning that provides a variety of algorithms for classification, regression, clustering, and model evaluation [47]. This work used scikit-learn to train a random forest regressor model and a linear regression model. For this purpose, the data was split into training and test data to optimize the models and evaluate their accuracy. The trained models can be used to predict expected force amplitudes for different combinations of temperature and pressure in

order to compare test cycles performed.

4.3.2. Procedure for Force Analysis

As described in the previous subsection, the procedure for force analysis with Python can be divided into three methods. To gain a deeper understanding of the loads acting on the REPAs throughout their operational period and to analyze specific events within a movement cycle, a correlation analysis is carried out, the data is visualized at defined points in time, and a model for force prediction is trained.

In the first step, a correlation analysis is carried out. This provides an overview of the relationships between the individual variables and enables an analysis of the influences of temperature, pressure, and rotational and translational movements on the forces and torques.

In the second step, the forces and moments are visualized over various cycles. The graphical representation of the cycles makes it possible to analyze the development of the forces and moments over the entire test duration and, thus, over the life cycle of the REPAs. Figure 4.3 provides an overview of the RFHA test campaign. It shows the forces in the z-direction of both RFHAs, as well as the HTF temperature and the HTF pressure. In addition to the development of the forces and moments over the entire test duration, certain critical points in time are considered, as shown in the Figure. Of particular interest here are times at which shutdowns occurred due to smoke development or leaks. These points in time are recorded during the test campaigns and documented in the REPA logbook. By visualizing the data at these points, the forces during a failure can be analyzed and compared with data from fault-free cycles. In particular, the development of the forces and moments in the cycles before the failure is examined in detail. If there are recognizable changes in the data at these points, these could be used as indications for possible condition monitoring and the implementation of predictive maintenance.

In order to ensure better comparability of the analyzed cycles, a machine learning model for force prediction is developed as part of the force analysis. Temperature and pressure are input variables, while the expected force amplitude is calculated as the output. For this purpose, the data is segmented into individual cycles and divided into training and test data sets. The model is then trained, creating a separate

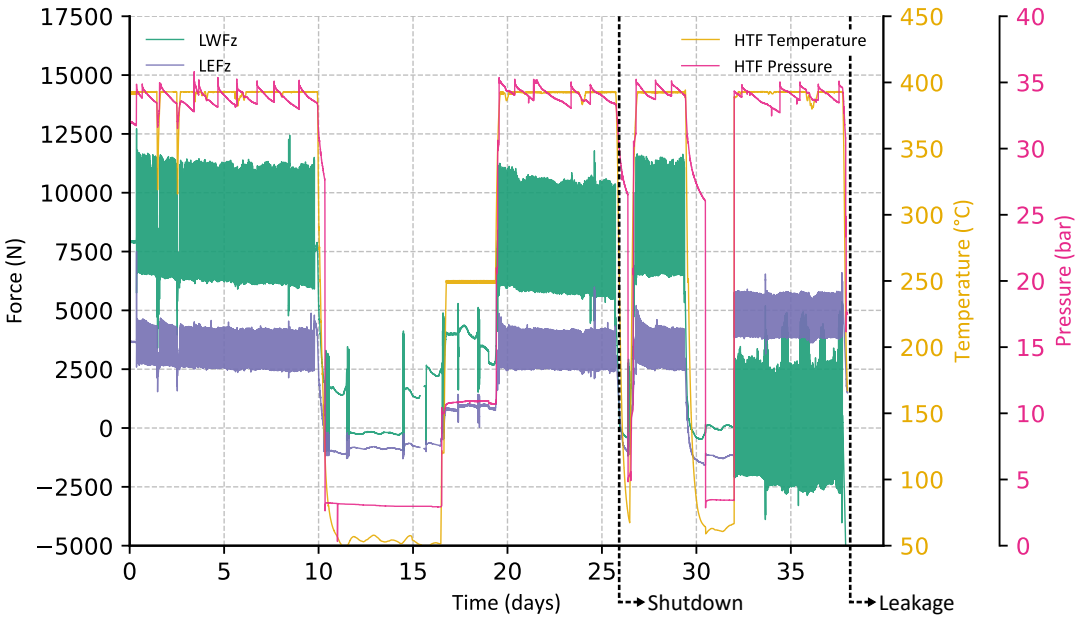

Figure 4.3.: Overview of the force, temperature and pressure values of the 2024 RFHA test campaign

model for each REPA. With the help of these models, special cycles that take place at temperatures and pressures below the real operating parameters and for which no comparison values exist can be compared with the values generated by the model. This allows statements about the measured forces and torques at specific points in time, such as leakage.

Figure 4.4 shows an overview of the first test series of the BJA test campaign, analogous to the representation of the RFHA test campaign. Since only the first 2,700 cycles of the BJA test campaign are available for analysis and no irregularities, such as smoke development or leakages, occurred during this period, the REPA force analysis primarily focuses on the RFHA test campaign. However, the first two steps of the force analysis are also conducted for the BJA test campaign. In addition, selected relationships and differences in the occurring forces and torques between the two REPA types are presented. The following chapter presents the results of the force analysis, including the correlation analysis and the trained force prediction models.

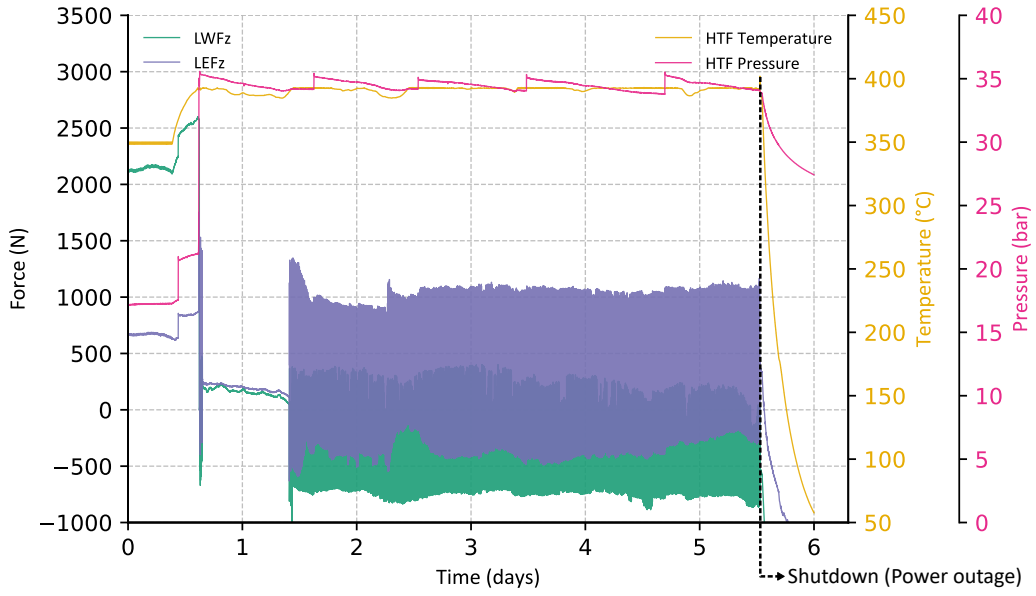

Figure 4.4.: Overview of the force, temperature and pressure values of the 2025 BJA test campaign

5. Results and Discussion

Mechanical loads on the REPAs are a key factor in their long-term functionality. In order to gain a deeper understanding of the forces and moments that occur during operation, a RFHA and a BJA test campaign were carried out. The results of these measurements are presented and analyzed in this chapter. For this purpose, the recorded forces and torques are examined using the methods described in the previous chapter.

As the RFHA test campaign has been completed, these results will be considered primarily. The initial results of the BJA test campaign will be presented in parallel. This allows the results of both test campaigns to be compared in order to identify differences and similarities in the mechanical stress of the REPAs examined. A special focus is placed on the measured values at the time of leakage to analyze the mechanical loads in this phase. The force analysis aims to identify characteristic load patterns and systematically evaluate the mechanical stress on the REPAs.

5.1. Results of the REPA test campaigns

This section presents the results of both REPA test campaigns with a focus on the RFHAs. First, a comparison is made with measured values from a real PTC with an RFHA system to assess the validity of the data recorded in the test rig. The correlation analysis is then presented to analyze the relationships between the parameters investigated and their mutual influence. The cyclic forces and moments of the two REPAs are then presented. A special focus is placed on the load cycles before and after the leakage of the west swivel in the RFHA test campaign. A comparison is made between the west and east sides, and the results are compared with the predictions of the force prediction model.

Figure 5.1 compares the torque values measured on the REPA test rig with those of a real PTC system. The comparison is based on the measured values obtained

by López-Martín et al. [48] on a URSSATrough Semi-SCA with RFHA. The torque values around the rotation axis were compared with those around the y-axis, which is the rotation axis of the test rig. For this purpose, the values of LWMy at the West REPA from the RFHA test campaign are used.

The left-hand side of the figure shows the torque curve over time. Due to differing cycle times in the conducted tests, the curves were scaled to display two complete tracking cycles. Apparent similarities between the values from the test rig (shown in green) and the PTC system (shown in orange) can be observed. In the first half of the cycle, only positive values are present, showing a decreasing trend. In the second half of the cycle, negative values appear, initially increasing and dropping shortly before the start of the next cycle. While some fluctuations are visible in the REPA test rig values, the general trend closely resembles that of the PTC system, with the REPA test rig showing slightly higher torque amplitudes and, thus, higher loads. On the right side of the figure, the torque curve is shown as a function of the rotational angle. The same patterns as described earlier are observed. It can be concluded that the REPA test rig, despite shorter cycle times and higher rotation speeds, creates realistic conditions for the loading of the REPAs.

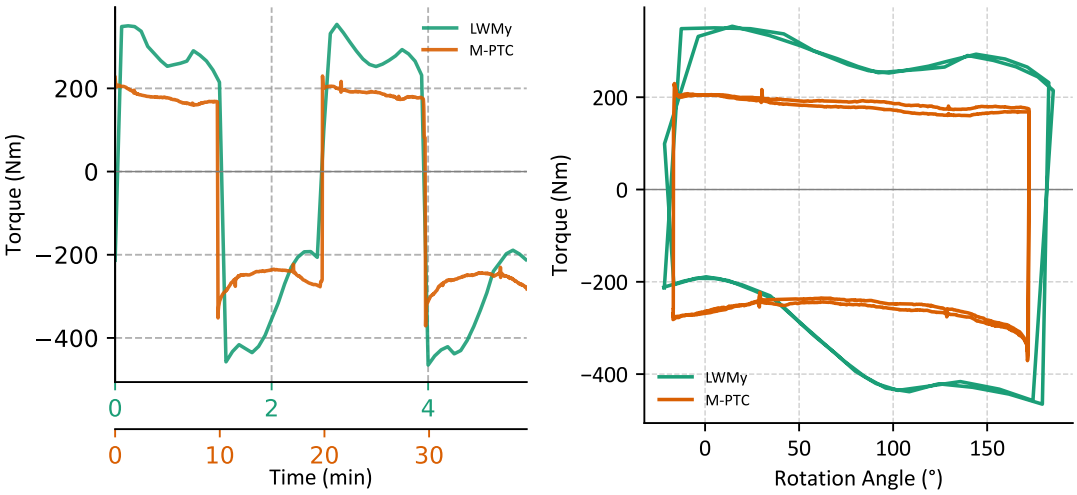

Figure 5.1.: Comparison of the torque measurement data of the REPA test rig and a PTC, measurement data on the PTC from López-Martín et al. [48]

5.1.1. Correlation Analysis

In the first step of the force analysis, a correlation analysis is conducted to determine the influence of the operating parameters of the test rig on the measured force values. Using the Pearson method, a correlation matrix is generated. The selected variables include the forces of the two REPAs on the west and east sides, the rotational position, the translational position, the process temperature, the process pressure, and the load cell temperature.

Figure 5.2 shows the resulting heatmap of the correlation matrix for the RFHA test campaign. The Pearson correlation quantifies the linear relationship between two variables. A value of 1, depicted in orange, indicates a complete positive correlation, whereas a value of -1, shown in green, signifies a complete negative correlation. A value of 0 suggests no correlation, with intermediate values representing weaker but still present correlations. Since all p-values are below $6.16 \cdot 10^{-12}$, which is significantly lower than 0.05, it can be assumed that all observed correlations are statistically significant.

A pronounced influence of the process variables process temperature, process pressure, and load cell temperature on the forces of both REPAs, on both the west and east sides, is evident. The process temperature exhibits the highest positive influence, with a correlation of 0.92 on the west and 0.97 on the east side. The load cell temperature follows with correlation values of 0.89 on the west and 0.95 on the east side. Process pressure shows a correlation of 0.74 on the west side and 0.77 on the east side with the force values. Overall, this indicates that higher temperatures and pressures correlate with higher forces. Additionally, these three variables strongly influence each other. The correlation between process temperature and load cell temperature is 0.97, which can be attributed to the fact that the process temperature and ambient temperature significantly influence the load cell temperature. Similarly, a high positive correlation of 0.78 exists between process temperature and pressure. To account for these interdependencies, partial correlations between the five process variables and the forces of the two REPAs are calculated. Figure 5.3 shows these partial correlations for both test campaigns.

The rotational and translational positions moderately influence the forces in the RFHA test campaign, which is expected since movements lead to force variations.

Figure 5.2.: Heatmap of the correlation matrix from the RFHA test campaign

Notably, an opposing effect is observed between the east and west sides. The correlation between rotational position and the forces is -0.15 on the west side and 0.22 on the east side. An inverse trend is observed for the translational position, with a correlation of 0.48 on the west side and -0.12 on the east side. These discrepancies between the two sides are also evident in the force cycle diagrams in the following subsection 5.1.2. Possible reasons for this could include minor structural differences between the two sides of the test rig, varying aging states of the RFHAs, differing load cell calibrations, or deviations in the installation of the load cells, such as varying bolt tightening forces during mounting. Furthermore, process temperature is shown to have the most significant influence on the forces in the RFHA test, with a partial correlation of 0.55 on the west side and 0.7 on the east side. Compared to the Pearson

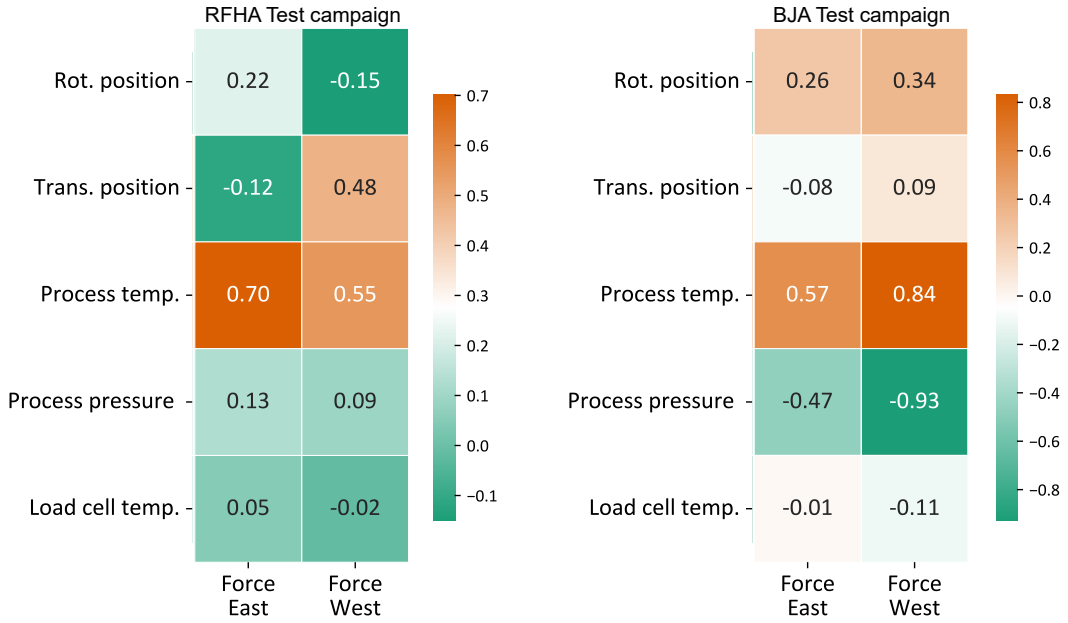

Figure 5.3.: Partial correlation between force values and operating parameters for RFHA (left) and BJA (right) test campaign

correlation matrix results, the influence of process pressure and load cell temperature is considerably lower. Process pressure exhibits a weak positive correlation with the forces, with values of 0.09 on the west and 0.13 on the east side. The load cell temperature has nearly no impact, with correlation values of -0.02 on the west and 0.05 on the east side.

In summary, temperature has a particularly significant effect on the forces that occur in the RFHA test. As temperature increases, the material's thermal expansion leads to internal stresses and structural stiffening. This results in increased forces, leading to higher loads on the RFHAs.

In contrast, the BJA test campaign shows similarities to the RFHA results and clear differences. As observed in the RFHA test, there is a strong positive correlation between process temperature and the forces. The correlation is 0.57 on the east and 0.84 on the west sides. A key difference is found in the influence of process pressure. While pressure had a weak effect in the RFHA test, the BJA test shows a strong negative correlation between pressure and forces. This does not necessarily mean that higher pressure always leads to smaller forces. Instead, it suggests that forces may shift further into the negative range under higher pressure. As a result, the total

force amplitude can increase.

Looking at the absolute values, it is clear that pressure plays an important role in the BJA test. This strong influence is reasonable because pressure, like temperature, can lead to internal stresses in the structure. These stresses increase the measured forces. The BJA configuration is more sensitive to such pressure effects than the RFHA setup.

5.1.2. Forces during cycling

This subsection presents various diagrams of the forces that occurred in the test campaigns. An offset value is calculated for each cycle to minimize inaccuracies in the force measurement caused by the long measurement period and to ensure comparability of the individual cycles performed. Using interpolation, the value in the 90 ° position is determined in the movement from the stow to the end position and used as the offset for the entire cycle. The values of the offset and a more detailed analysis are presented in Figure 5.10. Due to the offset, the value at 90 ° is always 0 N. All other values are to be seen in relation to this value and do not correspond to the absolute values measured.

Figure 5.4 provides an overview of the forces measured at both REPAs during the two test campaigns. The results of the RFHA are shown on the left-hand side, and those of the BJA test campaign on the right-hand side. For the RFHA test campaign, the arrows represent the average forces in the respective directions from cycle 10,000 to cycle 24,154. Only cycles conducted under real operating conditions, at an HTF temperature of 393 °C and an HTF pressure of 34 bar, are considered. The lines above and below the arrows indicate the measurement uncertainties, calculated based on the values from Table 4.1 and A.2.

In the left diagram, the arrows on the left depict the forces of the East RFHA, while the arrows on the right represent the forces of the West RFHA. For the East RFHA, the values in the x-direction range from -761 N to 345 N, corresponding to an amplitude of approximately 1106 N. In the y-direction, the forces range from -1294 N to 10 N, resulting in an amplitude of about 1304 N. The forces recorded in the z-direction vary between -939 N and 746 N, with an amplitude of approximately 1685 N. At the West RFHA, the forces in the x-direction range from -14 N to 2663 N, leading to

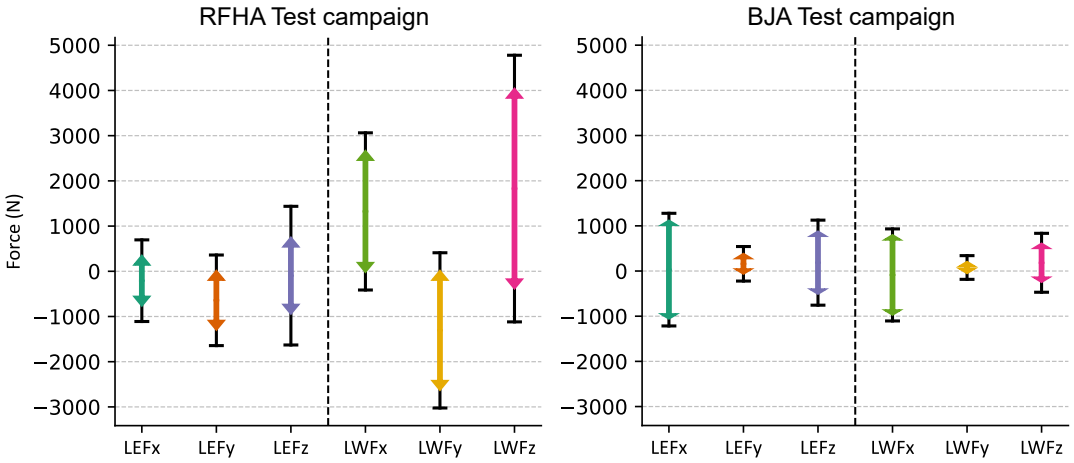

Figure 5.4.: Comparison of the average force values of the RFHA (left) and the BJA (right) test campaign

an amplitude of about 2677 N. In the y-direction, the measured forces range from -2624 N to 10 N, corresponding to an amplitude of approximately 2634 N. The values in the z-direction vary between -379 N and 4039 N, resulting in the largest amplitude of around 4418 N.

The distribution of forces shows a comparable structure in terms of arrow positioning and amplitudes. The forces at the West RFHA represent a scaled version of those at the East RFHA. In the x- and y-directions, the forces at the West RFHA are approximately twice as high as those at the East RFHA, while in the z-direction, they are about two and a half times as high. Negative values predominate in the y-direction, while the greatest forces are measured in the z-direction. Due to this pronounced force distribution in the z-direction, a more precise analysis of the forces in this direction follows for the RFHA test campaign.

Figure 5.4 also shows an overview of the forces measured during the first 2700 cycles of the BJA test campaign. In contrast to the RFHA test campaign, the forces on both sides show a comparable distribution. On the east side, the force values are higher overall, with the highest values in the x-direction. Here, the amplitude is 2171 N on the east side and 1763 N on the west side. The slightly different BJA dimensions can explain the minimal differences, with the higher forces occurring on the BJA with shorter connecting pipes. The measured forces are, therefore, of a similar order of magnitude to the values recorded on the east side during the RFHA test campaign.

This observation supports the assumption formulated in the correlation analysis of the RFHA test campaign that an error in the force measurement could have caused the observed differences between the two sides.

Figure 5.5 shows the forces in the z-direction on both RFHAs as a function of the rotation angle. Only the most pronounced forces in the z-direction are shown here. The diagrams of the other two directions have similar characteristics and are shown in the appendix A.3 and A.4. The forces of the cycles on the east side are shown on the left, and those of the west side are on the right. Each curve represents one cycle, starting from the stow position at -23 ° to the end position at 183 ° or 186 ° and back to the stow position. For a better overview, one cycle is shown for every 2,500 cycles. The arrows mark the start of the movement from the stow position at the time t_{stow} and the start of the return movement from the end position at the time t_{end}. Due to the offset applied, the force at 90 ° is always 0 N.

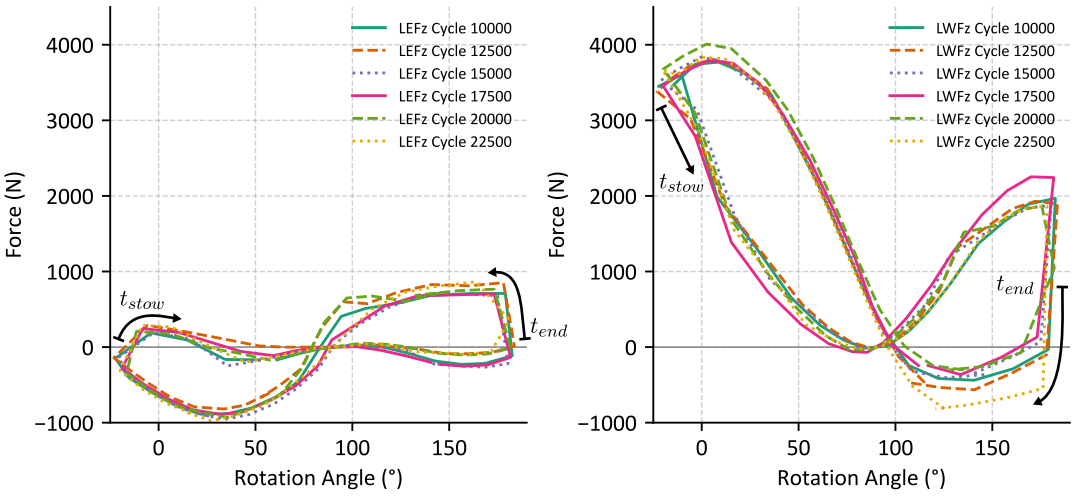

Figure 5.5.: Force values in z-direction as a function of the rotation angle for the RFHA test campaign

For both the East and West RFHA, the shape of the curve remains largely constant in the range from cycle 10,000 to cycle 22,500. Minor deviations are recognizable, but there is no continuous trend of increasing or decreasing loads as a function of the number of cycles, and thus, increasing service lifetime can be determined. This means that both the force amplitude and the type of loading remain constant over the observed period. In contrast, the behavior of the BJA differs. Figure 5.6 shows a corresponding diagram. Here, the most pronounced forces in the BJA test campaign

are shown in the x-direction every 500 cycles. The time intervals between the individual curves are significantly smaller than in Figure 5.5, yet noticeable differences in the force profiles are still evident. An analysis of the forces in the other directions reveals no clear correlation between the number of cycles and the force characteristics. The corresponding diagrams of the y- and z-directions are included in Appendix A.5 and A.6. It is noticeable that the forces at the time of cycle 0 show a minimum in the x-direction, while a maximum occurs in the other directions. This behavior is due to the design and installation method of the BJAs. In the first cycles after the initial assembly, the system is still very dynamic due to the many degrees of freedom, which means that the forces in this phase still exhibit large fluctuations. In the further course of the BJA test campaign, an increased variation in the force amplitude can be observed. In some cases, the forces change by more than 200 N between consecutive cycles.

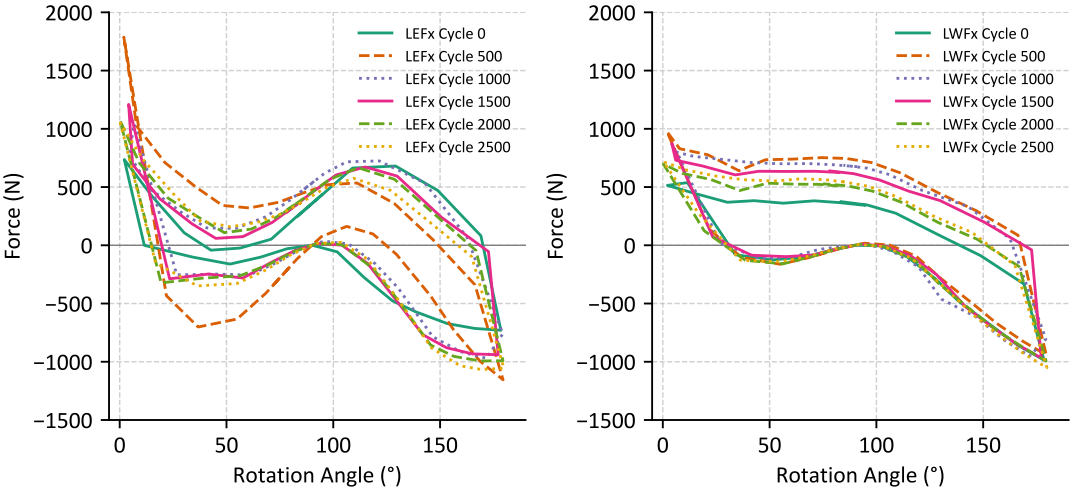

Figure 5.6.: Force values in x-direction as a function of the rotation angle for the BJA test campaign

In accordance with the correlation analysis regarding the relationship between angular position and force, significant differences between the two sides of the RFHA test campaign can be seen in Figure 5.5. On the east side, the force remains nearly constant during the movement from the stow to the end position. The maximum occurs at approximately 180 °, just before the return movement to the stow position starts. The force then decreases, reaching a minimum at around 30 ° before returning to the initial position. However, the maxima and minima are arranged oppositely on the west side. During the movement from the stow to the end position, the force decreases until reaching 90° and then increases again until the end position is reached. At the

beginning of the return movement to the stow position, the force drops abruptly, reaching a minimum at around 130 °. It then rises, with the maximum occurring at approximately 0 °, just before the stow position. Consequently, the force distributions on the east and west sides are inversely related.

These differences occur despite the identical orientation and arrangement of all REPA components. Potential causes, previously mentioned in the correlation analysis, include minor structural variations between the two sides of the test rig, differing aging states of the RFHAs, variations in load cell calibration, or deviations in the installation of the load cells. To analyze these differences more accurately, it is helpful to visualize the dependencies of the forces on both sides. Figures 5.7 and 5.8 show the forces on all three axes about one another for one cycle under standard operating conditions. The resulting curve is color-coded according to the rotation angle based on the colormap displayed on the right. Each figure shows an isometric, side, and top-down view, with an RFHA model also inserted in the 90 ° position for clarity.

Figure 5.7 illustrates how the forces on the East side change throughout a cycle. A clear difference depending on the displacement from the 90 ° position is evident, particularly in the top-down view. For angles greater than 90 ° (represented by the orange part of the curve), predominantly positive forces in the x-direction are observed. The opposite occurs for angles less than 90 °, with predominantly negative forces in the x-direction. This is expected, as the traverse is deflected either to the right or left of the 90 ° position for angles greater or smaller than 90 °, leading to forces in opposite x-directions from the 90 ° position. The distribution of forces in the y-direction also aligns with expectations. As described earlier, the traverse remains in the -5 ° position during the first part of the cycle. Then, it moves only in the negative y-direction up to 9 °, resulting in many values near 0 N, with the remaining values primarily in the negative range.

In comparison, the forces on the west side, as shown in Figure 5.8, differ significantly in some aspects from those on the east side. The distribution of forces in the y-direction is comparable. However, an opposite behavior is observed in the z-direction, as previously noted in the specific analysis of forces in the z-direction. The maximum occurs around 0 °, in the green region of the curve, whereas on the East side, the minimum occurs shortly after 0 °. The most significant difference is seen in the distribution of forces in the x-direction. Here, instead of forces in both positive

and negative directions as expected, only positive values are observed from the 90 ° position onward.

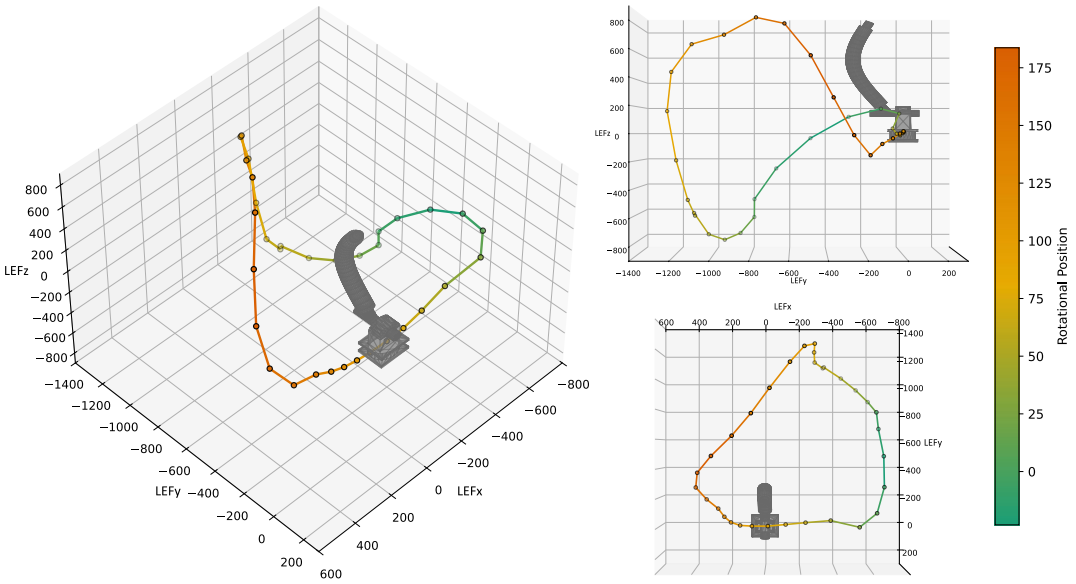

Figure 5.7.: Standard cycle forces on the East RFHA in isometric view, side view, and top-down view, all axes represent force in (N)

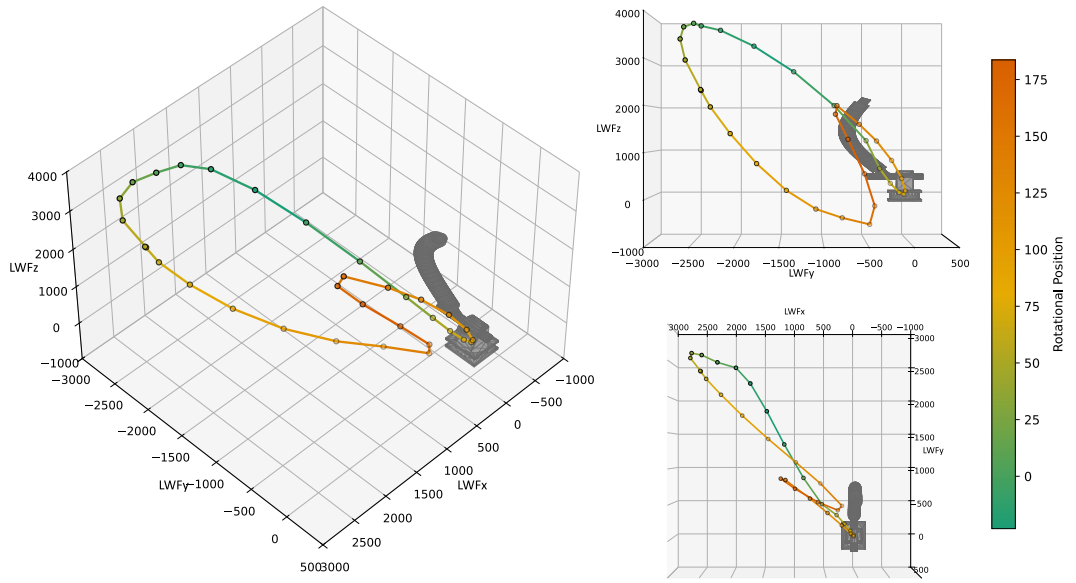

Figure 5.8.: Standard cycle forces on the West RFHA in ismoetric view, side view, and top-down view, all axes represent force in (N)

Given the fundamental differences between the two sides, structural differences in the

test rig setup or varying aging states of the RFHAs are unlikely causes. The incorrect calibration of the load cells, of one or more channels of these sensors, and deviations in the installation of the load cells could be the cause. However, this cannot be definitively verified due to the integration of new sensors and the reprogramming of the PLC that took place before the RFHA test campaign force analysis. Therefore, the exact reason for the differences between the two sides cannot be determined with certainty based on the available data.

Figure 5.9 shows the forces measured by the newly integrated load cells for a typical cycle of both BJAs. In contrast to the data obtained during the RFHA test campaign, apparent similarities between the two BJAs are evident here. The only notable deviation occurs around 45 ° during the return motion from the end position at 180 ° toward the stow or start position at 0 °. On the East side, an additional loop is observed in which the forces in both the x- and y-directions briefly decrease and then increase again, while the forces on the West side remain essentially constant in this range. These deviations are likely attributable to minor design differences between the two BJAs. Aside from these minor discrepancies, the force curves exhibit the expected characteristics. Starting from the 90 ° position, the forces in the x-direction predominantly assume negative values toward the end position at 180 ° and positive values toward the stow or start position at 0 °. Moreover, it is observed that forces in the z-direction are generally positive around 180 ° and predominantly negative around 0 °. As shown in the summary of the BJA test campaign, the forces in the y-direction are relatively small, indicating that the BJA effectively compensates translational motions without generating significant forces along the translation axis.

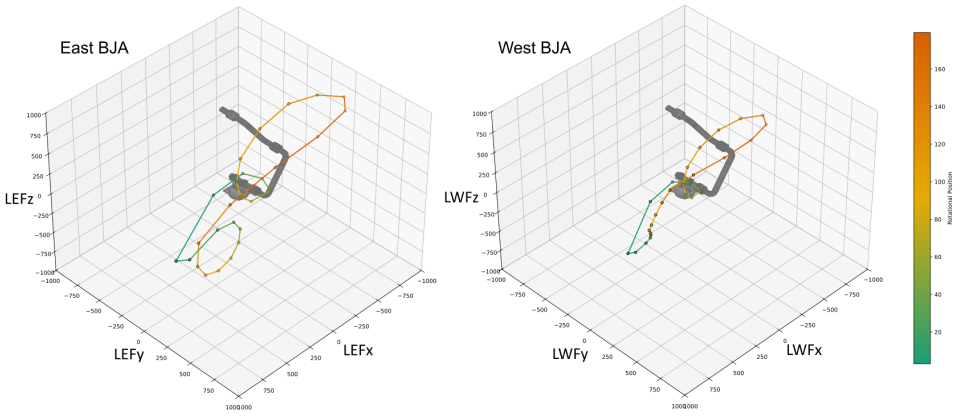

Figure 5.9.: Standard cycle forces for the BJA test campaign in ismoetric view for east (left) and west (right) side, all axes represent force in (N)

Figure 5.10 shows the previously described offset used in the force analysis for the RFHA test campaign. These curves represent the force value at 90 ° in the tracking movement from the stow position to the end position for each cycle. The left side of the figure displays the offset of the three axes of the East load cell, while the right side shows the offset of the three axes of the West load cell. Offset values for the BJA test campaign can be found in the Appendix A.7.

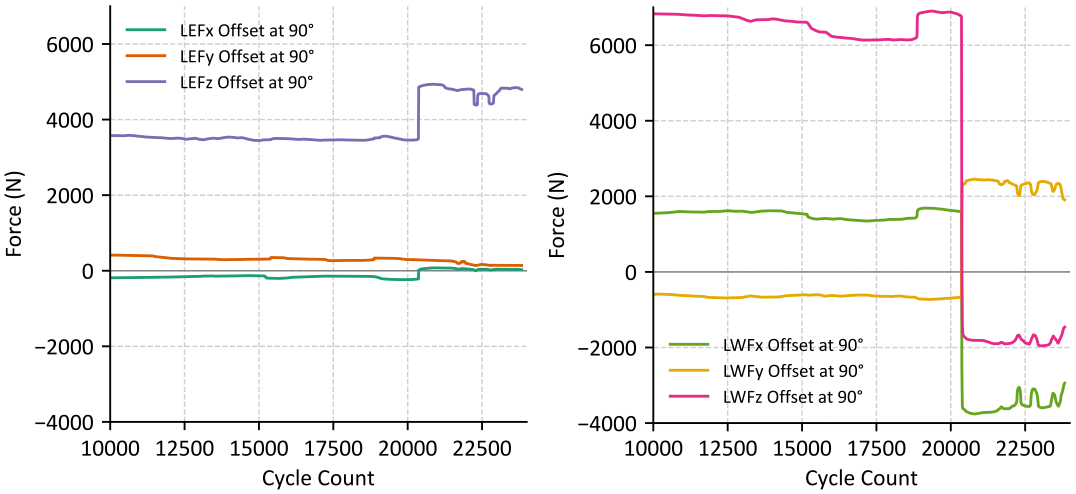

Figure 5.10.: Force offset values for the cycles performed in the RFHA test campaign

The offset values on the East side remain nearly constant for all three axes during the first 10,000 cycles of the test series. A slight downward trend is observable, which is more pronounced on the West side. In particular, the offset values of the z-axis decrease by approximately 700 N. This value exceeds the expected measurement inaccuracies. While the force amplitude remains constant, as observed in the analysis of individual cycles, the absolute force values decrease overall. The jumps in offset values at cycles 19,244, and 20,733 can be attributed to shutdowns of the test rig at those times. During these shutdowns, the load cells were tared, which led to significant differences in force values, especially after the shutdown at 20,733 cycles and the subsequent three-month pause before restarting. These differences are the reason for using the offset approach in force analysis, as it ensures comparability between different test phases. The peaks at cycles 22,300, 22,800, and 23,450 can be traced back to a malfunction of the encoder measuring the translational angle. Erroneous measurement values transmitted to the SCADA system affected the translational movement, leading to variations in the occurring forces. Cycles from these phases were not considered in the analysis, as they are not comparable to cycles conducted

under standard operating conditions.

In summary, under standard operating conditions of 393 °C and 34 bar, a constant force amplitude can be observed. Apart from a slight downward trend in the maximum force values, the load on the RFHAs remains stable over most of their lifetime. Furthermore, significant differences in force values between the two sides are evident, but the exact cause cannot be identified. However, incorrect calibration or differences in the installation of the load cells cannot be ruled out. Therefore, in the next step, the torques will also be analyzed to examine additional comparative parameters between the sides before finally considering the forces and moments at the time of the detected leakage.

5.1.3. Torques during cycling

Analogous to Subsection 5.1.2, which discusses the forces during cycling, this subsection presents the torques. The same offset method with an offset at 90 ° is also used to analyze the torque values. Figure 5.11 provides an overview of the measured torques during the RFHA and the BJA test campaign. The left diagram represents the average torques along the respective axes from cycle 10,000 to cycle 24,154 for the RFHA test campaign. The diagram on the right shows the average torques from cycle 0 to 2700 of the BJA test campaign. As in the previous force analysis, only cycles conducted under actual operating conditions are considered. The lines above and below the arrows indicate the measurement uncertainties, which were determined based on the values from Table 4.1 and A.2.

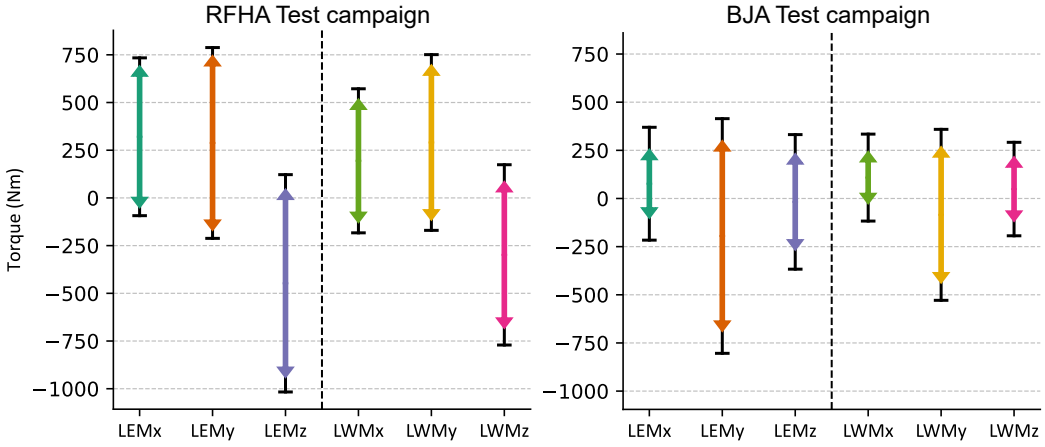

Figure 5.11.: Comparison of the average torque values of the RFHA (left) and the BJA (right) test campaign

For the East RFHA, the torques at the x-axis range from -49 Nm to 690 Nm, resulting in an amplitude of approximately 739 Nm. Around the y-axis, the torques vary from -168 Nm to 774 Nm, corresponding to an amplitude of approximately 912 Nm. The torques recorded at the z-axis range from -939 Nm to 44 Nm, with an amplitude of 983 Nm. For the West RFHA, the torques at the x-axis range from -127 Nm to 516 Nm, leading to an amplitude of about 643 Nm. At the y-axis, the measured torques range from -114 Nm to 695 Nm, corresponding to an amplitude of approximately 809 Nm. The torques at the z-axis vary between -681 Nm and 84 Nm, resulting in an amplitude of around 765 Nm.

In contrast to the measured force values of the RFHA test campaign, the torque values on the east and west sides are very similar. This corresponds to the expectation for the correct calibration of the load cells. The average torque values recorded during the BJA test campaign are also similar for both sides, as seen in Figure 5.11 on the right side. For the BJAs, the highest torques are observed around the y-axis, which corresponds to the rotational axis of the test rig. The amplitude reaches 986 Nm on the East side and 704 Nm on the West side. These values are comparable to the results obtained from the RFHA tests. The torque amplitudes around the x- and z-axes range between 300 Nm and 400 Nm and are, therefore, approximately half the magnitude of those observed in the RFHA campaign.

In the RFHA test campaign, the values on the x and y axes are predominantly in the positive range. This is because the translational movement of the traverse mainly causes the moments around the x-axis. This movement occurs once per cycle, from the hot starting position at -5 °, which also corresponds to the 90 ° offset position, to the cold end position at 9 °, so that the load predominantly acts in one direction. As a result, mainly positive torques occur along the x-axis. The torques around the y-axis exhibit two characteristic values depending on the direction of rotational movement. Since the offset in the tracking motion was set from the stow to the end position, values close to 0 Nm are primarily expected in the forward movement. Nearly constant positive torques occur in the return movement from the end to the stow position. This behavior is also observed in Figure 5.12, which shows the torques around the y-axis of both RFHAs as a function of the rotational angle.

On the left side of the figure, the torques of the cycles on the east side are shown, while those on the west side are displayed on the right. For better clarity, only the

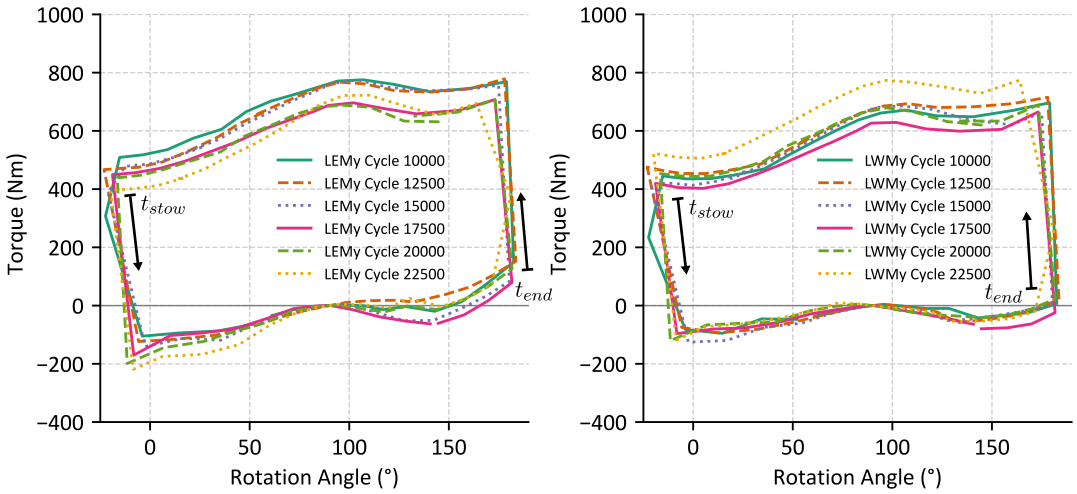

Figure 5.12.: Torque values at the y-axis as a function of the rotation angle for the RFHA test campaign

torques around the z-axis are presented, as the analysis of the diagrams of the other two axes exhibits similar characteristics. These diagrams are in Appendix A.8 and A.9. Analogous to Figure 5.5, each curve represents a cycle from the stow position at -23 ° to the end position at 183 ° or 186 °, and back to the stow position. Every 2,500th cycle is displayed for representation. The arrows indicate the start of the movement from the stow position at time t_{stow} and the start of the return movement from the end position at time t_{end}. Due to the applied offset, the torque values at 90 ° are always 0 Nm. The torque values remain approximately constant in both movement directions, from the stow to the end position and back. At the transition points in the stow and end positions, abrupt changes occur. For both the east and west RFHAs, the shape of the curves and the amplitude of the torques remain essentially constant from cycle 10,000 to cycle 22,500. However, a slight increase in torque values can be observed on the west side in cycle 22,500. This could indicate the first signs of aging, as a leakage was observed on the west side shortly afterward.

Figure 5.13 shows the torque about the y-axis measured during the BJA test campaign, with every 500th cycle shown. The magnitude of the measured torque is comparable to that observed in the RFHA test campaign. The shape of the curve also resembles that shown in Figure 5.12. Due to a reassignment of coordinate axes resulting from the newly integrated load cells used in the BJA test campaign, predominantly negative values were recorded, in contrast to the predominantly positive

values observed in the RFHA test campaign. Torques occurring around the axis of rotation are, therefore, approximately the same for both REPA types. Throughout the 2700 cycles conducted in the BJA test campaign, no irregularities such as leakage or smoke development were observed. Since the measured torque characteristics are similar to those of the forces analyzed in the x-direction, a more detailed examination of the torque data from the BJA campaign is not provided. Additional diagrams for the torques about the x- and z-axes are presented in Figures A.10 and A.11 in the appendix. The offset values applied for generating these diagrams are documented in Appendix A.12.

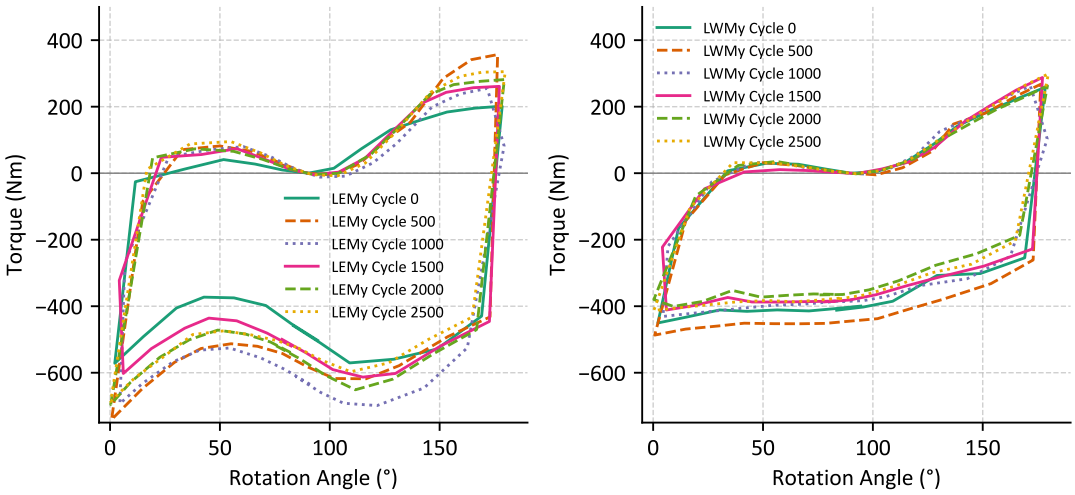

Figure 5.13.: Torque values at the y-axis as a function of the rotation angle for the BJA test campaign

Figure 5.14 shows the 90 ° offset values used in the previous diagrams of the RFHA test campaign. The left side of the figure represents the offsets of the three axes of the eastern load cell, while the right side shows the offsets of the three axes of the western load cell. Similar to the force offsets, discontinuities in the data can be observed at cycles 19,244 and 20,733, which are attributed to various shutdown events and the subsequent recalibration of the sensors. Additionally, peaks are visible around cycle 22,500, likely caused by faulty translational movements. Apart from these variations, the offset remains constant throughout the investigated period. Only the x-axis values exhibit a slight decrease between cycle 10,000 and cycle 18,500, while the y-axis offset on the eastern side increases. Since this value is negative, this implies a slight reduction in the absolute offset value.

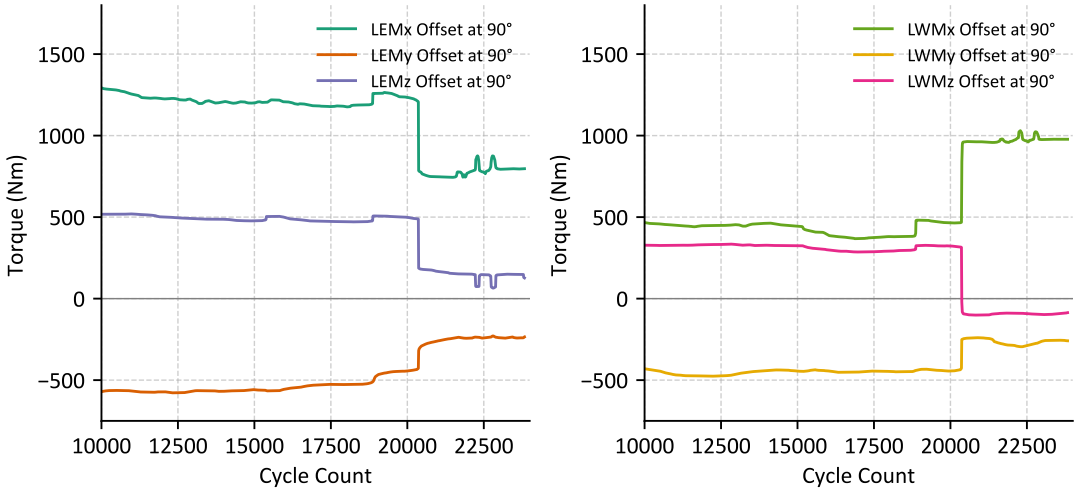

Figure 5.14.: Torque offset values for the cycles performed in the RFHA test campaign

Under standard operating conditions of 393 °C and 34 bar, a slight downward trend in the offset values, and consequently in the maximum torque values, can be observed. The torque amplitude remains constant over most of the operating period, indicating a stable load on the RFHAs. In contrast to the results of the force analysis, both sides exhibit similar torque amplitudes and load patterns. A noticeable increase in values around cycle 22,500 is observed on the western side, which may be an early indicator of the leakage that later occurred on this side. Therefore, the forces and moments at the time of leakage will be analyzed in more detail in the next step.

5.1.4. Forces and Torques during the Failure

After cycle 24,240 during the RFHA test campaign, a leakage occurred at the West RFHA, causing VP-1 oil to leak from the swivel joint. Figure 5.15 shows the oil residue that has formed on the west swivel and the insulation of the swivel.

This section analyzes the forces and torques of the cycles immediately before and at the time of the leakage. As there have been no failures in the BJA test campaign so far, only the RFHA test campaign is analyzed in this subsection. Prior to the occurrence of the leakage at the West RFHA, repeated smoke development and short shutdowns were observed. The actual leakage occurred at a temperature of 120 °C and a pressure of 21.7 bar, thus not under real operating conditions. Since no direct comparison cycles are available for these cycles, linear regression models are additionally used to compare the amplitudes.

Figure 5.15.: East facing side of west swivel joint and inside of insulation after leakage

Figure 5.16 shows the forces acting in the z-direction for the cycles in the leakage phase as a function of the rotation angle. Cycle 23,790 is one of the last cycles conducted under actual operating conditions. It exhibits similarities on both the east and west sides with the first 22,500 cycles, which are presented in section 5.1.2. On the east side, shown in the left half of the figure, only minor changes in amplitude and curve shape are observed. The maxima and minima of the forces remain mainly at the same angular positions. The observable changes are primarily due to variations in operating parameters, which are indicated in the figure legend. The most significant changes occur in cycle 24,150, particularly on the west side, depicted in the figure's right half. There, the amplitude of the forces in the z-direction increases, especially in the negative direction. This results in an amplitude of approximately 7000 N, corresponding to a force increase of over 60 %. In cycle 24,160, and during the leakage in cycle 24,240, the curve shape changes significantly again, leading to a shift in the positions of the maxima and minima. The maximum is now no longer at a rotation angle of 0 ° but at 120 °, and the minimum shifts from 130 ° to 75 °.

Since the previously identified general difference between the forces on the East and West sides complicates a direct comparison, the next step is to examine the torques. Figure 5.17 presents the torques around the y-axis for the same cycles as a function of the rotation position. An increase in amplitude is observed at cycle 24,150. This increase occurs on both sides, with the West side, shown in the right diagram, exhibit-

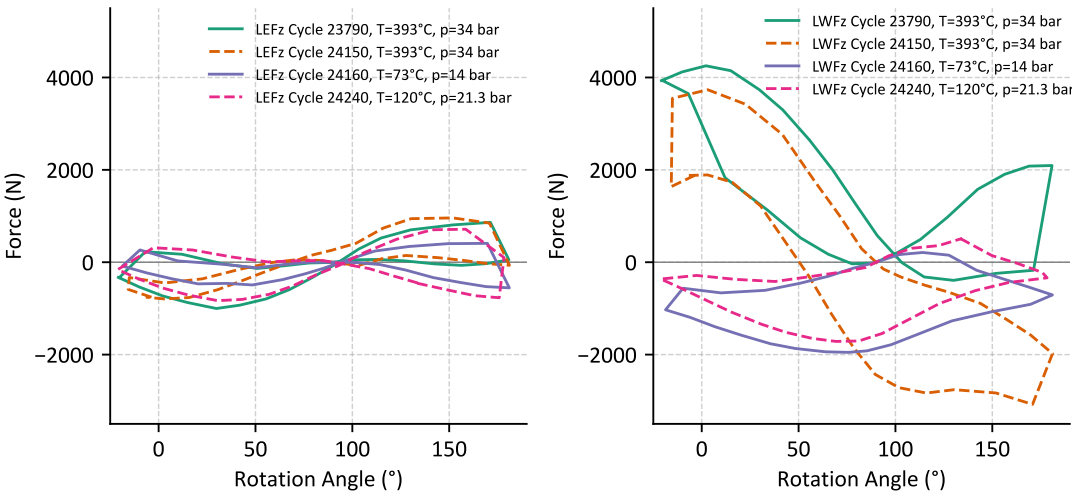

Figure 5.16.: Force values in z-direction during leakage of the RFHA

ing a greater increase. At cycles 23,790 and 24,160, both sides show similar values. However, at the time of leakage in cycle 24,240, a significant difference between the two sides is evident. With the renewed increase in temperature and pressure, higher torques are expected due to the positive correlation. This can be observed on the East side in the left diagram, whereas on the West side, the torques reach their lowest values at this time.

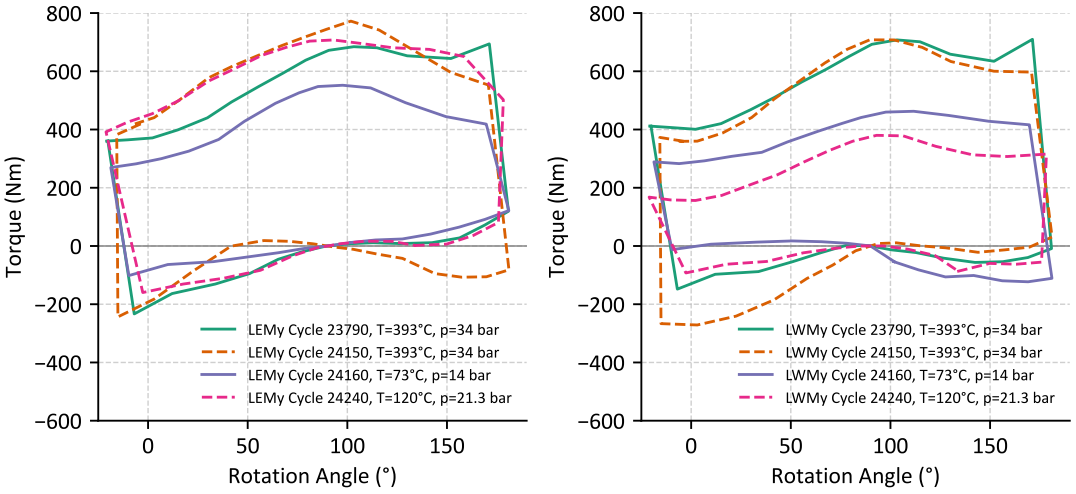

Figure 5.17.: Torque values at the y-axis during leakage of the RFHA

Significant changes in amplitude were observed during the leakage phase for both forces and torques. To analyze the development of the amplitudes in the last 250

cycles before the leakage in more detail, these are depicted in Figure 5.19 and Figure 5.20.

A Random Forest regression model and a linear regression (LR) model were trained to predict force and torque amplitudes. Since some of the cycles for the leakage phase took place at low temperatures and pressures, there are no direct comparative cycles, as already written. The LR models can, therefore, be used as a reference point for the expected force amplitudes. Due to the limited number of cycles with lower temperatures and pressures than the standard operating conditions and the strong linear dependencies of the variables identified in the correlation analysis, the linear regression model yields better results and is used in the following analysis. Figure 5.18 visually represents the models. Temperature and pressure can be specified as input variables as these are the main operating variables that are changed. The output is a predicted force or torque amplitude for a cycle under these operating conditions.

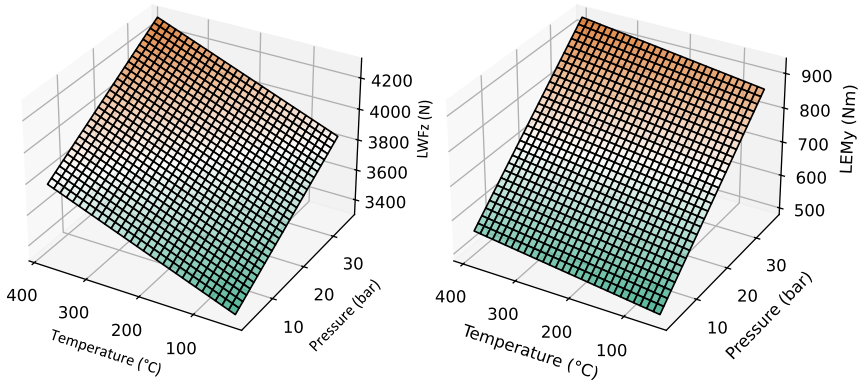

Figure 5.18.: Linear regression models with temperature and pressure as input and force or torque amplitudes as output

Figure 5.19 shows the force amplitudes in the z-direction for the last 250 cycles of the RFHA test campaign. The results of the LR model are shown as dotted lines, while solid lines represent the measured amplitudes. The left side of the figure shows the absolute amplitude values, while the right side shows the normalized amplitudes. Normalization is performed by dividing the absolute values by the average force amplitude identified in the force analysis, which is shown in Figure 5.4. Since it was determined that the west force values correspond to a 2 to 2.5-fold scaling of the east force values, a direct comparison is possible.

The force amplitude in the range of cycle 24,000 is around 5 to 10 % above the average

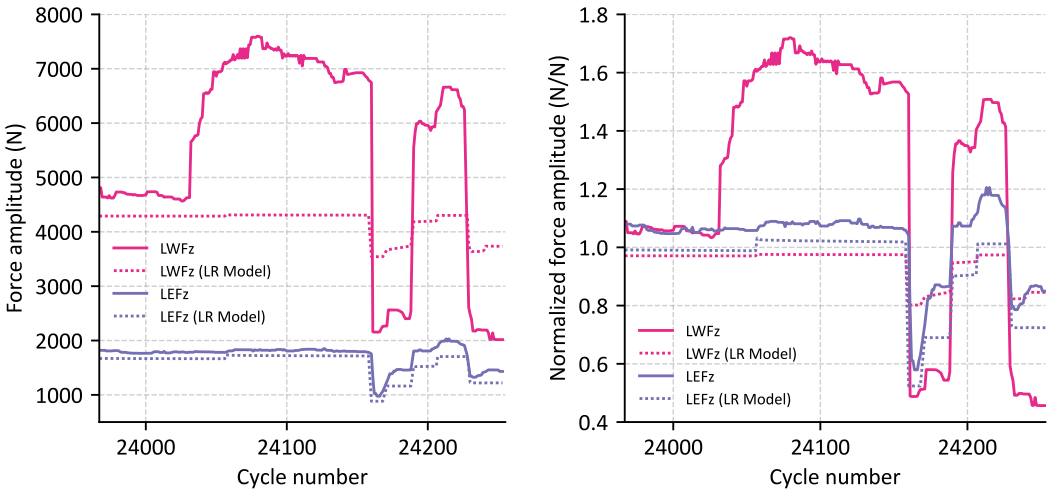

Figure 5.19.: Force amplitudes and normalized force amplitudes during leakage compared with linear regression models

of the test series. This increase begins at cycle 23,300, around 1000 cycles before the leakage, and reaches its maximum at cycle 24,000. The LR models deliver values that correspond approximately to the standard amplitude, which is to be expected as the standard operating conditions of 34 bar and 395 °C are present up to cycle 24,160. At cycle 24,030, a sudden increase in the force amplitude in the z-direction can be observed on the west side. The amplitude reaches over 7000 N at times, corresponding to an increase of more than 60 % compared to the average amplitude. The force amplitude on the east side remains constant mainly in this area up to cycle 24,160, with only a slight influence being recognizable.

A shutdown occurs at cycle 24,160 due to smoke development. Short-term smoke development had already occurred sporadically in the previous days. Since the start of the second half of the test after a three-month break at cycle 20,773, these phenomena have been observed several times, which indicates the occurrence of small leaks and can be interpreted as an indication of the aging of the swivel joints. After the shutdown, the force amplitude is greatly reduced, particularly on the west side, and is well below the values predicted by the LR model. In contrast, the reduction on the east side remains moderate and largely corresponds to the model predictions. Following the renewed heat-up, the force amplitude increases again, accompanied by further smoke development, whereupon the temperature and pressure are temporarily reduced. At cycle 24,240, a significant leakage occurs, which leads to the RFHA

being declared no longer operational and the test campaign having to be aborted. This is initially characterized by a sharp increase in force amplitudes, followed by an excessive decrease at reduced temperature and pressure. At the time of leakage, the east side shows a renewed increase in force amplitude from cycle 24,235, while the lowest values are recorded on the west side. This indicates that despite increasing operating parameters, the force amplitude on the west side remains low or decreases further. While the force amplitudes on the east side are largely within the range of the LR model, the values on the west side only reach around 50 % of the standard amplitude and thus remain well below the expected values. This could indicate that mechanical or structural changes occurred in the swivel joint during the phases with high forces observed about 150 to 200 cycles before the leakage.

One notable aspect is that the force amplitudes decrease more than expected at low operating parameters. In addition, the main leakage also occurs at reduced operating parameters. This could indicate that a structural change in the swivel has occurred such that high stresses due to high pressures and the thermal expansion of the material at elevated temperatures lead to high forces but do not cause significant leakage. At low operating parameters, on the other hand, the reduced stresses and loads lead to a lower force amplitude, whereby the seals fail, and, ultimately, leakage occurs. To support this hypothesis, the amplitudes of the torques are considered in the last step of the analysis.

Figure 5.20 shows the torque amplitudes in the leakage phase. The amplitudes predicted by the LR model are shown as dotted lines, while solid lines represent the measured values. Analogous to the force analysis, the absolute values are shown on the left-hand side and the normalized values on the right-hand side, whereby the normalization is carried out using the average torque amplitudes identified in subsection 5.1.3. When analyzing the torques in cycle 22,500, it was already determined that the torque amplitudes on the west side are increased. In the phase in which the forces increase by 60 %, the torque amplitudes on the west side increase by more than 20 % compared to the average values and the model predictions. On the east side, the values remain primarily constant and increase by a maximum of 10 % above the average. Analogous to the force amplitudes, the torque amplitudes on the west side also fall sharply at the time of leakage at cycle 24,240 and only reach around 50 % of the average values. This observation is consistent with the results of the force analysis, which showed a sharp drop after a phase with high amplitudes, which is below the

predictions of the LR model. This supports the hypothesis that structural changes in the swivel joint cause these changes in force and torque amplitudes, ultimately leading to significant leakage.

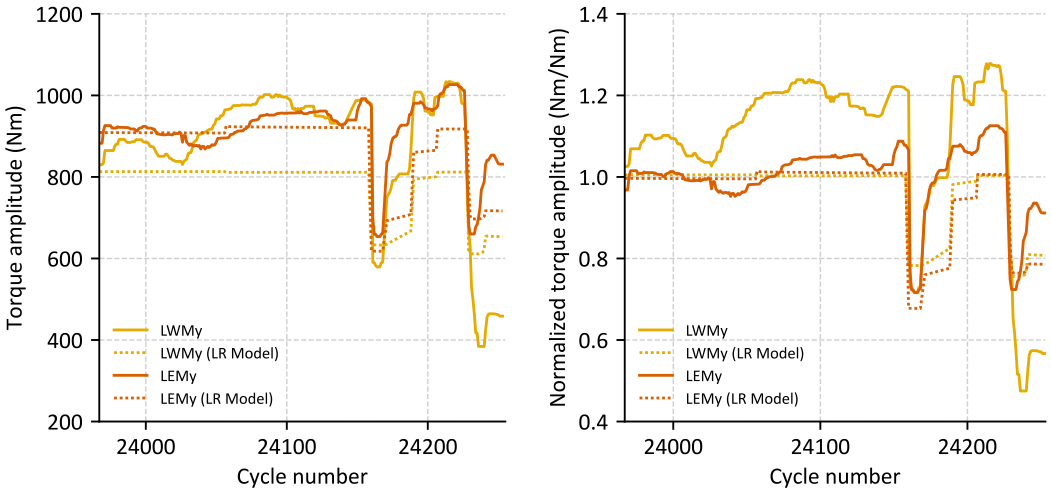

Figure 5.20.: Torque amplitudes and normalized torque amplitudes during leakage compared with linear regression models

The force and torque amplitudes analysis shows that significant changes occur several hundred cycles before the final leakage. An increase in amplitudes can be observed, especially on the west side, where the leakage occurs, followed by a sharp drop shortly before the leakage. On the other hand, the values on the east side remain largely stable or within the expected range. This phenomenon is particularly noticeable on the z-axis for the force amplitudes and the y-axis for the torque amplitudes, which is why these were analyzed in detail here. However, similar behavior can also be seen for the other axes. Figures on this can be seen in Appendix A.13 to A.16. The observation that a significant increase in amplitudes is first observed and then significant leakage occurs with reduced operating parameters indicates that structural changes in the swivel joint play a role. The finding that the force amplitudes already increase by up to 10 % around 1000 cycles before leakage and that an increase of more than 60 % can occur around 150 to 200 cycles before leakage is relevant for condition monitoring and predictive maintenance. As approximately one cycle per day is carried out in practice, these periods correspond to a lead time of almost three years and six months, respectively. This shows structural changes can be detected early, leaving sufficient time to initiate suitable maintenance measures.

5.2. Conclusion

The data analysis that was conducted shows that monitoring force and torque amplitudes can provide meaningful insights into the mechanical behavior and degradation of REPA components. For RFHAs, the forces remained largely stable throughout most of the lifetime, with a clear increase in amplitudes several hundred cycles before leakage. This indicates that structural changes begin well in advance and can be detected early, making predictive maintenance based on force data both feasible and effective.

In contrast, the BJA campaign revealed higher fluctuations even at an early stage, though no damage has occurred yet. While long-term conclusions cannot be drawn at this point, the similarities in load behavior suggest that early indicators of failure may also emerge in the future.

The torque analysis further supported these findings and helped compensate for uncertainties in the force measurements, highlighting the value of combining both metrics. Overall, the results confirm that load-based condition monitoring is a promising approach, particularly in the case of the RFHA, and provide a solid basis for extending these methods to other REPA types.

6. Summary & Outlook

As part of this study, an RFHA test series was conducted on the REPA test rig. A total of 24,240 cycles were completed until leakage occurred. Subsequently, the test rig was modified by integrating new load cells specifically calibrated to the expected force values to enhance measurement accuracy. Additionally, two BJAs were configured and installed according to the test rig's requirements. A detailed analysis of the BJA results could not be conducted. Only the first BJA test series with 2,700 cycles performed was analyzed. All necessary data processing, visualization, and force analysis tools are available to analyze the upcoming tests further.

The force analysis of the RFHA test campaign revealed that both force and torque amplitudes remained largely constant throughout the component's lifetime. Significant changes occurred several hundred cycles before the final leakage, particularly on the west side, where the leakage ultimately developed. In this area, amplitudes initially increased gradually, rising sharply shortly before leakage and dropping below expected values. In contrast, values on the east side remained largely stable. This behavior was particularly pronounced in force amplitudes along the z-axis and torque amplitudes along the y-axis. It was observed that amplitudes increased by up to 10 % approximately 1,000 cycles before leakage and by more than 60 % between 150 and 200 cycles before leakage. This trend could serve as a basis for condition monitoring. In practice, approximately one cycle is performed per day, providing a warning period of nearly three years or six months, enabling predictive maintenance.

Several limitations regarding the methodology of accelerated lifetime testing can be identified. While a complete cycle takes one day under real operating conditions, it is performed within only 2.5 minutes of the test. Consequently, numerous factors occurring under actual operating conditions are not captured. For example, in field operation, movement occurs incrementally in 0.25° steps throughout the day, whereas in the test, movement is continuous. Additionally, long-term corrosive effects and fluctuations in temperature and pressure, which occur in real operation, depending

on the time of day, are not adequately represented.

Analysis of the test results revealed a significant difference between the east and west sides of the tested components. The exact cause of this discrepancy could not be conclusively identified. Possible explanations include sensor calibration errors or variations in installation. This introduces a degree of uncertainty in the interpretation of results. Furthermore, only two RFHAs and two BJAs were tested, meaning the conditions leading to leakage could vary under different circumstances. Since the critical leakage did not occur under real operating conditions, further investigations are necessary to precisely determine the failure mechanisms and identify appropriate parameters for condition monitoring and predictive maintenance. In parallel, the manufacturer of the RFHA is analyzing the affected system to determine the cause of the leakage and understand the failure in detail.

The findings indicate that condition monitoring and predictive maintenance for REPAs based on force measurements are generally feasible. However, additional sensor-based approaches could also be considered. Before the occurrence of critical leakage, smaller leaks in RFHAs were observed, accompanied by smoke formation. In real-world applications, a sniffer measuring HTF concentration in the air, a visual monitoring system for detecting smoke formation, or a vibration analysis of the swivel could be viable alternatives. Since force measurement is complex and costly, reducing measurements to a single direction, such as only the z-axis, could help decrease sensor complexity and costs.

Although only a limited number of cycles could be analyzed in the BJA test campaign, the data already reveal characteristic force and torque patterns that resemble those observed in the RFHA tests. While long-term conclusions are not yet possible, these similarities suggest that early failure indicators may also develop in BJAs over time. Consequently, force-based condition monitoring could also be a viable approach for these components. In addition, complementary methods such as visual inspection, gas detection, or vibration analysis remain promising options. Visual monitoring is particularly relevant for detecting smoke formation and observing angular changes between individual ball joints.

In the present experiment, cameras were installed to monitor the angles between the pipe segments and individual ball joints. Upon completion of the test campaign, force

analyses can be conducted using the Python tools developed in this study and compared with image recordings and planned sniffer and vibration analyses. The focus will be on phases in which issues or leakages occur.

The results provide promising initial insights into condition monitoring based on force analysis. However, further investigations are required to develop a robust method in combination with other measurement techniques. The objective is to establish a condition monitoring and predictive maintenance concept that simplifies maintenance and enhances PTC power plant safety and operational reliability.

Bibliography

[1] United Nations: The Paris Agreement. https://www.un.org/en/climatechange/paris-agreement. Accessed: 2025-02-11.

[2] Asim Ahmad, Om Prakash, Rukaiya Kausher, Gaurav Kumar, Shatrudhan Pandey, and S.M. Mozammil Hasnain. Parabolic trough solar collectors: A sustainable and efficient energy source. *Materials Science for Energy Technologies*, 7:99–106, 2024.

[3] Objetivos de la PSA como gran instalación solar. https://www.psa.es/es/gen/objetivos.php. Accessed: 2025-02-11.

[4] Abdul Hai Alami, A.G. Olabi, Ayman Mdallal, Ahmed Rezk, Ali Radwan, Shek Mohammod Atiqure Rahman, Sheikh Khaleduzzaman Shah, and Mohammad Ali Abdelkareem. Concentrating solar power (CSP) technologies: Status and analysis. *International Journal of Thermofluids*, 18:100340, 2023.

[5] Robert Pitz-Paal. Solar Technology. University Lecture, Institute of Solar Research, RWTH Aachen University, 2023.

[6] Reinhold Kneer. Heat and Mass Transfer I. University Lecture, Institute of Heat and Mass Transfer, RWTH Aachen University, 2023.

[7] W. A. Beckman J. A. Duffie. *Solar Engineering of Thermal Processes*, chapter 1. John Wiley and Sons, Ltd, 2013.

[8] Volker Heinzel Robert Stieglitz. *Thermische Solarenergie*, volume 1. Springer Berlin, Heidelberg, 2013.

[9] Direct Normal Irradiation (DNI). https://solargis.com/resources/free-maps-and-gis-data. Accessed: 2024-12-03.

[10] Campo Heliostatos PSA. https://quo.eldiario.es/gigantes/q2302891190/visita-a-la-plataforma-solar-de-almeria. Accessed: 2024-12-11.

[11] Md Tasbirul Islam, Nazmul Huda, A.B. Abdullah, and R. Saidur. A comprehensive review of state-of-the-art concentrating solar power (CSP) technologies: Current status and research trends. *Renewable and Sustainable Energy Reviews*, 91:987–1018, 2018.

[12] Thomas Keck and Wolfgang Schiel. Dish Stirling Anlagen zur dezentralen Stromerzeugung. 53, 01 2001.

[13] Lee A. Weinstein, James Loomis, Bikram Bhatia, David M. Bierman, Evelyn N. Wang, and Gang Chen. Concentrating Solar Power. *Chemical Reviews*, 115(23):12797–12838, December 2015. Publisher: American Chemical Society.

[14] Robert Pitz-Paal. Parabolic Trough, Linear Fresnel, Power Tower - A Technology Comparison. Institute for Advanced Sustainability Studies e.V.

[15] A.Z. Hafez, A.M. Attia, H.S. Eltwab, A.O. ElKousy, A.A. Afifi, A.G. AbdElhamid, A.N. AbdElqader, S-E.K. Fateen, K.A. El-Metwally, A. Soliman, and I.M. Ismail. Design analysis of solar parabolic trough thermal collectors. *Renewable and Sustainable Energy Reviews*, 82:1215–1260, 2018.

[16] Solar Millennium. Die Parabolrinnen-Kraftwerke Andasol 1 bis 3. 2011.

[17] Andreas Plumpe. Design of a Test Rig and its Testing Methods for Rotation and Expansion Performing Assemblies in Parabolic Trough Collector Power Plants. Master's thesis, RWTH Aachen Institute of Solar Research, German Aerospace Center (DLR), 2016.

[18] K. Riffelmann, T. Richert, P. Nava, and A. Schweitzer. Ultimate Trough® – A Significant Step towards Cost-competitive CSP. *Energy Procedia*, 49:1831–1839, 2014. Proceedings of the SolarPACES 2013 International Conference.

[19] Hank Price, Eckhard Lüpfert, Delilah Kearney, Eduardo Zarza, Gilbert Cohen, R. Gee, and Rod Mahoney. Advances in Parabolic Trough Solar Power Technology. *Journal of Solar Energy Engineering-transactions of The Asme - J SOL ENERGY ENG*, 124, 2002.

[20] HelioTrough Product Facts. `http://www.heliotrough.com/english/heliotrough/heliotrough_facts.html`. Accessed: 2024-12-16.

[21] Heliotrough Skal-ET solar collector. `https://www.heliotrough.com/cms/images/SKAL-ET-b.jpg`. Accessed: 2024-12-16.

[22] Prashant Saini, Shweta Singh, Priyanka Kajal, Atul Dhar, Nikhil Khot, M.E. Mohamed, and Satvasheel Powar. A review of the techno-economic potential and environmental impact analysis through life cycle assessment of parabolic trough collector towards the contribution of sustainable energy. *Heliyon*, 9(7):e17626, 2023.

[23] Pablo Tagle, Krishna Nigam, and Carlos Rivera-Solorio. Parabolic trough solar collectors: A general overview of technology, industrial applications, energy market, modeling, and standards. *Green Processing and Synthesis*, 9:595–649, 11 2020.

[24] Yathin Krishna, M. Faizal, R. Saidur, K.C. Ng, and Navid Aslfattahi. State-of-the-art heat transfer fluids for parabolic trough collector. *International Journal of Heat and Mass Transfer*, 152:119541, 2020.

[25] C. Jung, J. Dersch, A. Nietsch, and M. Senholdt. Technological Perspectives of Silicone Heat Transfer Fluids for Concentrated Solar Power. *Energy Procedia*, 69:663–671, 2015. International Conference on Concentrating Solar Power and Chemical Energy Systems, SolarPACES 2014.

[26] D. Kearney, B. Kelly, U. Herrmann, R. Cable, J. Pacheco, R. Mahoney, H. Price, D. Blake, P. Nava, and N. Potrovitza. Engineering aspects of a molten salt heat transfer fluid in a trough solar field. *Energy*, 29(5):861–870, 2004. SolarPACES 2002.

[27] Gustavo A. de Andrade, Paulo H.F. Biazetto, and Julio E. Normey-Rico. A simplified dynamic model of direct stem generation solar plants for state estimation and control applications. *IFAC-PapersOnLine*, 58(14):61–66, 2024. 12th IFAC Symposium on Advanced Control of Chemical Processes ADCHEM 2024.

[28] Rafael Aguilar, Loreto Valenzuela, Antonio L. Avila-Marin, and Pedro L. Garcia-Ybarra. Simplified heat transfer model for parabolic trough solar collectors using supercritical CO2. *Energy Conversion and Management*, 196:807–820, 2019.

[29] Pablo D. Tagle-Salazar, Krishna D.P. Nigam, and Carlos I. Rivera-Solorio. Parabolic trough solar collectors: A general overview of technology, industrial applications, energy market, modeling, and standards. *Green Processing and Synthesis*, 9(1):595–649, 2020.

[30] M. Shahabuddin, M.A. Alim, Tanvir Alam, M. Mofijur, S.F. Ahmed, and Greg Perkins. A critical review on the development and challenges of concentrated solar power technologies. *Sustainable Energy Technologies and Assessments*, 47:101434, 2021.

[31] Ehsanul Kabir, Pawan Kumar, Sandeep Kumar, Adedeji A. Adelodun, and Ki-Hyun Kim. Solar energy: Potential and future prospects. *Renewable and Sustainable Energy Reviews*, 82:894–900, 2018.

[32] Christoph Hilgert, Christoph Happich, Timo Effertz, and Nicole Janotte. REPA Teststand. `https://www.dlr.de/de/sf/downloads/dokumente/soko/soko2015/poster/Hilgert_-_REPA_Test_Rig_-_DLR_2015.pdf`, 2015. Accessed: 2025-01-23.

[33] Solar S2 Series Flexible Ball Joints Installation, Operating and Maintenance Instructions. `https://www.advancedthermal.net/wp-content/uploads/2021/07/ATS-SOLAR-IOM-2010-Rev.-6.pdf`. Accessed: 2025-03-19.

[34] Ryan Shininger, Kyle Kattke, Mark Anderson, Francisco Ortiz Vives, Mirko Saur, Matthew Boyd, and Hank Price. Flexible hose interconnect testing for parabolic troughs with nitrate salt. *AIP Conference Proceedings*, 2303(1):150014, 12 2020.

[35] Dylan C. P. Grogan. Development of Molten-Salt Heat Transfer Fluid Technology for Parabolic Trough Solar Power Plants - Public Final Technical Report. Technical report, Abengoa Solar, LLC, 08 2013.

[36] Jun Dong, Jianfang Tang, Chuncheng Zang, Li Xu, and Zhifeng Wang. Development and Application of Test System for Ball Joints of Parabolic Trough Solar Collector. *Power Generation Technology*, 45(2):291–298, 2024.

[37] ME-Messsysteme GmbH. Skalierung des Ausgangssignals. `https://www.me-systeme.de/docs/support/anschluss-inbetriebnahme/kb-display.pdf`. Accessed: 2025-01-22.

[38] Stefan Keil. *Dehnungsmessstreifen*. Springer Vieweg Wiesbaden, 2 edition, 2 2017.

[39] Müller Thore. Commissioning and validation of the underlying model of a test rig analyzing rotation and expansion performing assemblies in parabolic trough collector power plants. Master's thesis, RWTH Aachen Institute of Solar Research, German Aerospace Center (DLR), 2017.

[40] Six Axis F/T Sensor User's Manual. `https://www.srisensor.com/uploads/13d2fa2c.pdf`. Accessed: 2025-01-27.

[41] Saliou Guillaume, Christoph Hilgert, Rafael López-Martín, and Eckhard Lüpfert. Segregation of influences on flexible pipe connectors (REPA) force under field operation condition for parabolic trough collector plants. *AIP Conference Proceedings*, 2815(1):080009, 10 2023.

[42] Hilbel Tobias. Design of the motion control for a test rig analyzing rotation and expansion performing assemblies in parabolic trough collector power plant applications, 2016.

[43] Kraftsensor K6D175 10kN/1kNm/UP13. `https://www.me-systeme.de/de/k6d175-10kn-1knm`. Accessed: 2025-03-10.

[44] Ana Cleia González Alves. Dynamometer and translational movement improvement for the REPA Test Rig in the Solar Platform of Almeria. Master's thesis, Universidad de Almería, Escuela Superior de Ingeniería, 2023.

[45] Six Axis Circular Load Cell D280MM F3KN. `https://www.srisensor.com/de/m43xx-series-6-axis-ft-load-cell-for-industrial-application-product/`. Accessed: 2025-01-23.

[46] Abhinav Nagpal and Goldie Gabrani. Python for Data Analytics, Scientific and Technical Applications. In *2019 Amity International Conference on Artificial Intelligence (AICAI)*, pages 140–145, 2019.

[47] McKinney Wes. *Python for data analysis*. O'Reilly Media, Inc., 1 edition, 2012.

[48] Loreto Valenzuela Rafael López-Martín and Carmen M. Amador-Cortés. Torque in the rotation axis of a parabolic trough solar collector due to wind loads. SolarPACES 2024 Conference, Rome, Italy, 2024.

A. Appendix

Table A.1.: Bill of material for ball joint assemblies east and west

Reg. No.	Description	Diameter	Length	Quantity	Info
1	Pipe - SA-106 SCH 40, Gr B	2"	845 mm	2	BJ Connection West
2	Pipe - SA-106 SCH 40, Gr B	2"	670 mm	2	BJ Connection East
3	Pipe - SA-106 SCH 40, Gr B	2"	564 mm	1	Top-Tube West
4	Pipe - SA-106 SCH 40, Gr B	2"	477 mm	2	Fixture/Termopozo Tube East+West
5	Pipe - SA-106 SCH 40, Gr B	2"	214 mm	2	Bottom Connection Tube 2
6	Pipe - SA-106 SCH 40, Gr B	2"	176 mm	1	Top-Tube East
7	Pipe - SA-106 SCH 40, Gr B	2.5"	347 mm	2	Bottom Connection Tube 1
8	Pipe - SA-106 SCH 40, Gr B	2.5"	336 mm	1	Top Connection 45 ° East
9	LR Elbow 90 ° ASME B16.9, ASTM A-234	2"	R76 mm	10	
10	LR Elbow 45 ° ASME B16.9, ASTM A-234	2.5"	B44 mm	2	
11	LR Elbow 90 ° ASME B16.9, ASTM A-234	2.5"	R95 mm	4	
12	Concentric Reducer 2"-2.5" ASME B16.9, ASTM A-234	2" - 2.5"	89 mm	4	
13	Termopozo	-	-	2	
14	Ball Joint 2"-S2-SWW-400H-70-20	2"	168.3 mm	6	
15	Flex Hose	2.5"	1050 mm	2	
16	Pipe Fixture	-	-	2	

Sunrise Instruments Calibration Report

Address:2nd Floor Building B2 19#Keyuan Xishi Road Nanning Guangxi Province China 530007
Phone:+86 771-389-9499 Fax:+86 771-389-9497
Email:sri@srisensor.com

Calibration No.	SRi-OR-67946	Cal Date	2023-7-17
Model No.	M4347K5	Serial No.	21177
Technician	Wei Jing Xian	Temp(C)/Hum.(%).	22.0 / 65.0
Customer		Excitation(V)	5.0080
Description	F3KN D280MM LC	Cable Length	
Comments	SHCS M10:45N.m		

Voltage Calibration

Bridge	Capacity	Zero Offset	Nonlinearity	Hysteresis	Output @ Capacity	Sensitivity
	N/Nm	V	%FS	%FS	V	V/EU
FX	3000	-0.0534	0.15	0.33	5.1268	1.7089E-03
FY	-3000	-0.3734	-0.11	-0.30	-5.1869	1.7290E-03
FZ	-6000	0.1452	-0.09	-0.19	-5.1025	8.5042E-04
MX	1500	-0.0101	0.04	0.13	5.2498	3.4998E-03
MY	1500	-0.0245	0.05	0.15	5.1445	3.4297E-03
MZ	1000	-0.2565	0.62	0.36	5.1137	5.1137E-03

CROSSTALK

Bridge	Load	FX	FY	FZ	MX	MY	MZ
	N/Nm	% FS	% FS	% FS	% FS	% FS	% FS
FX	3000	0.00	0.47	-0.42	0.04	0.22	-0.04
FY	-3000	0.53	0.00	-0.06	-0.03	-0.05	-0.30
FZ	-6000	-1.81	-1.54	0.00	0.11	0.49	-0.44
MX	1500	-1.49	-1.05	0.70	0.00	0.30	-1.49
MY	1500	-0.46	2.29	0.98	-0.21	0.00	-1.13
MZ	1000	0.84	-0.33	-0.39	-0.38	0.54	0.00

Reference Load Cell

Manufacturer	Model Type	Model No.	Serial No.	Cal Due Date
SUNRISE	Golden Standard	M3006-22K	SRILSB-549	2023/11/29

Figure A.1.: Calibration protocol M4347K5 load cell east

Sunrise Instruments Calibration Report

Address:2nd Floor Building B2 19#Keyuan Xishi Road Nanning Guangxi Province China 530007
Phone:+86 771-389-9499 Fax:+86 771-389-9497
Email:sri@srisensor.com

Calibration No.	SRi-OR-68083	Cal Date	2023-7-28
Model No.	M4347K5	Serial No.	21260
Technician	Wei Jing Xian	Temp(C)/Hum.(%).	22.0 / 65.0
Customer		Excitation(V)	5.0070
Description	F3KN D280MM LC	Cable Length	
Comments	SHCS M10:45N.m		

Voltage Calibration

Bridge	Capacity	Zero Offset	Nonlinearity	Hysteresis	Output @ Capacity	Sensitivity
	N/Nm	V	%FS	%FS	V	V/EU
FX	3000	0.1040	0.17	0.40	5.0011	1.6670E-03
FY	-3000	-0.2087	-0.11	-0.31	-5.0395	1.6798E-03
FZ	-6000	-0.2089	-0.09	-0.32	-4.9891	8.3151E-04
MX	1500	0.0450	0.06	0.16	5.1526	3.4350E-03
MY	1500	0.0040	0.03	0.16	5.0759	3.3839E-03
MZ	1000	0.0281	0.13	0.21	5.0873	5.0873E-03

CROSSTALK

Bridge	Load	FX	FY	FZ	MX	MY	MZ
	N/Nm	% FS	% FS	% FS	% FS	% FS	% FS
FX	3000	0.00	0.39	-0.08	0.02	0.20	0.19
FY	-3000	0.01	0.00	-0.01	-0.06	-0.03	-0.05
FZ	-6000	-2.78	-0.65	0.00	0.36	-0.08	-0.44
MX	1500	-1.20	-0.52	0.94	0.00	-0.17	-0.76
MY	1500	-0.56	1.11	0.92	0.61	0.00	-0.81
MZ	1000	0.23	0.23	0.21	0.22	0.07	0.00

Reference Load Cell

Manufacturer	Model Type	Model No.	Serial No.	Cal Due Date
SUNRISE	Golden Standard	M3006-22K	SRILSB-549	2023/11/29

Figure A.2.: Calibration protocol M4347K5 load cell west

Table A.2.: K6D175 load cell measurement uncertainty [41]

Uncertainty	**Approach**	**Value east**	**Value west**	**Estimated impact**
Zero signal when mounted, SF_0	measured	1 N	41 N	moderate
Relative hysteresis error, μ	meas. under stationary conditions			neglected
Relative creep 30 min, d_{cr}	<0.1 % FS	<10 N		minor
Relative linearity error, d_{lin}	<0.1 % FS	<10 N		minor
Relative repeatability error, b_{rg}	<0.1 % FS	<10 N		minor
Temperature effect on zero signal at 20 °C, $TK_{0,20\,°C}$	0.1 % FS / K	(+/-) 0 to 580 N		major
Temperature effect on characteristic value, TK_C	0.05 % RD / K	(+/-) 0 to 41 N		moderate
Difference in zero signal due to temperature hysteresis, U_{0,V^0}	meas. under stationary conditions			neglected
Difference in zero signal after complete heating cycle, $\Delta U_{0,nc}$	measured	9 N	18 N	minor

FS: of full scale, being in Z axis 20 kN, RD: of reading

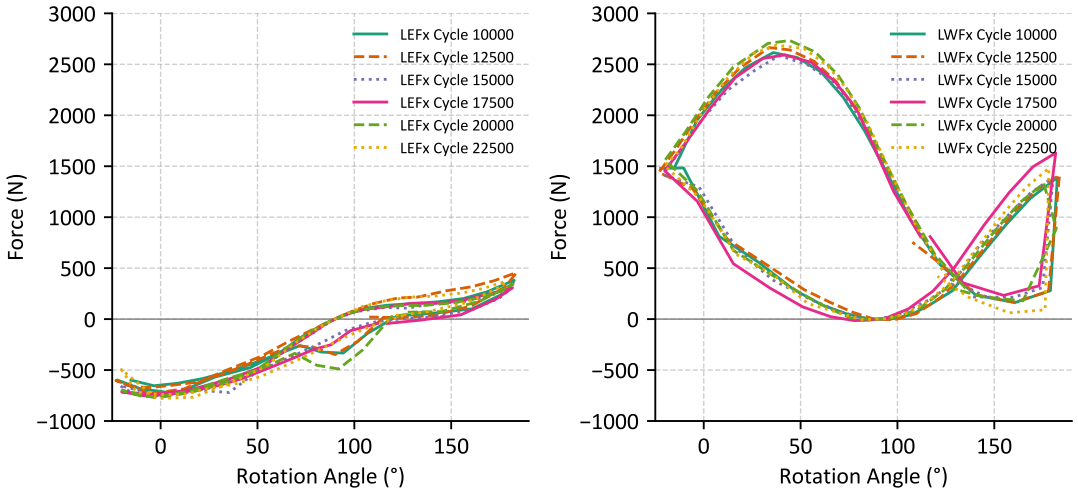

Figure A.3.: Force values in x-direction as a function of the rotation angle for the RFHA test campaign

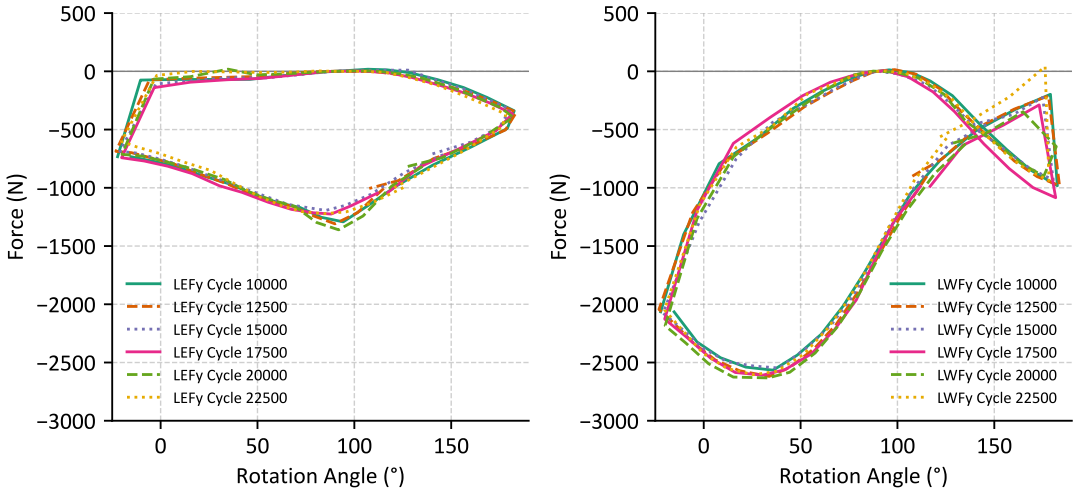

Figure A.4.: Force values in y-direction as a function of the rotation angle for the RFHA test campaign

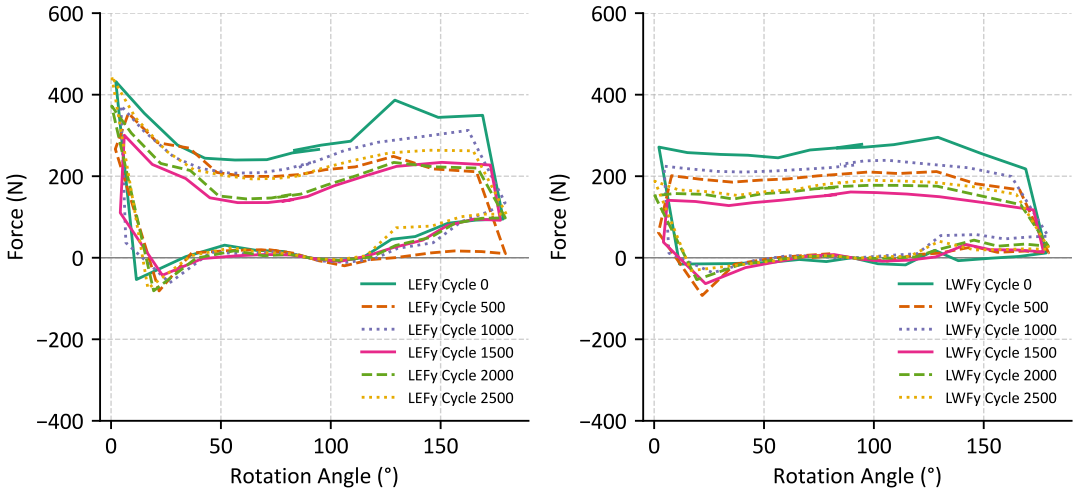

Figure A.5.: Force values in y-direction as a function of the rotation angle for the BJA test campaign

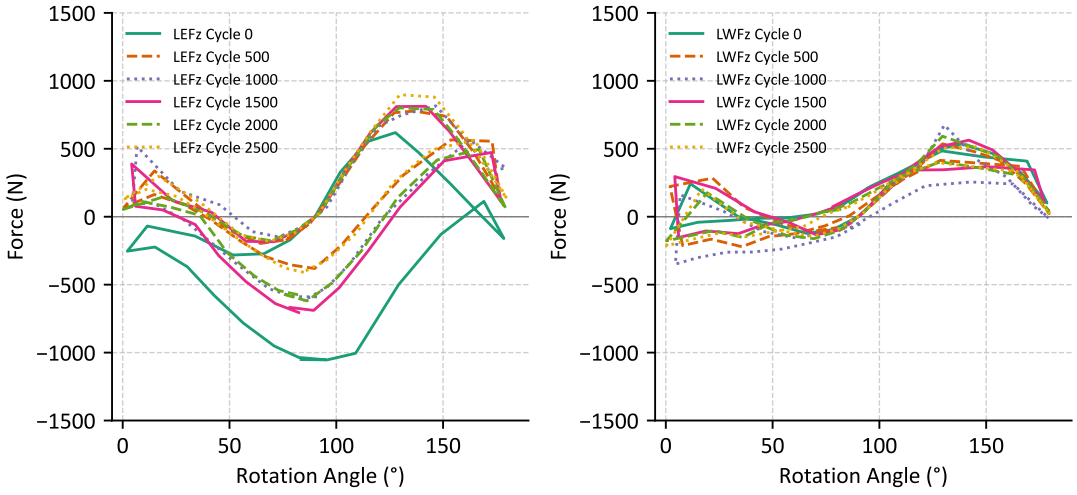

Figure A.6.: Force values in z-direction as a function of the rotation angle for the BJA test campaign

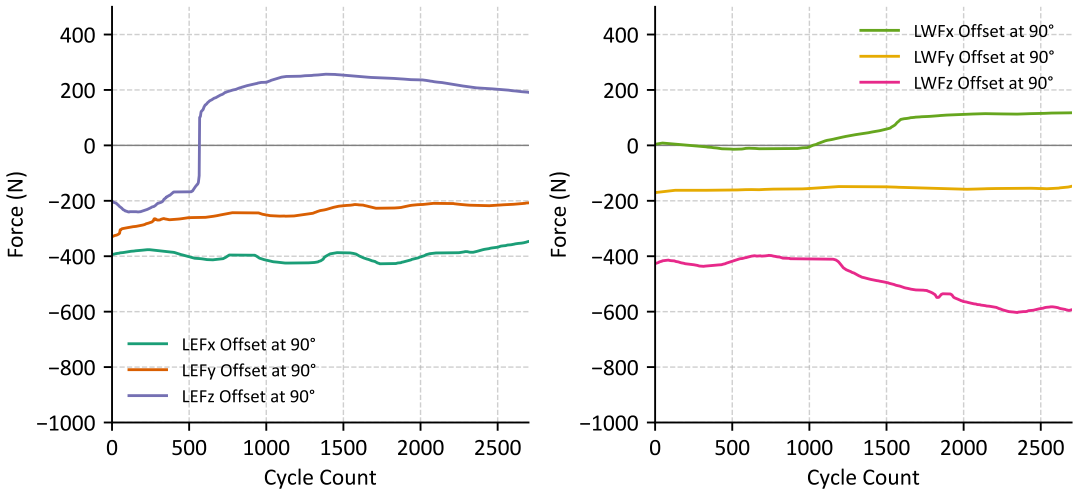

Figure A.7.: Force offset values for the cycles performed in the BJA test campaign

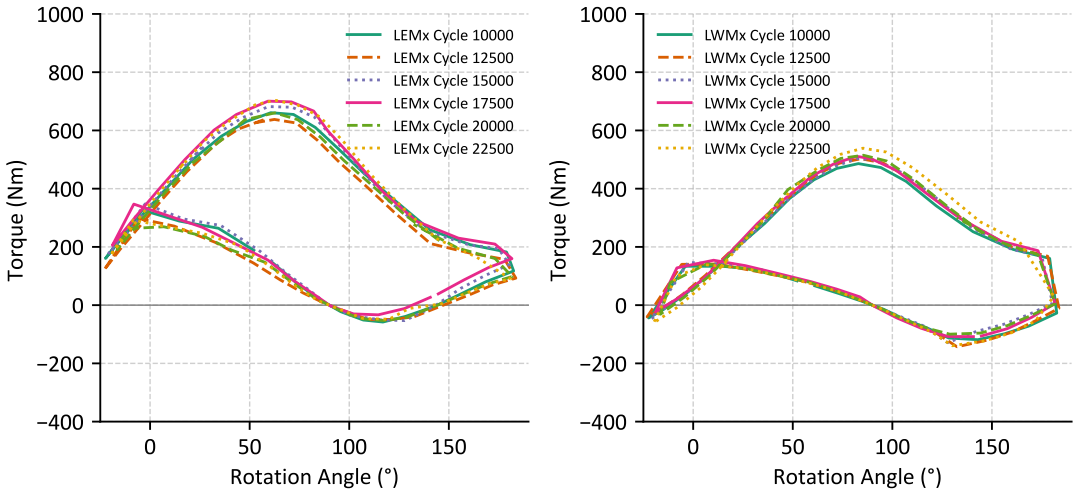

Figure A.8.: Torque values at the x-axis as a function of the rotation angle for the RFHA test campaign

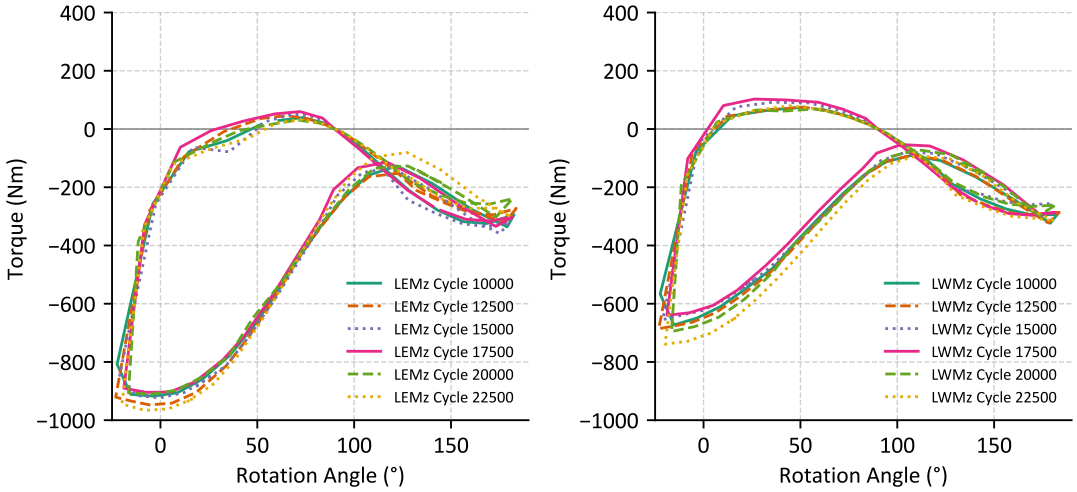

Figure A.9.: Torque values at the z-axis as a function of the rotation angle for the RFHA test campaign

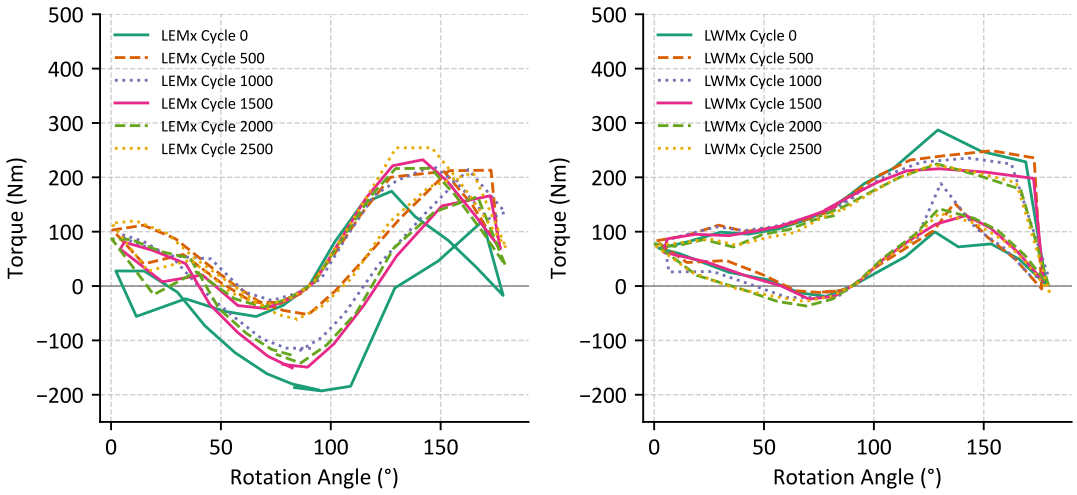

Figure A.10.: Torque values at the x-axis as a function of the rotation angle for the BJA test campaign

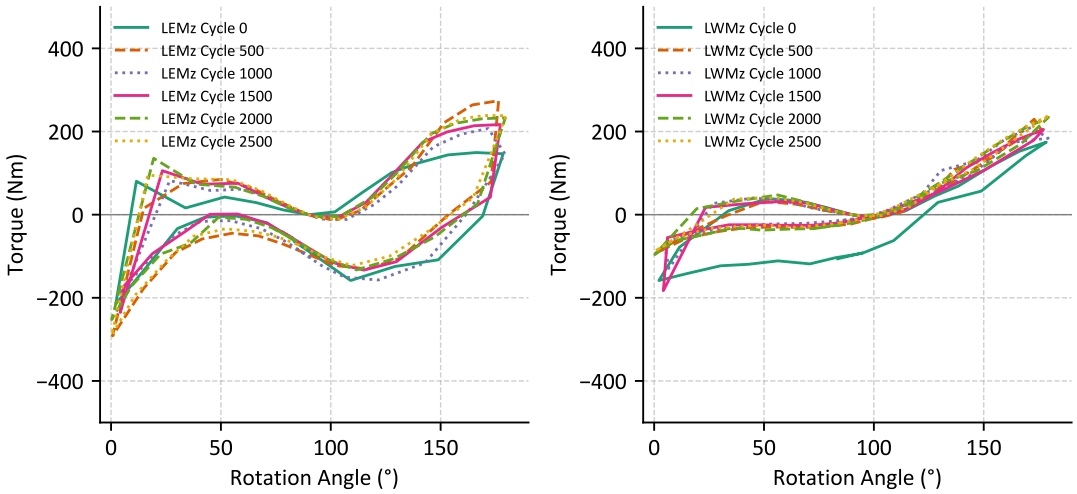

Figure A.11.: Torque values at the z-axis as a function of the rotation angle for the BJA test campaign

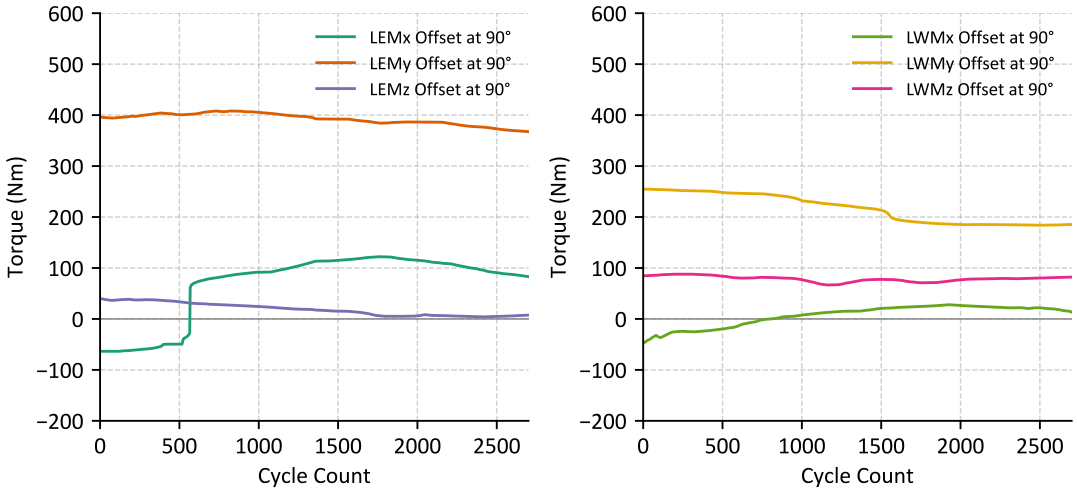

Figure A.12.: Torque offset values for the cycles performed in the BJA test campaign

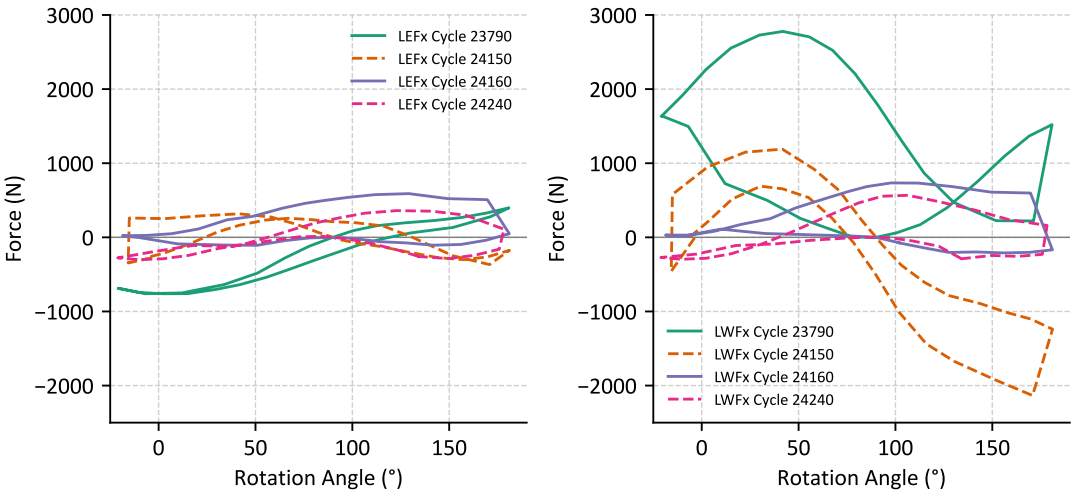

Figure A.13.: Force values in x-direction during leakage of the RFHA

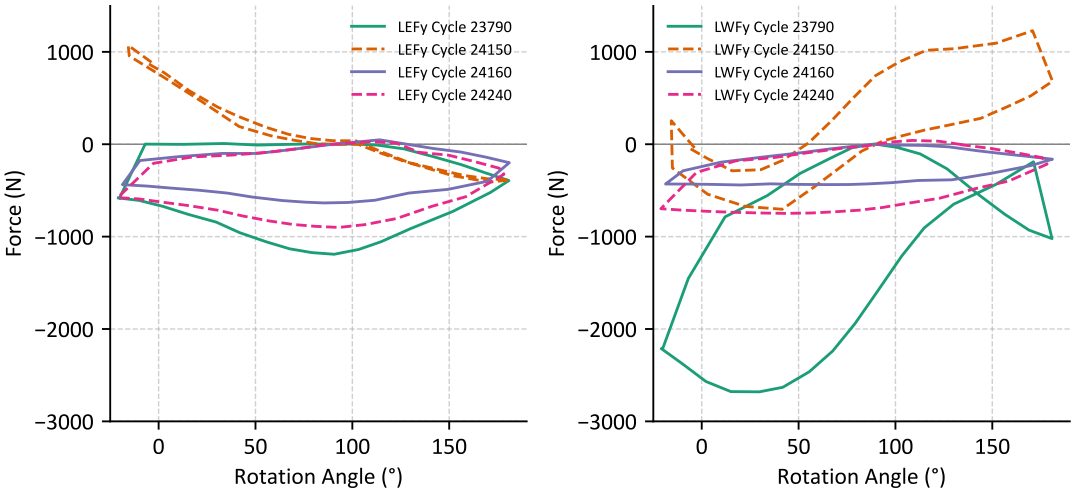

Figure A.14.: Force values in y-direction during leakage of the RFHA

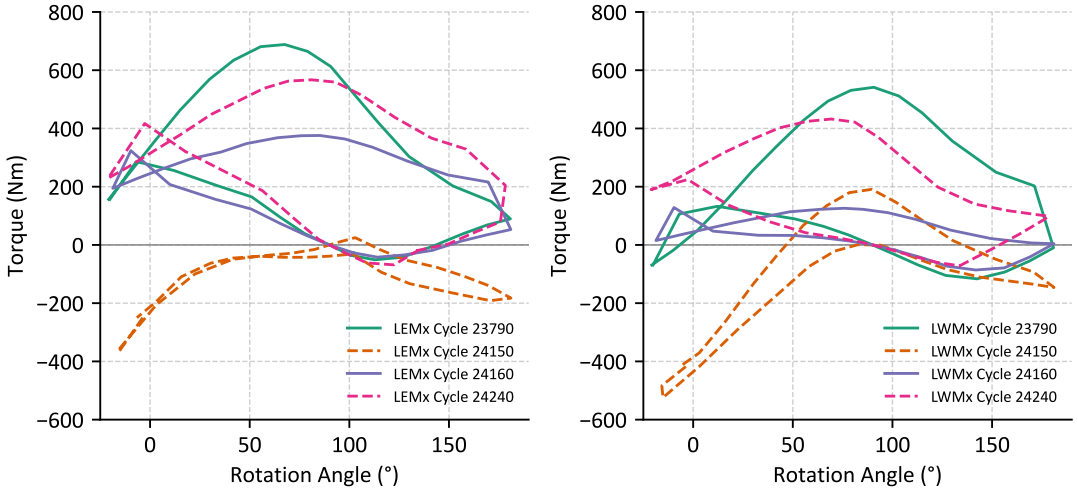

Figure A.15.: Torque values at the x-axis during leakage of the RFHA

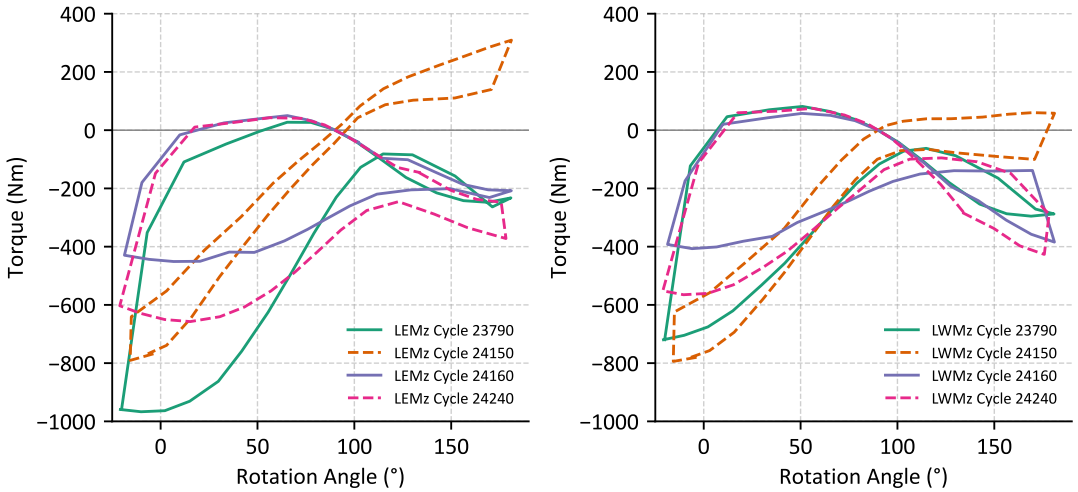

Figure A.16.: Torque values at the z-axis during leakage of the RFHA